BLACK HOLES IN THE EARLY UNIVERSE, IN COMPACT BINARIES, AND AS ENERGY SOURCES INSIDE SOLAR-TYPE STARS

Thesis by
Dragoljub Marković

In Partial Fulfillment of the Requirements
for the Degree of
Doctor of Philosophy

California Institute of Technology
Pasadena, California
1994
(Defended February 28, 1994)

To my beloved wife

Acknowledgments

I wish to thank my advisor Kip Thorne for encouragement and selfless support. His insight and his unsurpassed art of gentle prodding directed me past obstacles which would have seemed insurmountable without his help.

On numerous occasions I was enlightened by discussions with my bright and knowledgeable colleagues and collaborators, among whom I would like to mention Garrett Biehle, Lars Bildsten, Curt Cutler, Eanna Flanagan, Gunnar Klinkhammer, Amos Ori, Eric Poisson, Bharat Ratra and Gerald Sussman.

I also thank Shirley Hampton-Parker and Kate Finigan for their good will and patience with an inexhaustible source of administrative trouble.

My years at Caltech brought the invaluable benefit of friendship with Dimitris Kallifatides and Aaron Melman.

I am also deeply grateful to my parents Ljiljana and Miroslav for their love and support under increasingly difficult circumstances. Finally I am greatly indebted to my wife Romana, to whom this thesis is dedicated, for her sacrifice and encouragement.

Abstract

This thesis consists of three separate studies of roles that black holes might play in our universe.

In the first part we formulate a statistical method for inferring the cosmological parameters of our universe from LIGO/VIRGO measurements of the gravitational waves produced by coalescing black-hole/neutron-star binaries. This method is based on the cosmological distance-redshift relation, with "luminosity distances" determined directly, and redshifts indirectly, from the gravitational waveforms. Using the current estimates of binary coalescence rates and projected "advanced" LIGO noise spectra, we conclude that by our method the Hubble constant should be measurable to within an error of a few percent. The errors for the mean density of the universe and the cosmological constant will depend strongly on the size of the universe, varying from about 10% for a "small" universe up to and beyond 100% for a "large" universe. We further study the effects of random gravitational lensing and find that it may strongly impair the determination of the cosmological constant.

In the second part of this thesis we disprove a conjecture that black holes cannot form in an early, inflationary era of our universe, because of a quantum-field-theory-induced instability of the black-hole horizon. This instability was supposed to arise from the difference in temperatures of any black-hole horizon and the inflationary cosmological horizon; it was thought that this temperature difference would make every quantum state that is regular at the cosmological horizon be singular at the black-hole horizon. We disprove this conjecture by explicitly constructing a quantum vacuum state that is everywhere regular for a massless scalar field. We further show that this quantum state has all the nice thermal properties that one has come to expect of "good" vacuum states, both at the black-hole horizon and at the cosmological horizon.

In the third part of the thesis we study the evolution and implications of a hypothetical primordial black hole that might have found its way into the center of the Sun or any other solar-type star. As a foundation for our analysis, we generalize the mixing-length theory of convection to an optically thick, spherically symmetric accretion flow (and find in passing that the radial stretching of the inflowing fluid elements leads to a modification of the standard Schwarzschild criterion for convection). When the accretion is that of solar matter onto the primordial hole, the rotation of the Sun causes centrifugal hangup of the inflow near the hole, resulting in an "accretion torus" which produces an enhanced outflow of heat. We find,

however, that the turbulent viscosity, which accompanies the convective transport of this heat, extracts angular momentum from the inflowing gas, thereby buffering the torus into a lower luminosity than one might have expected. As a result, the solar surface will not be influenced noticeably by the torus's luminosity until at most three days before the Sun is finally devoured by the black hole. As a simple consequence, accretion onto a black hole inside the Sun cannot be an answer to the solar neutrino puzzle.

Contents

Chapter 1

Introduction

1 Motivation

Despite the long and venerable history of theoretical research on black holes, the observational evidence for the existence of those objects is not quite as compelling as that for some other exotic objects, such as white dwarves and neutron stars. The reason is not difficult to grasp: Black holes can be observed only through their interaction with astronomical bodies visible in some portion of the electromagnetic spectrum. This interaction is typically quite complex and the line of reasoning, leading from an astronomical observation to an inference of a black-hole existence, often contorted.

Fortunately, the broadening of the notion of astronomical "visibility," due to the advent of LIGO (Laser Interferometer Gravitational-wave Observatory) and similar detectors early in the next century, is likely to provide an entirely new and more direct view of black holes. In particular, the gravitational waves, emitted by coalescing binaries consisting of at least one black hole, should provide a wealth of information regarding not only the binaries' orbital parameters but also some properties of the black holes themselves, such as their masses and spins. Furthermore, those binaries are among the primary candidates for sources of detectable gravitational radiation due to the large amplitudes of the waves emitted and the frequency range that overlaps with the range of maximum sensitivity for the LIGO-type detectors ($10 - 1000\mathrm{Hz}$). Motivated by the prospect of detection of coalescence gravitational waves and the progress of the LIGO project, a group of researchers at Caltech and elsewhere is devoting a significant part of their energies to the study of emission of gravitational waves and some theoretical aspects of their detection.

Among the parameters that can be obtained directly from a detected coalescence wave is the distance of the binary from the Earth. In addition, as we explain below, the redshift can be estimated for binaries which consist of a black hole and a neutron star or of two neutron stars. Following some early suggestions by Schutz and Krolak [6], the author explores in detail, in Chapter 2 of this thesis, the prospects for the use of such distance and redshift estimates to determine the parameters describing the basic geometry of the Universe: the Hubble constant, the mean density and the cosmological constant. Despite great efforts of many astronomers, these parameters have eluded observational determination for decades [2, 3], and new approaches, such as the one discussed in this thesis, are worth considering.

The black-hole members of compact binaries are end-products of evolution of very massive stars. An entirely different mechanism of black-hole formation has been speculated, however. In the early universe large fluctuations of density, or violent events such as collisions of domain walls, might have lead to creation of the so-called "primordial black holes." The hypothetical formation of black holes in the very early, inflationary phase of the expansion of the universe leads to a question of principle: Both the black hole and the cosmological horizon of a mathematical idealization of the inflationary universe (the de Sitter universe) emit Hawking radiation. The radiation fluxes coming from the two sources have different temperatures. This lead W. Hiscock to speculate, several years ago, that the co-existence of the two horizons would, in any state of quantum fields, inevitably give rise to instabilities due to a divergent renormalized stress-energy tensor at least at one of the horizons. In particular, this would mean that if a state were chosen to yield a regular behavior at the cosmological horizon, the infinite stress-energy tensor at the black-hole horizon might preclude the formation of a black hole. In collaboration with W.G. Unruh, the author has investigated this conjecture and shown it to be wrong by exhibiting a quantum vacuum state that, despite the different temperatures of the horizons, has a stress-energy tensor regular everywhere. Thus, black holes can survive perfectly well in the early, inflationary universe. This work is presented in Chapter 3.

If actually formed in the early universe, a primordial black hole could survive for tens of billions of years, despite the mass loss due to the Hawking radiation, providing its initial mass was greater than about 10^{15} grams. It is, then, not totally implausible that such a black hole of a relatively small mass M ($M \ll M_{\odot}$) could, at later times, find its way into the center of a star and subsequently evolve through accretion. One would wish to know whether the accretion onto the black hole could produce a significant part of the luminosity of the star and thus announce the presence of the black hole to an outside observer. And if it could, for how long would the hole help the unfortunate star shine more brightly before devouring it? This, with attention focused on the Sun rather than a generic star, is the topic of Chapter 5.

Accretion onto a black hole was proposed by Hawking [3] as an explanation for the observed deficit of detected solar neutrinos. However, from a later study by Flammang [5], one can infer that luminosity produced by the accretion would be much smaller than the luminosity of the Sun — until at most a few hours before the demise of the Sun. Still, one might conjecture that one ingredient missing from

Flammang's treatment, the rotation of the Sun, could supply the accreting fluid with enough angular momentum to alter radically the geometry of the innermost region of the flow and, thus, give rise to luminosities far exceeding Flammang's value. These higher luminosities, if achieved, would lead to convection, which, in turn, would limit the amount of angular momentum that can be retained by the inflowing fluid. Thus, a non-spherical accretion inside the Sun would be, to use engineers' language, a complex "heat generator with a negative feedback." In Chapter 5 we seek to estimate the maximum output of such an engine and to describe, in broad strokes, the evolution of a hypothetical black hole inside a solar-type star. As a foundation for this analysis, the importance of convection has necessitated our generalizing the mixing-length theory of convection to a (roughly) spherically symmetric accretion flow, where convective velocities may be comparable or even smaller than the accretion velocity. This theory is presented in Chapter 4.

2 Overview

In Chapter 2 of this thesis we present a detailed analysis of the prospects for determining the fundamental cosmological parameters of our universe using the distance-redshift relation as revealed by binary coalescence gravitational waves. By measuring the signal amplitudes in at least three widely separated LIGO-type detectors, we can obtain the position of a binary source on the sky and, more importantly, "luminosity distance" D from the Earth.

The determination of the redshifts relies on the presence of neutron stars as standard-mass objects. Specifically, the quantity directly measurable from the phase (frequency) evolution of the signal is the "redshifted" neutron star mass $(1+Z)M_{\mathrm{n}}$ rather than the true mass M_{n}. However, astronomical observations of X-ray and binary pulsars, as well as theoretical studies of the formation of neutron stars, strongly indicate that neutron-star masses fall within a narrow range centered on $1.4M_{\odot}$. Thus, through a measurement of the redshifted neutron-star mass, we can infer the redshift Z itself.

In addition to discussing the basics of inferring distance D and redshift Z from binary coalescence waveforms, we develop in Chapter 2 a statistical method for deducing the three cosmological parameters by comparing observed and a-priori distributions of detected events in the Z-D plane.

Based on the properties of LIGO-type detectors that are expected to be operating early in the next century, we have been able to estimate the errors of such a determination of the cosmological parameters. These errors are quoted in the Abstract of Chapter 2.

In addition, in Chapter 2 we examine the influence of gravitational lensing on the inferred values of the cosmological parameters. Due to our ignorance of the statistics of lensing, a bias will be introduced in estimation of the parameters, because the lensing will shift the detected luminosity distances from the values that would be obtained in an ideally smooth Friedmann universe. In the case of the Hubble constant and the mean density of the universe, we estimate that this bias is less than or comparable to the statistical errors, assuming we observe with three "advanced" LIGO-type detectors during one year. On the other hand, the bias for the cosmological constant may be significantly larger than the corresponding statistical error. In our evaluations we have adopted the rough binary coalescence rates estimated by Phinney and, independently, by Narayan, Piran and Shemi [6], and the so-called "advanced-detector" benchmark noise curves for the detectors, as presented by the LIGO science team [7].

Chapter 3, which was coauthored with W.G. Unruh, is devoted to a study of quantum fields in a spacetime that is obtained if a Schwarzschild black hole is inserted inside a de Sitter universe. There are two variants of this spacetime: One contains an eternal black hole, including its past horizon, while the other contains a massive body that at some moment undergoes a gravitational collapse to form a black hole. These spacetimes possess two horizons: the black-hole horizon and the cosmological horizon resulting from an exponential expansion of the de Sitter universe. We specialize, for mathematical simplicity, to a two-dimensional version of the Schwarzschild-de Sitter and gravitational-collapse-de Sitter spacetimes.

In his study of a quantum scalar field in the two-dimensional collapse-de Sitter spacetime, W.A. Hiscock [8] examined several possible vacuum states and showed that each of them yielded a stress-energy tensor $T_{\mu\nu}$ divergent at one of the horizons. On the basis of these results, Hiscock conjectured that there was no quantum state that would have a $T_{\mu\nu}$ regular everywhere in this spacetime.

This hypothesis prompted W.G. Unruh and the author of this Thesis to identify a new family of states having, as we show in Chapter 3, a perfectly regular $T_{\mu\nu}$ on both the cosmological and black hole horizons.

In particular, W.G. Unruh devised a general method of constructing regular vacuum states in spacetimes with static horizons (of which the Schwarzschild-de Sitter spacetime is one example): A regular state was defined by modes of positive frequency with respect to affine parameters of any pair of null geodesics which intersected each other at a point between the two horizons.

In the case of the gravitational-collapse-de Sitter spacetime, it was possible, as demonstrated by the author of this thesis, to single out a particularly simple regular vacuum state (closely related to the Unruh states) defined with respect to the affine parameter of the past cosmological horizon only. The author showed that in this state a static particle detector would measure the modes propagating from the cosmological horizon to be precisely thermally populated at the temperature of the cosmological horizon. On the other hand, the modes propagating from the point where the black hole forms, toward the cosmological horizon, would be populated thermally at the temperature of the cosmological horizon before the collapse, and at the temperature of the black hole horizon late after the collapse. Furthermore, in complete agreement with the detector's measurements, the author showed that, near each of the horizons, $T_{\mu\nu}$ was a superposition of perfectly thermal radiation at the black hole temperature and at the cosmological temperature, with positive energy associated with the temperature of the distant horizon and negative energy with that of the nearby one. This form of $T_{\mu\nu}$ was amenable to a straightforward interpretation in terms of the membrane paradigm [9, 10]: It was a stress-energy tensor corresponding to the measurements made by static detectors from which one subtracted that of a thermal bath at the temperature of the nearby horizon.

In Chapter 4 we turn our attention to the generic problem of optically thick, spherically symmetric accretion. In particular, this Chapter is devoted to an analysis of convection on the background of the radial inflow. The main purpose is to develop a "mixing-length" model of the convection which would be sufficiently general to cover all possible ratios of convective and accretion velocities, with an essential requirement that all the velocities involved be subsonic.

An important ingredient of our model is the heating that every fluid element undergoes due to the inward increase of the luminosity. For instance, this heating allows the convective elements moving upward with respect to the mean flow of the fluid but downward relative to the black hole to accumulate more heat than the fluid flowing with the mean velocity of accretion, and thus sustain their convective motion. On the other hand, the radial stretching of the accreting fluid will tend to inhibit convection: In order to accelerate through the stretching medium, a convective element will need to have a larger temperature difference with the environment than in the case of convection in a static fluid. This will lead to a more rapid equalization of the element's temperature with that of the environment. To avoid this, the entropy gradient, $\partial S/\partial r$, will have to be more negative than a certain typically small, negative value (proportional to the amount of radial stretching) — the threshold of convection. This shifting of the threshold constitutes a modification of the familiar Schwarzschild criterion ($\partial S/\partial r < 0$) for convection in a static fluid.

In an application of our model of convection to the structure of an optically thick, spherically symmetric accretion flow at subsonic velocities, we conclude that, at least in the case of a gas-pressure-dominated fluid with a homogeneous chemical composition, *every* such flow must be convective. However, in low-luminosity situations, such as those discussed by Flammang [5], only a small portion of the total luminosity is transported by convection and the luminosity is virtually independent of radius. Furthermore, in such situations, the inevitable increase in the threshold of convection due to intensified radial stretching, as the fluid flows inward, seems to provide the means by which convection will cease once the fluid reaches the vicinity of the accretion radius $r_{\mathrm{a}} = GM/c_{\mathrm{s}}^2$ (where c_{s} is the speed of sound). However, the details of the inner boundary of the convective region cannot be studied within the framework of our model, since the accretion velocity approaches the speed of sound near the accretion radius.

By contrast, in the case of higher-luminosity solutions of equations describing the structure of convective accretion, the increase in luminosity as the fluid flows inward will sustain convection even at smaller radii. These solutions would be consistent with an everywhere subsonic settling of the incoming fluid onto a region of high density and temperature in the immediate vicinity ($r \lesssim r_{\mathrm{a}}$) of the black hole — at an accretion rate smaller than the Bondi rate. The structure at small radii could be supported by rotation of the inflowing fluid. The rotation can brake the (approximate) spherical symmetry of accretion only close to the black hole, where, due to the presence of a centrifugal barrier, a hot and dense disk or torus-like structure would form.

This brings us to the evolution of a hypothetical small black hole inside a solar-type star — the subject of Chapter 5 of this Thesis. Since we have restricted our discussion to optically thick accretion, we can follow the growth of the black hole for masses greater than about 10^{21} grams. (For smaller holes the photon mean free path is comparable to or larger than the accretion radius.)

As long as there are efficient mechanisms for braking the differential rotation in the accreting fluid, the fluid will loose enough angular momentum to proceed toward the black hole without being hindered by a centrifugal barrier. By "efficient" we mean that the extraction of angular momentum from the inflowing fluid should be sufficiently rapid so that the fluid accreting at the Bondi rate would lose most of its angular momentum before reaching the vicinity of the black hole.

In particular, we find that the braking of rotation by conventional viscosity, due to Coulomb collisions in the accreting plasma, is efficient only for black holes whose mass is smaller than roughly $10^{-11} M_{\odot}$.

An efficient braking at higher masses could be provided by magnetic torques. A pre-existing field of typical strength B_o would be amplified by differential rotation. The resulting winding of the field lines might, however, lead to reconnection of the lines and to a reduction of the field's ability to brake the differential rotation. The competition between the amplification and reconnection determines the black-hole mass range for which the magnetic braking would be efficient. As we show in Chapter 5, for B_o exceeding a few gauss, the maximum mass M_B for efficient braking by magnetic torques is primarily determined not by reconnection but rather by the limited winding of the magnetic field lines; the result is $M_B \approx 6 \times 10^{-8} M_{\odot} B_o^{3/4}$ [11].

For larger black-hole masses, the rotation of the Sun will finally have an opportunity to exert its influence. It is plausible that the formation of a torus in the vicinity of the black hole will lead to luminosities exceeding the Flammang luminosity, characteristic of optically thick, spherically symmetric accretion. Relying on our model of convection in accreting fluid, developed in Chapter 4, we are able to examine the transport of angular momentum by convection that will inevitably follow the increase in the luminosity. We conclude that, due to the convection-limited supply of angular momentum, the luminosity produced by the torus can never exceed a few percent of the total luminosity of the Sun — until at most three days before the hole completely devours the Sun. If the accretion rate during the final three days is less then about 20% of the Bondi rate, the luminosity and the total heat produced by the accretion cannot cause any change in the appearance of the Sun until tens of minutes before the Sun is destroyed. Presumably at that time, hydrodynamic effects from the final stages of the Sun's collapse should reach the surface of our star. By contrast, if the accretion proceeded at approximately the Bondi rate, despite the presence of the torus, the total energy output during the last three days could, in principle, grow large enough to cause observable effects.

Bibliography

[1] B. F. Schutz, Nature **323**, 310 (1986); A. Krolak and B.F. Schutz, Gen. Rel. Gravit., **19**, 1163 (1987). B. F. Schutz, Class. Quantum Gravity **6**, 1761 (1989).

[2] E. Hubble, Proc. Natl. Acad. Sci. **15**, 168 (1929).

[3] A. Sandage, Ann. Rev. Astron. Astrophys. **26**, 561 (1988); P.J.E. Peebles, *Principles of Physical Cosmology* (Princeton University Press, Princeton, 1993).

[4] S. Hawking, Mon. Not. R. Astron. Soc. **152**, 75 (1971).

[5] R.A. Flammang, MNRAS **199**, 833 (1982).

[6] E. S. Phinney, Astrophys. J. **380**, L17 (1991); R. Narayan, T. Piran, and A. Shemi, *ibid.* **379**, L17 (1991).

[7] A. Abramovici *et al.*, Science **256**, 325 (1992).

[8] W.A. Hiscock, Phys. Rev. D **39**, 1067 (1989).

[9] K.S. Thorne, R.H. Price and D.A. Macdonald, *Black Holes: The Membrane Paradigm* (Yale University Press, New Haven, 1986).

[10] V.P. Frolov and K.S. Thorne, Phys. Rev. D **39**, 2125 (1989).

[11] The data presently available from solar seismological observations do not provide information on magnetic fields in the interior of the Sun deeper than about one half of the solar radius. However, significant improvements might be possible in the near future; see, e.g., S. Turck-Chièze *et al.*, Phys. Reps. **230**, 57 (1993).

Chapter 2

Possibility of determining cosmological parameters from measurements of gravitational waves emitted by coalescing, compact binaries

(Originally appeared in Phys. Rev. D **48**, 4738 (1993).)

Abstract

We explore the feasibility of using LIGO/VIRGO gravitational-wave measurements of coalescing, neutron star/neutron-star (NS-NS) binaries and black-hole/neutron-star (BH-NS) binaries at cosmological distances to determine the cosmological parameters of our Universe. From the observed gravitational waveforms one can infer, as direct observables, the luminosity distance D of the source and the binary's two "redshifted masses," $M_1' \equiv M_1(1+z)$ and $M_2' \equiv M_2(1+z)$, where M_i are the actual masses and $z \equiv \Delta\lambda/\lambda$ is the binary's cosmological redshift. Assuming that the NS mass spectrum is sharply peaked about $1.4 M_\odot$, as binary pulsar and X-ray source observations suggest, the redshift can be estimated as $z = M_{\rm NS}'/1.4 M_\odot - 1$. The actual distance-redshift relation $D(z)$ for our Universe is strongly dependent on its cosmological parameters [the Hubble constant H_0, or $h_0 \equiv H_0/100{\rm km\ s^{-1} Mpc^{-1}}$, the mean mass density $\rho_{\rm m}$, or density parameter $\Omega_0 \equiv (8\pi/3H_0^2)\rho_{\rm m}$, and the cosmological constant Λ, or $\lambda_0 \equiv \Lambda/(3H_0^2)$], so by a statistical study of (necessarily noisy) measurements of D and z for a large number of binaries, one can deduce the cosmological parameters. The various noise sources that will plague such a cosmological study are discussed and estimated, and the accuracies of the inferred parameters are determined as functions of the detectors' noise characteristics, the number of binaries observed, and the neutron-star mass spectrum. The dominant source of error is the detectors' intrinsic noise, though stochastic gravitational lensing of the waves by intervening matter might significantly influence the inferred cosmological constant λ_0, when the detectors reach "advanced" stages of development. The estimated errors of parameters inferred from BH-NS measurements are embodied in Fig. 2.2 and can be described by the following rough analytic fits: $\Delta h_0/h_0 \simeq 0.02(N/h_0)(\tau\mathcal{R})^{-1/2}$, (for $N/h_0 \lesssim 2$) where N is the detector's noise level (strain/$\sqrt{\rm Hz}$) in units of the "advanced LIGO" noise level; $\mathcal{R}$ is the event rate in units of the best-estimate value, 100 ${\rm yr^{-1} Gpc^{-3}}$, τ is the observation time in years. In a "high density" universe ($\Omega_0 = 1$, $\lambda_0 = 0$) $\Delta\Omega_0 \simeq 0.3(N/h_0)^2(\tau\mathcal{R})^{-1/2}$, $\Delta\lambda_0 \simeq 0.4(N/h_0)^{1.5}(\tau\mathcal{R})^{-1/2}$, for $N/h_0 \lesssim 1$. In a "low density" universe ($\Omega_0 = 0.2$, $\lambda_0 = 0$), $\Delta\Omega_0 \simeq 0.5(N/h_0)^3(\tau\mathcal{R})^{-1/2}$, $\Delta\lambda_0 \simeq 0.7(N/h_0)^{2.5}(\tau\mathcal{R})^{-1/2}$, also for $N/h_0 \lesssim 1$. These formulae indicate that, if event rates are those currently estimated ($\sim$ 3 per year out to 200 Mpc), then when the planned LIGO/VIRGO detectors get to be about as sensitive as the so-called "advanced detector level," (presumably in the early 2000's), interesting cosmological measurements can begin.

1 Introduction and summary

1.1 Background

With construction now approved for the American LIGO(Laser Interferometer Gravitational-Wave Observatory) [1] and French/Italian VIRGO [2] kilometer-scale gravitational-wave detector systems, many researchers are looking forward to these facilities as opening a "new window onto the universe," when they go into operation near the end of the 1990s. Arguably, in addition to aiding current astronomical studies, the monitoring of gravitational waves is likely to provide us with a view of astrophysical phenomena and objects that will be extremely difficult or impossible to observe by conventional electromagnetic means. Among such phenomena are the coalescences of neutron-star/neutron-star (NS-NS), black-hole/neutron-star (BH-NS), and black-hole/black-hole (BH-BH) binaries at distances approaching cosmological. These binaries are systems like the famous binary pulsar PSR 1913+16, whose two bodies are gradually spiraling together as a result of losing energy and angular momentum to gravitational radiation. About three minutes before final coalescence, such a binary's gradually increasing gravitational-wave frequency (equal to twice its orbital frequency) should reach 10 Hz, which is the lower end of the LIGO/VIRGO frequency band. The three-detector LIGO/VIRGO network should then be able to monitor the final three minutes of inspiral, as the frequency sweeps upward from 10 Hz toward 1000 Hz.

Such coalescences are rare events, and therefore to see several per year, LIGO/VIRGO must look far beyond our galaxy. More specifically: Phinney, and independently Narayan, Piran, and Shemi [3] have estimated, from the statistics of successful and unsuccessful searches for "binary pulsars" in our galaxy (NS-NS binaries), that there is one NS-NS coalescence each 10^5 years in our galaxy (with a factor ~ 10 uncertainty at the "1 σ level"). They have then extrapolated out into the distant universe, using the plausible assumption that the NS-NS coalescence rate in any galaxy is proportional to its number of massive stars (NS progenitors), which in turn is proportional to the galaxy's observed luminosity in blue light (the color emitted primarily by massive stars). This extrapolation produced a NS-NS coalescence rate of about 3 per year within a distance of 200 Mpc from Earth, and an uncertainty of a factor ~ 2 in the distance for 3 per year. Interestingly, this NS-NS coalescence rate is about 100 times lower than the rate of formation of the massive main-sequence binaries that *could* become NS-NS binaries at the ends of their evolutions. This suggests that 99 percent of such massive binaries are disrupted during the supernova explosions that convert their normal stars into NS's.

The coalescence rate for BH-NS binaries is much less certain than for NS-NS binaries, since pulsar searches have not yielded any as yet. However, Phinney, and independently Narayan, Piran, and Shemi [3] argue that the BH-NS rate will be comparable to the NS-NS rate for the following reason: The main-sequence binary progenitors for BH-NS's are more massive and thus more rare than those for NS-NS's, but this is roughly compensated by the fact that it should be far harder to disrupt a BH-NS-forming system during its supernova outbursts—far harder because in this case, by contrast with the NS-NS one, during each of the two supernovae the companion is expected to be more massive than the exploding star and thus can gravitationally hang onto the exploding star's core with some ease. This (admittedly somewhat fragile) argument suggests, then, a rate of about 3 BH-NS coalescences per year out to 200 Mpc.

These estimated coalescence rates have been a major factor in setting the arm lengths of the LIGO/VIRGO gravitational wave detectors: With the chosen arm lengths, it is reasonable to expect "advanced" detectors in LIGO/VIRGO to reach out to distances $\gtrsim 1500$ Mpc for NS-NS coalescences and $\gtrsim 3000$ Mpc for BH-NS [1, 4] (though the earliest LIGO/VIRGO detectors may be a factor ~ 20 poorer than this).

By cross correlating the outputs of the three LIGO/VIRGO detectors (one in Hanford, Washington, one in Livingston, Louisiana, and one near Pisa, Italy), it should be possible to determine the location of a binary coalescence on the sky to within a $\sim$one square degree error box, and also to monitor the coalescence's two "gravitational waveforms," $h_+(t)$ and $h_\times(t)$ [5]. The two waveforms, produced during the last three minutes of binary inspiral, are precisely determined by the inspiraling bodies' masses and spins, the orientation of their orbit when the waves enter the LIGO/VIRGO band (most importantly the orbital inclination ι to our line of sight), and the binary's distance from earth [6, 7]. By comparing the observed, noise-infested waveforms with theoretically derived templates, the observers expect to determine the binary's parameters.

Theoretical simulations [7, 8] are beginning to give us some understanding of the accuracies of such parameter determinations. Of greatest importance for this paper are the following accuracy estimates: For the binary's "chirp mass" $M_c \equiv M_1^{3/5} M_2^{3/5}/(M_1 + M_2)^{1/5}$, an accuracy $\Delta M_c/M_c \simeq 0.01/\rho$; for the NS mass in a BH-NS binary, an accuracy $\Delta M_n/M_n \simeq 1.9/\rho$ where ρ is the total signal to noise ratio in the three detectors (which will be $\sim \sqrt{3} \times 5 \approx 9$ at the threshold for a believable detection of the binary's waves [7, 8], and $\gtrsim 11$ for the typical detected signal [4]); and for the distance to the source, an accuracy $\Delta D/D \simeq (3/\rho)\times$(a function of the inclination angle ι and position of the source on the sky that is of order unity).

Bernard Schutz [6] has pointed out that the statistical distribution of such gravitationally determined binary parameters can be used to probe the cosmological structure of our Universe.

Schutz has explored in considerable detail one variant of his cosmological idea: the combined use of gravitationally measured distances and electromagnetically measured redshifts to determine the Hubble constant H_0 (or equivalently $h_0 \equiv H_0/100\text{km s}^{-1}\text{Mpc}^{-1}$). This variant relies on assigning to each detected coalescence several possible redshifts, corresponding to the various electromagnetically observed clusters of galaxies within the gravitational-wave source's ~one square degree angular error box on the sky. Each electromagnetic redshift, combined with the gravitationally determined distance, gives a possible value of h_0. By seeing which value of h_0 keeps showing up over and over again and averaging it over many inspiral events, one can zero in on the true Hubble constant. Estimates [6] suggest that such measurements might succeed in determining h_0 to a few percent accuracy within a few years after the first detection of gravitational waves from coalescing binaries.

Unfortunately, this gravitational/electromagnetic approach to cosmology will probably be restricted to fairly nearby binaries (distances less than a few hundred Mpc), because at greater distances there will be too many clusters of galaxies in the gravitational error box for the method to work. This distance restriction may prevent the gravitational/electromagnetic approach from ever giving useful information about the Universe's other cosmological parameters: its density parameter $\Omega_0 \equiv (8\pi/3H_0^2)\rho_{\rm m}$ (where $\rho_{\rm m}$ is the mean mass density), and its dimensionless cosmological constant $\lambda_0 \equiv \Lambda/(3H_0^2)$ (where Λ is the familiar cosmological constant of dimension length^{-2} in geometric units, $c = 1$, $G = 1$).

A second, purely gravitational variant of Schutz's cosmological idea has hope of determining all three parameters, H_0, Ω_0, and λ_0. Krolak and Schutz [6] mention this variant in passing, but neither they nor anyone else has yet explored it in detail. Such an exploration is the objective of this paper.

1.2 The method of determining h_0, Ω_0, and λ_0

The theoretical foundation for this purely gravitational variant of the original Schutz's idea is the redshift-distance relation $D(z)$ for distant objects, which depends sensitively on the three cosmological parameters. This relation is briefly reviewed in Sec. 2. In the electromagnetic astronomical studies conducted so far, it has been possible to determine the redshifts z of distant astrophysical objects with fairly high accuracy. The main obstacle continues to be, unfortunately, the uncertainty of the intrinsic luminosities, which impairs the determination of distances D.

This situation is, in a way, reversed for gravitational waves from merging binaries: The distance to the source (actually the "luminosity distance" D) is a direct observable; it can be read directly off the time evolving waveforms [6]. However, the redshift z is *not* a direct, gravitational-wave observable.

Fortunately, for binaries at cosmological distances, the redshift can be inferred indirectly. As we elaborate in Sec. 3, all quantities intrinsic to the binary with physical dimension $(\text{mass})^p$ [or $(\text{length})^p$] enter the waveforms observed at earth multiplied by factor $(1+z)^p$. In particular, the waveforms contain, as a direct observable, the "cosmologically redshifted mass" $M_\mathrm{n}' \equiv M_\mathrm{n}(1+z)$ of the binary's NS (or NS's). In our own galaxy, radio and X-ray observations have strongly indicated that the mass distribution of NS's in binaries is sharply peaked around $1.4M_\odot$. Assuming that this will be true also for distant, coalescing NS-NS and BH-NS systems (and, crucially, that the NS mass spectrum is independent of redshift at $z \gtrsim 1$, which is very plausible), one can estimate the redshift as $(1+z) = M_n'/1.4M_\odot$. This is the best one can do for a BH-NS binary; but for a NS-NS system, the redshifted chirp mass $M_c' \equiv (M_1'M_2')^{3/5}/(M_1'+M_2')^{1/5}$ can provide a somewhat more accurate redshift estimate $[(1+z) = M_c'/1.2M_\odot]$, since M_c' is measured far more accurately than the individual, redshifted NS masses M_1' and M_2' (see previous subsection).

For each observed coalescence, the deduced luminosity distance D and redshift z will be influenced by several noise sources: (i) noise intrinsic to the detectors, which contaminates the waveforms and thereby alters the inferred D and z; (ii) a deviation of the actual NS mass or chirp mass from the "standard" value ($1.4M_\odot$ or $1.2M_\odot$); and (iii) gravitational lensing by inhomogeneities of the Universe's gravitational field, through which the gravitational waves propagate. (By contrast with electromagnetic astronomy, there is no significant noise introduced by any other propagation effects; for example, absorption, scattering, and reddening by interaction with intervening matter are utterly negligible for gravitational waves [5].)

The noise-induced errors in D and z will cause the detected coalescence events to "scatter" considerably away from the correct distance-redshift relation $D(z)$; and, therefore, we must develop a reliable statistical method of finding from the data a "best fit" $D(z)$ curve that is as close as possible to the real one. Developing such a method is a central goal of this paper.

Our method is based on computing *a priori* distributions of events in the redshift-distance (z-D) plane, assuming that the binaries' true z and D (their "starting points" before noise infects them) lie on the theoretical redshift-distance curve $D(z)$ corresponding to a specific set of values of the cosmological parameters h_0, Ω_0, λ_0. These *a priori* distributions (one for each $\{h_0$, Ω_0, and $\lambda_0\}$) can then be compared with the observed distributions, and from that comparison, using the method of "maximum likelihood," one can deduce "best-fit" values of, and uncertainties for h_0, Ω_0, and λ_0. In the limit of a large number of events, the average errors in the cosmological parameters are given by the Cramer-Frechet-Rao (CFR) limit [22], which we discuss in Appendix B and Sec. 4.

In Sec. 4 we develop concepts and formulas for computing the *a priori* z-D distributions. Crucial ingredients for the computation are: (i) The spectral density of the detectors' noise and formulas for how that noise influences the measured distances D and redshifted NS and chirp masses, M_n' and M_c'. (ii) The statistical distribution of actual NS and chirp masses in coalescing binaries. These first two ingredients very strongly influence the *a priori* z-D distributions and the resulting values and uncertainties of h_0, Ω_0, and λ_0. It therefore is fortunate that these ingredients are likely to be rather well understood by the time the cosmological studies begin.

Not so well understood, but fortunately less influential, will be the following ingredients: (iii) the statistical distribution of sources along the real redshift-distance curve (i.e., the event rate as a function of distance from Earth), (iv) the statistical distribution of the actual BH masses in BH-NS binaries, and (v) the spectrum of gravitational-lens-producing gravitational inhomogeneities in the Universe. For concreteness, in this paper we make the plausible assumption that out to the relevant redshifts ($z \sim 3$ for both the NS-NS and BH-NS binaries), the event rate on a "per unit comoving volume" basis is independent of distance from Earth. In Sec. 4 (especially Fig. 2.6) we explore quantitatively the influence of uncertainties in the BH mass spectrum and show that it will be sufficient to know the spectrum (from gravitational wave measurements) to an accuracy of $\sim 2M_\odot$ (out of a typical 10 or $20M_\odot$). In Sec. 5 (especially Fig. 2.8) we explore the influence of gravitational lensing and show that uncertainties in the Universe's gravitational inhomogeneities will not seriously affect the deduced Hubble constant h_0, but they may introduce systematic errors into the determination of the density parameter Ω_0 and the cosmological constant λ_0.

1.3 Estimates of the accuracy with which h_0, Ω_0, and λ_0 can be determined

In Sec. 4 we estimate the accuracy with which this method can determine h_0, Ω_0, and λ_0. Our estimate is obtained by constructing model *a priori* distributions in the z-D plane and applying to them the maximum likelihood method in the CFR limit. The assumptions that go into our model distributions are discussed at length in Secs. 3 and 4. The more important of these assumptions, stated in brief, are:

(i) The detectors' noise spectrum has the shape shown in Fig. 2.3, for which the signal-to-noise ratio ρ for the binary's inspiral waveforms, in each of the three detectors, is given by Eqs. (22) and (23). In this paper we embody the influence of the detector noise on ρ in the distance r_0 [Eqs. (24) and (25)] of a binary that would produce $\rho = 1$ for the relative orientation of the source and the detector giving the strongest signal. As currently estimated, for the "advanced" noise levels toward which LIGO/VIRGO detectors will evolve over time, $r_0 \simeq$ 8Gpc for a NS-NS binary, and $r_0 \simeq$ 17Gpc for a BH-NS binary with the black hole mass $M_b = 10M_\odot$ [4].

(ii) The accuracy with which a NS-NS binary's redshifted chirp mass is measured is $\Delta M_c'/M_c' \simeq 0.01/\rho$ (which is so good that its errors have negligible influence on the inferred cosmological parameters). The accuracy with which the redshifted neutron star mass in a BH-NS system will be measured is $\Delta M_n' = 1.9/\rho$ [Eq. (2.47)].

(iii) The accuracy with which the luminosity distance is measured is given by Eq. (2.47), where ε is a function of source's inclination angle and its position on the sky and varies in the range $2 \lesssim \varepsilon \lesssim 7$; see Fig. 2.4.

(iv) The actual spread in NS masses is $\delta M_n / < M_n >= 0.2$ (based on fairly numerous but not highly accurate X-ray binary observations) or 0.05 (based on fewer, but much more accurate radio binary pulsar observations).

(v) The distribution function for the observed distances and redshifts is log normal [Eq. (2.60)], with standard deviations that are determined by assumptions (ii), (iii), (iv), and are given by Eqs. (2.47) and (2.63) for NS-NS binaries or Eq. (2.67) for BH-NS binaries.

(vi) The rate of mergers is constant per unit of co-moving volume, Eq. (40) with $N_{200} = 3$ NS-NS events and 3 BH-NS events in a sphere of comoving radius 200 Mpc.

(vii) Noise due to gravitational lensing is unimportant.

(viii) The BH's in BH-NS systems (for simplicity and concreteness) all have masses $M_{\rm BH} = 10 M_{\odot}$.

(ix) Observational data are collected for one year.

With these assumptions, the estimated errors in the determination of the cosmological parameters, are as shown in Fig. 2.1 (for NS-NS binaries) and Fig. 2.2 (for BH-NS binaries). The errors are plotted vertically as a function of the horizontally plotted detector sensitivity, which is embodied in the parameter r_0 of assumption (i) above. (Recall that $r_0 \simeq 8$ Gpc for advanced detectors and NS-NS binaries, and 17 Gpc for advanced detectors and BH-NS binaries – as projected at present.)

Note the typically smaller errors for the "compact" universe. This is in part due to the larger number of events detected in a universe with smaller average distances between galaxies (see Fig. 2.5). In addition, a compact universe allows the observer to better access the distances (redshifts) at which the contrast in $D(z)$ for different values of Ω_0 and λ_0 is more apparent.

Also note that for both cosmologies, "advanced" LIGO-type detectors' observations of NS-NS binaries ($r_0 \approx 8$Gpc) could give fairly accurate measurements of the Hubble constant. On the other hand, in order to obtain the other two cosmological parameters, Ω_0 and λ_0, with any respectable accuracy one would have to develop the detectors even further. Of course, since all errors are inversely proportional to the square root of the number of detected events, an alternative, at least in a compact universe, might simply be to have a lot of patience and observe for many (order of 10) years.

The errors in the BH-NS case are only slightly larger than for NS-NS binaries at a given r_0. Therefore, the better accuracy of redshift determination based on the chirp mass of NS-NS binaries does not seem to be as important as one might expect. Due to the larger r_0 in the case of BH-NS binaries, the advanced LIGO-type detectors could give interesting measurements of all three basic cosmological

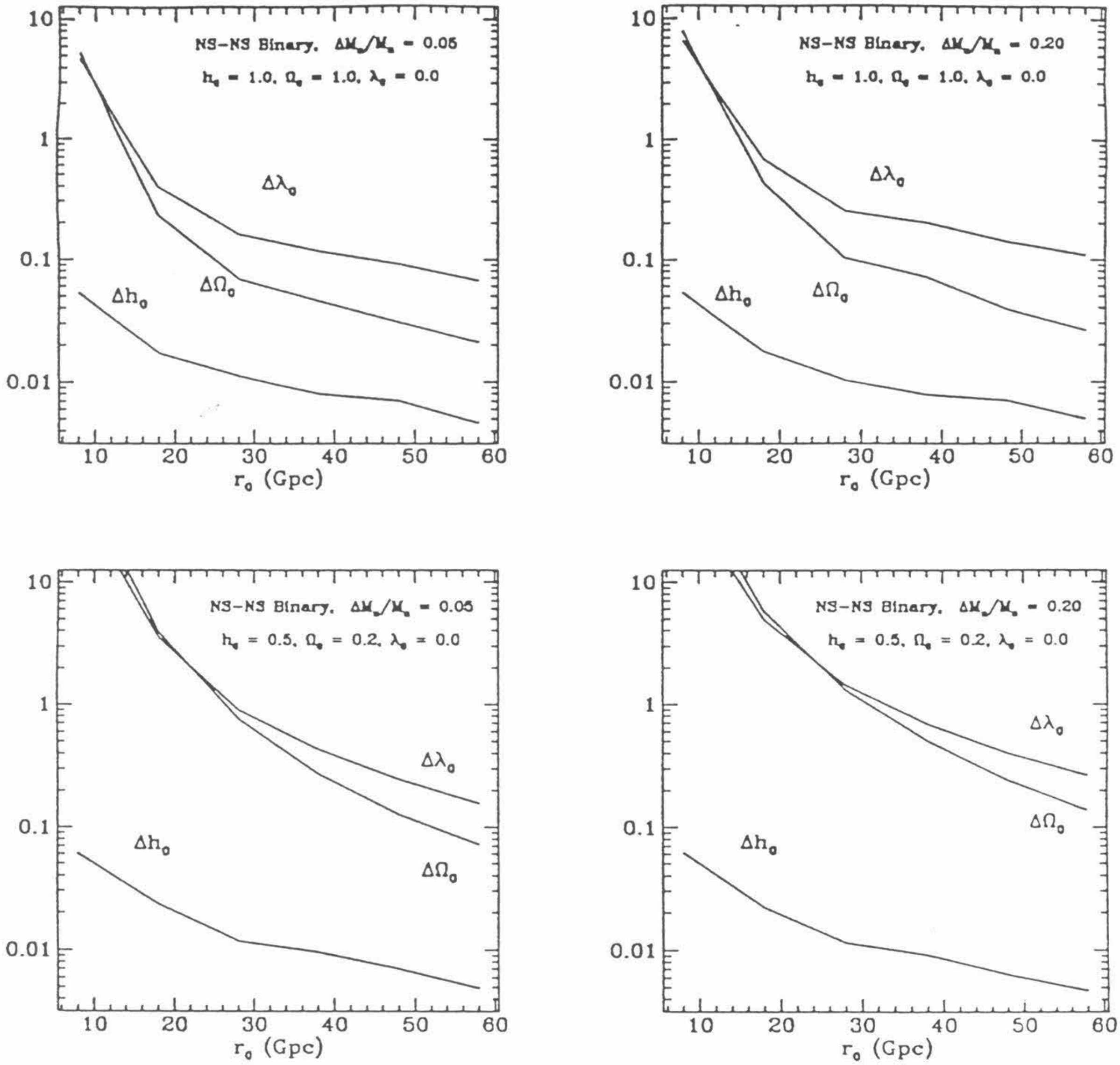

Figure 2.1: Estimates of errors in the determination of cosmological parameters for the case of NS-NS binaries. The projected value of r_0 for each of the three detectors of an advanced LIGO/VIRGO type is 8Gpc.

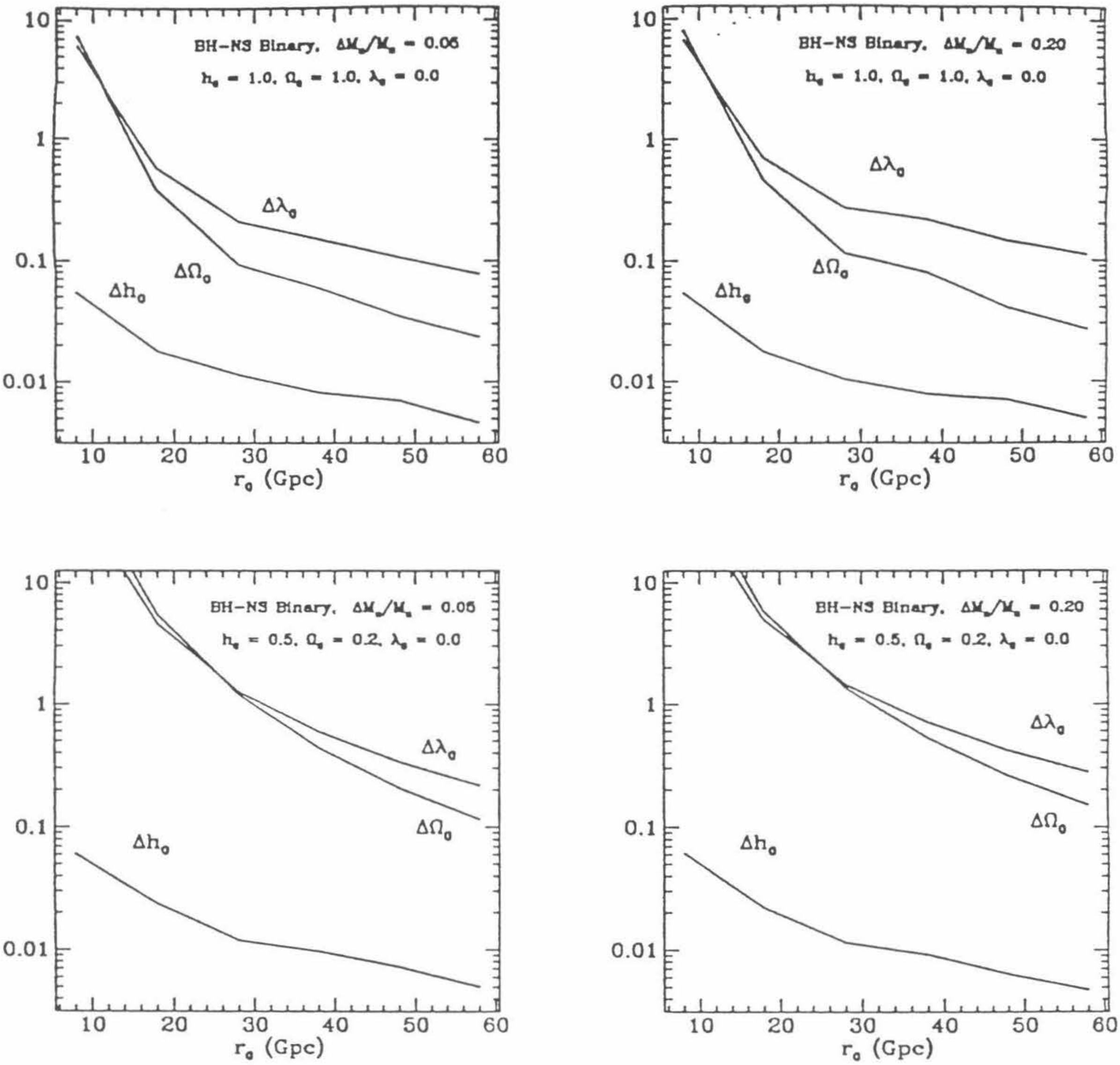

Figure 2.2: Estimates of errors in the determination of cosmological parameters for the case of BH-NS binaries assuming a known, infinitely sharp black hole mass function. The projected value of r_0 for each of the three detectors of an advanced LIGO/VIRGO type is 17Gpc.

parameters in the "compact" universes. In the case of a "spacious" universe, however, further improvements in the detector and/or longer observation times would still be needed.

Obviously, these estimated errors will scale as 1 over the square root of the number of events observed, i.e., as $1/\sqrt{N_{200}\tau}$, where N_{200} is the event rate in a comoving volume that has radius 200 Mpc, and τ is the observing time in years. Combining this with rough analytic fits to the curves in Figs. 2.1 and 2.2, we obtain the results quoted in the abstract.

2 Friedmann cosmological models — an overview

The main purpose of this section is to establish the notation and review the basic equations that will be needed later. Much more detail can be found in the opulent literature on the subject [10].

Despite the apparent clumpiness even at scales of order 100Mpc, it seems [11] adequate to use homogeneous and isotropic Friedmann models to describe the universe at still larger scales. The assumptions of homogeneity and isotropy inevitably lead to the Friedmann metric [10]

$$ds^2 = -dt^2 + R^2(t)\left(\frac{dr^2}{1-kr^2} + r^2(d\theta^2 + \sin^2\theta d\phi^2)\right). \tag{2.1}$$

in which the evolution of the scale factor R is described by the equation

$$\left(\frac{\dot{R}}{R}\right)^2 = \frac{8\pi}{3}\rho_{\mathrm{m}} + \frac{\Lambda}{3} - \frac{k}{R^2}, \tag{2.2}$$

where ρ_{m} is the total matter density, Λ is the cosmological constant and $\dot{R} \equiv dR/dt$. Equation (2.2) simplifies if we define the following parameters

$$\Omega_0 \equiv \frac{8\pi}{3}\frac{\rho_{\mathrm{m}_0}}{H_0^2}, \qquad \lambda_0 \equiv \frac{\Lambda}{3H_0^2}, \qquad \Omega_k \equiv -\frac{k}{R_0^2 H_0^2}, \tag{2.3}$$

and

$$a = \frac{R}{R_0} = \frac{1}{1+z}. \tag{2.4}$$

Here the subscript $_0$ denotes the present values, z is the redshift and $H_0 = (\dot{R}/R)_0 = h_0 \times 100$ km/(sMpc) is the Hubble constant. The three parameters defined by Eqs. (2.3) are related to each other by the equation

$$\Omega_0 + \lambda_0 + \Omega_k = 1. \tag{2.5}$$

With the additional observation that the post-recombination universe can be treated as pressureless [$\rho_{\mathrm{m}} = \rho_{\mathrm{m}_0}(R_0/R)^3$], we obtain

$$\frac{1}{H_0^2}\dot{a}^2 - \left(\frac{\Omega_0}{a} + \lambda_0 a^2\right) = 1 - \Omega_0 - \lambda_0. \tag{2.6}$$

Obviously, the Friedmann models, and, presumably, the universe at very large scales, are completely described only by the three parameters $H_0(h_0)$, Ω_0 and λ_0.

At least in principle, the three cosmological parameters can be inferred through their imprint on observable quantities. Among the observables we will concentrate on the relation between luminosity distance and redshift. The luminosity distance, D, of a source of radiation is defined as $D \equiv \sqrt{L/4\pi F}$ where L is the intrinsic luminosity of the isotropically radiating source and F is the flux detected by the observer. In terms of the Friedmann radial coordinate r (see Eq. (2.1)) of the source and its redshift, the value of the luminosity distance is

$$D = (1 + z) r R_0. \tag{2.7}$$

Using Eq. (2.6) and the equation of a null ray propagating from the source to the observer at $r = 0$,

$$\frac{dR}{\dot{R}R} = -\frac{dr}{\sqrt{1 - kr^2}}, \tag{2.8}$$

one obtains

$$D = \frac{1+z}{H_0} \times \begin{cases} \frac{\sin\left(|\Omega_k|^{1/2}\Gamma(z)\right)}{|\Omega_k|^{1/2}} & \text{for } \Omega_0 + \lambda_0 > 1 \\ \Gamma(z) & \text{for } \Omega_0 + \lambda_0 = 1 \\ \frac{\sinh\left(|\Omega_k|^{1/2}\Gamma(z)\right)}{|\Omega_k|^{1/2}} & \text{for } \Omega_0 + \lambda_0 < 1, \end{cases} \tag{2.9}$$

where

$$\Gamma(z) = \int_0^z \frac{dz'}{\left(\Omega_0(1 + z')^3 + \Omega_k(1 + z')^2 + \lambda_0\right)^{1/2}}, \tag{2.10}$$

and $\Omega_k = 1 - \Omega_0 - \lambda_0$. In the special case of vanishing cosmological constant, the above expressions reduce to

$$D(z) = \frac{2}{H_0\Omega_0^2}\left[\Omega_0 z - (2 - \Omega_0)(\sqrt{1 + \Omega_0 z} - 1)\right]. \tag{2.11}$$

Among other measures of distance that we will be using later are the angular diameter distance $D_A(z)$ and "corrected luminosity" or "proper motion" distance r_c, simply related to the luminosity distance by

$$\begin{aligned} D_A &= D/(1+z)^2, \\ r_c &= D/(1+z). \end{aligned} \tag{2.12}$$

Obviously, if we could measure both the redshifts and the distances of a number of sources, that would allow us to determine all the Friedmann cosmological parameters. As we elaborate in this paper, the detection of gravitational waves from distant coalescing binaries might provide just such an opportunity.

3 Gravitational waves emitted by coalescing binaries and their detection

3.1 Elements of gravitational wave detection

The proposed application of gravitational waves from coalescing binaries to cosmological measurements relies primarily on the relative "simplicity" of the physics involved. Namely, the wave forms produced by compact binaries can, at least in principle, be computed with high accuracy. They depend on relatively few parameters: the masses of the binary members, their spins, and the orbital orientation at the time the waves sweep into the detector's frequency band. Furthermore, the propagation of the gravitational waves from the source to the earth is not complicated by interaction with intervening matter that affects electromagnetic radiation — absorption, scattering etc. The only potentially significant propagation effect, gravitational lensing by inhomogeneities in the matter distribution, will be discussed in Sec. 5.

The wave emitted by inspiraling binaries reaches (at $f \simeq 10\text{Hz}$) the detector's observable frequencies long after the orbit has been circularized by gravitational radiation reaction. At that time post-Newtonian corrections to the amplitude and frequency of the wave are still not larger than about 10% and the wave's two waveforms are well described by the Newtonian quadrupole formula [5]

$$\begin{aligned} h_+ &= \frac{1}{2}(1+\cos^2\iota)\mathrm{Re}h_c(t), \\ h_\times &= \pm(\cos\iota)\mathrm{Im}h_c(t), \end{aligned} \tag{2.13}$$

where

$$h_c(t) = 4\frac{M_c}{r}\left(\pi M_c f\right)^{2/3} \exp\left(i2\pi\int^t f dt\right). \tag{2.14}$$

Here Re and Im denote the real and imaginary part respectively, ι is the orbit's inclination angle (the angle of the orbital angular momentum to the line of sight), $M_c = (M_1 M_2)^{3/5}/(M_1 + M_2)^{1/5}$ is the so called "chirp mass" (M_1 and M_2 are the binary components' masses) and r is the distance from the detector to the source. For the moment we assume that the source is close enough to make effects associated with the curvature and expansion of the universe negligible. The frequency f grows with time as

$$f(t) = \frac{1}{\pi M_c}\left(\frac{5}{256}\frac{M_c}{t_0 - t}\right)^{3/8}. \tag{2.15}$$

In later phases of inspiral post-Newtonian corrections grow to about 20% at 100Hz and 100% at 1000Hz [7]. In addition to the parameters already present in the Newtonian order waveforms (2.13), those corrections will depend on the spins of the binary companions and, more importantly, on different combinations of the masses M_1, M_2. Thus, by comparing the measured waveforms with theoretically computed templates, the masses and spins can be determined. Naturally, the inevitable noise in the detector will introduce a certain error in this determination. Nevertheless, the known statistical properties of the noise will make it possible to estimate the errors together with the parameters themselves [8].

The response of the j'th member in a set of LIGO-type detectors is a linear combination of the wave forms (2.13)

$$h_j = F_{+_j}(\alpha,\beta,\gamma;\theta,\phi,\psi)h_+ + F_{\times_j}(\alpha,\beta,\gamma;\theta,\phi,\psi)h_\times. \tag{2.16}$$

Functions F_{+_j} and $F_{\times_j}$ depend, among other parameters, on detector's geographic longitude α, latitude β, and the angle γ from the local parallel anticlockwise to the "$\hat{\mathbf{a}}$" arm. For instance, at $\gamma = 0$ the arm directed along the unit vector $\hat{\mathbf{a}}$ points eastward along the parallel, while the other arm, directed along the unit vector $\hat{\mathbf{b}}$ ($\hat{\mathbf{a}}\cdot\hat{\mathbf{b}} = 0$) points northward along the meridian. In addition, θ and ϕ are the standard geocentric polar coordinates of the source of radiation where the pole ($\theta = 0$) coincides with the northern pole, while the $\theta = \pi/2, \phi = 0$ axis is drawn from the center of the earth through the intersection of the Greenwich meridian with the earth's equator. ψ is the angle between the vector ∂_θ at the source and the axis x' of the "wave frame" (in the plane orthogonal to the line of sight to the source) in which h_+ and $h_\times$ were defined [5]. The basic steps in the derivation of functions F_{+_j} and $F_{\times_j}$ are outlined in Appendix A.

A quantity of principal importance for detection of gravitational waves and binary parameter estimation is the signal to noise ratio which for the j'th detector is

$$\rho_j = (< h_j | h_j >)^{1/2} . \tag{2.17}$$

We have introduced here a scalar product, which for two real functions of time, $m_1(t)$ and $m_2(t)$, is defined as

$$< m_1 | m_2 > \equiv 4 \int_0^\infty \Re \left(\tilde{m}_1^*(f) \tilde{m}_2(f) \right) \frac{df}{S_h}, \tag{2.18}$$

where $\tilde{m}_1$ and $\tilde{m}_2$ are the Fourier transforms of functions m_1 and m_2,

$$\tilde{m}(f) = \int_{-\infty}^{\infty} e^{i 2\pi f t} m(t) dt, \tag{2.19}$$

and $S_h(f)$ is the spectral power of the noise [5].

Using the Fourier transform of the detector response h_j

$$\tilde{h}_j(f) = [F_{+_j} \frac{1}{2}(1+v^2) + i F_{\times_j} v] \tilde{h}_0(f), \tag{2.20}$$

where $v \equiv \cos \iota$, and $\tilde{h}_0$, which can be obtained [8] from Eqs. (2.13)-(2.15)

$$\tilde{h}_0(f) = \frac{M_c^2}{r} \sqrt{\frac{5\pi}{24}} \left(\pi M_c f \right)^{-7/6} e^{i[\frac{\pi}{4} + 2\pi f t_0 + \frac{3}{128}(\pi M_c f)^{-5/3}]}, \tag{2.21}$$

one can derive the j'th detector signal to noise ratio

$$\rho_j = \chi_j(\alpha, \beta, \gamma; \theta, \phi, \psi, \iota) \frac{r_0}{r}, \tag{2.22}$$

where

$$\chi_j = \left(F_{+_j}^2 \frac{1}{4}(1+v^2)^2 + F_{\times_j}^2 v^2 \right)^{1/2}, \tag{2.23}$$

$(0 < \chi < 1)$. r_0 is a function of the binary chirp mass M_c, the minimum S_m of the noise spectral power and the frequency f_m at which the minimum occurs $(S_m \equiv S_h(f_m))$ [1, 5]; see Fig 2.3.

For a binary consisting of a black hole and a neutron star, the value of r_0 can be estimated as [8]

$$r_0 \simeq 28 \mathrm{Gpc} \left(\frac{10^{-24} \mathrm{Hz}^{-1/2}}{\sqrt{S_m}} \right) \left(\frac{70 \mathrm{Hz}}{f_m} \right)^{2/3} \left(\frac{M_c}{3 M_\odot} \right)^{5/6} . \tag{2.24}$$

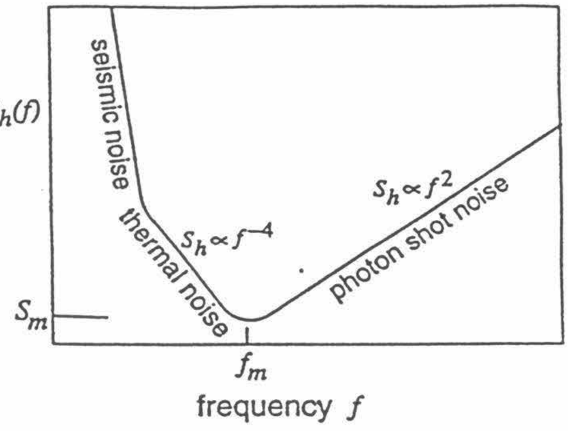

Figure 2.3: The expected noise spectrum for broad-band LIGO/VIRGO gravitational wave detectors [1, 4]. The transition frequency between thermal noise and seismic noise, and the slope of the seismic noise have a negligible influence on the issues discussed in this paper.

In the above expression we have taken as fiducial the chirp mass corresponding to a $10M_\odot$ black hole and a $1.4M_\odot$ neutron star. For the case of a pair of neutron stars, the relevant value is

$$r_0 \simeq 14\text{Gpc}\left(\frac{10^{-24}\text{Hz}^{-1/2}}{\sqrt{S_m}}\right)\left(\frac{70\,\text{Hz}}{f_m}\right)^{2/3}\left(\frac{\mathcal{M}_c}{1.2M_\odot}\right)^{5/6}. \tag{2.25}$$

The numerical value of the noise level ($\sqrt{S_m}$) used in Eqs. (2.24) and (2.25) is the order of magnitude of the noise predicted for the "advanced" LIGO/VIRGO detectors. At the time of the writing of this article it is estimated $\sqrt{S_m} \simeq 1.7\ 10^{-24}\text{Hz}^{-1/2}$ [4], corresponding to $r_0 \simeq 8$Gpc for NS-NS binaries and $r_0 \simeq 17$Gpc for BH-NS binaries.

Determination of the distance to the source requires the knowledge of its position on the sky which can be obtained from the time delays between signal arrivals in three detectors. As we stated in the introduction, three is indeed the number of detectors planned for the early next century and the number we assume in this article.

On the other hand, to eliminate "spurious" detections we will demand that the signal to noise ratio ρ_{min} in the detector giving the weakest response to a given binary coalescence event be at least five [7]

$$\rho_{\text{min}} \equiv \chi_{\text{min}}\frac{r_0}{r} \geq 5. \tag{2.26}$$

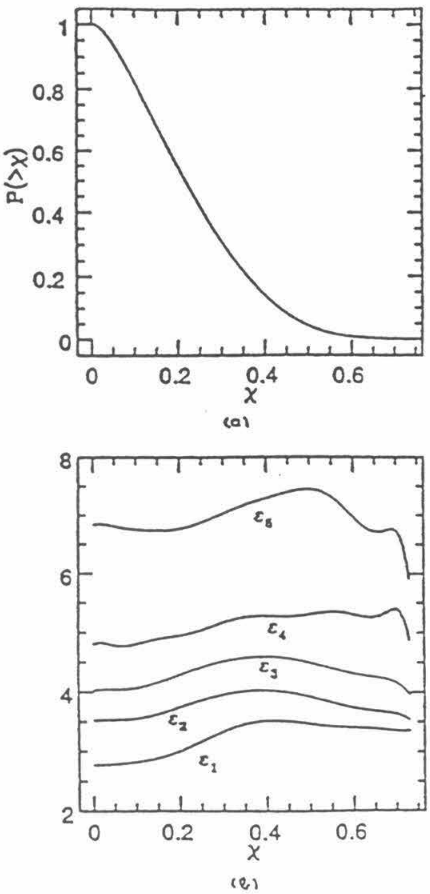

Figure 2.4: (a)Probability $P(>\chi)$ of $\chi_{\rm min}$ exceeding χ. (b)Functions $\varepsilon_k(\chi)$ which determine the error in distance estimation. Any binary whose orbit orientation and position on the sky yield $\chi_{\rm min} \geq \chi$ is assigned one of the five values $\varepsilon_k(\chi)$ with equal probabilities.

Thus, statistically speaking, of all the waves arriving from sources with same M_c and r, and being observed by three detectors with identical noise properties, only those with $\chi_{\rm min} \geq \bar{\chi}(r) \equiv 5r/r_0$ will be used for distance determination.

For our cosmological applications it will be important to know the probability $P(>\chi)$ of $\chi_{\rm min}$ exceeding a certain value χ. This probability function, obtained by a Monte-Carlo method is shown in Fig. 2.4(a). The three detectors are supposed to be constructed in Washington state ($\alpha \approx -120^o, \beta \approx 45^o, \gamma \approx 130^o$), Louisiana ($\alpha \approx -90^o, \beta \approx 30^o, \gamma \approx 200^o$), and Italy near Piza ($\alpha \approx 13^o, \beta \approx 45^o, \gamma = 0^o$(presumed)). The sources were assumed isotropically distributed over the sky, with an isotropic distribution of binary orbital planes.

3.2 Distance determination

Since the source's position on the sky can be obtained rather accurately (to better than one square degree [6]), we will assume that θ and ϕ are exactly known. Then we will try to estimate together the three remaining parameters ($r, v \equiv \cos\iota, \psi$) entering the amplitude of the signal, while leaving M_c, along with the other parameters appearing in post-Newtonian corrections (see below), to extraction from the phase (time dependence) of the signal. This approximate scheme is aimed at yielding rough estimates of distance determination errors. We thus disregard possible but, most likely, not very significant contribution from other parameters to the errors in r, v and ψ.

The signals obtained from three detectors can be represented by the column

$$\mathbf{h} \equiv \begin{pmatrix} h_1 \\ h_2 \\ h_3 \end{pmatrix} . \tag{2.27}$$

The inferred parameters τ ($\tau_1 = r, \tau_2 = v, \tau_3 = \psi$) are those that maximize the maximum likelihood function [12]. They are thus obtained from equation

$$< \mathbf{n} + \mathbf{h}(\tau_{(0)}) - \mathbf{h}(\tau) | \mathbf{h}_{,\mu} >= 0, \tag{2.28}$$

where $\mathbf{n}$ is the noise present in the three detectors at the detection, $\mathbf{h}(\tau_{(0)})$ is the original (uncontaminated) signal, $\mathbf{h}(\tau)$ is the best-fit template, and $\mathbf{h}_{,\mu}$ is the partial derivative with respect to the μ'th parameter. The scalar product in Eq. (2.28) is naturally related to the scalar product defined in Eq. (2.18) — for instance:

$$< \mathbf{n} | \mathbf{h}_{,\mu} > \equiv \sum_{j=1}^{3} < n_j | h_{j,\mu} > . \tag{2.29}$$

Expecting relatively small deviations $\Delta\tau \equiv \tau - \tau_{(0)}$, we expand Eq. (2.28) around $\tau_{(0)}$ up to the second order in noise strength and $\Delta\tau$

$$< \mathbf{n} - \mathbf{h}_{,\nu} \Delta\tau_\nu - \frac{1}{2} \mathbf{h}_{,\nu\lambda} \Delta\tau_\nu \Delta\tau_\lambda | \mathbf{h}_{,\mu} + \mathbf{h}_{,\mu\nu} \Delta\tau_\nu >, \tag{2.30}$$

where all derivatives are evaluated at $\tau_{(0)}$. To first order in $\Delta\tau$ we obtain

$$\begin{aligned} \overline{\Delta\tau_\mu \Delta\tau_\nu} &= \left(\mathrm{G}^{-1}\right)_{\mu\lambda} \left(\mathrm{G}^{-1}\right)_{\nu\eta} < \mathbf{h}_{,\lambda} \overline{| \mathbf{n} >< \mathbf{n} |} \mathbf{h}_{,\eta} > \\ &= \left(\mathrm{G}^{-1}\right)_{\mu\nu} , \end{aligned} \tag{2.31}$$

where $G_{\mu\nu} =< \mathbf{h}_{,\mu} | \mathbf{h}_{,\nu} >$, $\mathbf{G}^{-1}$ is the inverse of $\mathbf{G}$, and overlining denotes statistical ensemble average.

From Eq. (2.20), bearing in mind the spin-2 property of gravitational waves, $F_{+,\psi} = 2F_{\times}$ and $F_{\times,\psi} = -2F_{+}$, and using $x = r/r_{(0)}$ ($r_{(0)}$ is the true value of distance) instead of r, we obtain the six independent components of matrix $\mathbf{G}$:

$$
\begin{aligned}
G_{xx} &= [\mathcal{F}_{++}\frac{1}{4}(1+v^2)^2 + \mathcal{F}_{\times\times}v^2]\left(\frac{r_0}{r}\right)^2, \\
G_{xv} &= -[\mathcal{F}_{++}\frac{1}{2}(1+v^2)v + \mathcal{F}_{\times\times}v]\left(\frac{r_0}{r}\right)^2, \\
G_{x\psi} &= -\mathcal{F}_{+\times}[\frac{1}{2}(1+v^2)^2 - 2v^2]\left(\frac{r_0}{r}\right)^2, \\
G_{vv} &= [\mathcal{F}_{++}v^2 + \mathcal{F}_{\times\times}]\left(\frac{r_0}{r}\right)^2, \\
G_{v\psi} &= \mathcal{F}_{+\times}(v^2-1)v\left(\frac{r_0}{r}\right)^2, \\
G_{\psi\psi} &= 4G_{xx},
\end{aligned}
\tag{2.32}
$$

where

$$
\mathcal{F}_{++} \equiv \sum_{j=1}^{3} F_{+_j}^2, \quad \mathcal{F}_{\times\times} \equiv \sum_{j=1}^{3} F_{\times_j}^2, \quad \mathcal{F}_{+\times} \equiv \sum_{j=1}^{3} F_{+_j}F_{\times_j}. \tag{2.33}
$$

We see from Eqs. (2.31) and (2.32) that the errors are proportional to r/r_0 if $\det(\mathbf{G}) \neq 0$. For $v \simeq 1$, however, $\det(\mathbf{G}) \simeq 0$, which is caused by vectors $\mathbf{h}_{,x}$ and $\mathbf{h}_{,v}$ being collinear:

$$
\mathbf{G} = \left(\frac{r_0}{r}\right)^2 (\mathcal{F}_{++} + \mathcal{F}_{\times\times}) \begin{pmatrix} 1 & -1 & 0 \\ -1 & 1 & 0 \\ 0 & 0 & 4 \end{pmatrix}. \tag{2.34}
$$

In other words, in the treatment linear in $\Delta\tau$, discussed so far, the combination $\Delta x + \Delta v$ can be arbitrarily large. Of course, as we depart farther from $\tau_{(0)}$ we need to include higher derivatives and powers of $\Delta\tau$ as we have done in Eq. (2.30). For the realizations of noise $\mathbf{n}_\mathrm{d}$ which "push" the inferred parameters along the "degenerate" ray $\Delta\tau_d$ ($\Delta x_\mathrm{d} \equiv \Delta r_\mathrm{d}/r_{(0)} = \Delta v_\mathrm{d}$, $\Delta\psi = 0$), which implies $\mathbf{h}_{,\nu}\Delta\tau_\nu = 0$ at $v_{(0)} = 1$, we obtain

$$
< \mathbf{n}_\mathrm{d} | \mathbf{h}_{,\mu} > -\frac{1}{2} < \mathbf{h}_{,\nu\eta} | \mathbf{h}_{,\mu} > \Delta\tau_\mathrm{d}^{\nu} \Delta\tau_\mathrm{d}^{\eta} = 0, \tag{2.35}
$$

to the second order in $\Delta\tau_\mathrm{d}$. From the solution of this equation

$$
(\Delta x)^4 = 4\frac{< \mathbf{h} | \mathbf{n}_\mathrm{d} >< \mathbf{n}_\mathrm{d} | \mathbf{h} >}{\mathcal{F}_{++}^2}, \tag{2.36}
$$

we can estimate a rough upper limit on Δx:

$$\begin{aligned}\Delta x \lesssim & \left(4\frac{\overline{<\mathbf{h}|\mathbf{n}><\mathbf{n}|\mathbf{h}>}}{\mathcal{F}_{++}^2}\right)^{1/4} \\ = & \left(4\frac{\mathcal{F}_{++}+\mathcal{F}_{\times\times}}{\mathcal{F}_{++}^2}\right)^{1/4}\sqrt{\frac{r}{r_0}}.\end{aligned} \tag{2.37}$$

The deviation Δx is thus changed from being proportional to r/r_0 away from $v = 1$ to a weaker dependence ($\propto (r/r_0)^{1/2}$) near $v = 1$.

As we shall see in the next section, our cosmological application of coalescence signals will be based on a statistical treatment of a relatively large number of events. To facilitate our estimates we will assume that errors in distance ($\Delta x = \Delta r/r_{(0)}$) are actually always proportional to r_0/r

$$\Delta x = \varepsilon(\theta,\phi,\psi,\iota)\frac{r}{r_0}, \tag{2.38}$$

where, to account for the modification near $v = 0$, we limit ε from above

$$\varepsilon(\theta,\phi,\psi,\iota) \leq \bar{\varepsilon}(\theta,\phi,\psi). \tag{2.39}$$

The limit $\bar{\varepsilon}$ is defined as

$$\bar{\varepsilon} \equiv \left(4\frac{\mathcal{F}_{++}(\theta,\phi,\psi)+\mathcal{F}_{\times\times}(\theta,\phi,\psi)}{\mathcal{F}_{++}^2(\theta,\phi,\psi)}\right)^{1/4}\sqrt{<\frac{r_0}{r}>}, \tag{2.40}$$

where $< r_0/r > \approx 20$ (for $\rho_{\text{min}} = \chi_{\text{min}} r_0/r \geq 5$, see Fig. 2.4(a), is the typical average value of r_0/r for all events detected by all three detectors. More specifically, given values of θ, ϕ and ψ, $\varepsilon(\theta,\phi,\psi,\iota)$ is computed according to Eqs. (2.31) and (2.32) if v is far enough from 1 so that ε does not exceed the limit (2.39). Otherwise, the limit (2.39) is taken as actual ε.

Starting from this basis, we obtain by a Monte-Carlo method five functions $\varepsilon_k(\chi)$ computed in the following way: We take all events with $\chi_{\text{min}} \geq \chi$ (see Eq. (2.23)), then arrange them according to increasing ε. Finally, we define $\varepsilon_k(\chi)$ to be the average ε of those events in the k'th fifth of this array. By this modeling procedure we take into account the range of errors corresponding to different angles θ, ϕ, ψ and ι, while keeping the amount of computation, necessary to obtain the results discussed in the following sections, within relatively modest bounds. The functions $\varepsilon_k(\chi)$ are shown in Fig. 2.4(b). Their relevance will become completely clear in the next section.

3.3 Chirp and neutron star mass estimation

Due to the change in wave frequency Eq. (2.15), the parameter which can be measured with highest accuracy is the chirp mass [8] — to about 0.1% at $\rho \approx 10$. On the other hand, if one wants to obtain individual masses, one will have to use post-Newtonian corrections of the form [8, 9]

$$\dot{f}(t) = \dot{f}_{\text{Newt}}\left[1 - \left(\frac{743}{336} + \frac{11}{4}\frac{\mu}{M}\right)(\pi M f)^{2/3} + \left(4\pi - \frac{113}{12}\zeta_{\perp} - \frac{25}{4}\xi_{\perp}\right)(\pi M f) + \cdots\right], \tag{2.41}$$

where $\zeta_{\perp}$ and $\xi_{\perp}$ are projections orthogonal to the binary orbital plane of the vectors, $\vec{\zeta} = \vec{S}_1 + \vec{S}_2$ and $\vec{\xi} = (M_2/M_1)\vec{S}_1 + (M_1/M_2)\vec{S}_2$ ($\vec{S}_1$ and $\vec{S}_2$ are components' spins, μ and M are the reduced and the total mass of the binary). $\dot{f}_{\text{Newt}}$ is the lowest order Newtonian expression corresponding to Eq. (2.15). Relatively similar frequency dependence of the two correction terms in the above equation will make it difficult to disentangle the effects of spins from the dependence on the individual masses. It is estimated [8] that this will cause the fractional error in μ to be as high as about 10% in the case of an NS-NS binary and about 15% for a BH-NS binary at signal to noise ratio $\rho = 13$. Since the error is, naturally, inversely proportional to ρ, we will thus assume for a BH-NS binary

$$\frac{\Delta M_n}{M_n} = \frac{1.9}{\rho}, \tag{2.42}$$

where ΔM_n is the average error in the estimation of the member neutron star's mass, and $(\rho)^2 = (\rho_1)^2 + (\rho_2)^2 + (\rho_3)^2$ is the total signal to noise ratio in the three detectors. In practical computations, we will use

$$\rho(r) = \frac{r_0}{r} < (\chi_1)^2 + (\chi_2)^2 + (\chi_3)^2 >^{1/2}, \tag{2.43}$$

where we average over all angles that give $\chi_{\min} \geq \bar{\chi} \equiv 5r/r_0$.

It is important to note that the above expressions for errors strictly apply only in the limit of small errors [12]. In this limit the estimated parameters will be distributed around the true ones according to a Gaussian with the variances indicated in Eqs. (2.38) and (2.42). For a smaller signal to noise ratio, and correspondingly large errors, the distribution of inferred parameters is not necessarily Gaussian. Nevertheless, the errors quoted give us an estimate of the spread of the inferred parameters described by a distribution function whose details, though yet unknown, can be fully worked out in the future.

3.4 Gravitational Waves and Cosmological Redshift

We can easily generalize the above treatment to the source at cosmological distances. In this case h_c, Eq. (2.14), is modified to

$$\begin{aligned} h_c &= \frac{M_c}{r_c}(\pi M_c f)^{2/3} \exp\left(i2\pi \int^t f dt\right) \\ &= \frac{M_c'}{(1+z)r_c}(\pi M_c' f')^{2/3} \exp\left(i2\pi \int^{t'} f' dt'\right), \end{aligned} \tag{2.44}$$

where r_c, the so-called "corrected luminosity" or "proper motion" distance, was defined in Sec. 2. (See Eq. (2.12)). Also, $M_c' = (1+z)M_c$, $dt' = (1+z)dt$ and $f' = f/(1+z)$, where t', f' are quantities measured by the observer and f, t are the quantities at the source. From the above definitions and Eq. (2.15), it follows

$$f' = \frac{f}{1+z} = \frac{1}{\pi M_c'}\left(\frac{5}{256}\frac{M_c'}{t_0' - t'}\right)^{3/8}. \tag{2.45}$$

One immediately sees that any quantity with the dimensions $(\text{length})^p$ (in geometric units) will be scaled by the factor $(1+z)^p$. This will hold for any order of post-Newtonian corrections to the waveform Eqs. (2.13) – (2.15). From Eq. (2.44) one can then conclude that the signal to noise ratio ρ_k in each detector, being proportional to $M_c'^{5/6}/D$ (D is the luminosity distance of the source — see Sec. 2.), behaves as

$$\rho_k = \chi_k \frac{r_0}{r_c}\frac{1}{(1+z)^{1/6}} = \chi_k \frac{r_0}{D}(1+z)^{5/6}. \tag{2.46}$$

By a straightforward generalization of Eqs. (2.38) and (2.42), the binary parameter estimation errors are

$$\begin{aligned} \frac{\Delta M_{\rm n}'}{M_{\rm n}'} &= \frac{1.9}{\rho}, \\ \frac{\Delta D}{D} &= \varepsilon \frac{D}{r_0}\frac{1}{(1+z)^{5/6}}. \end{aligned} \tag{2.47}$$

As we see, the luminosity distance of the source is measured directly while the redshift, z, is disguised in the measurable combination of parameters $M' = (1+z)M$. However, if one of the members of the binary is a neutron star, one still might be able to estimate the redshift due to the observation that neutron star masses fall within a certain range. The data currently available from X-ray and binary pulsars [13] are consistent with the average neutron star mass of $\bar{M}_n = 1.4 M_\odot$ and the standard deviation of about $\Delta M_n = 0.3 M_\odot$, corresponding to the relative error of

$$\delta M_n / \bar{M}_n \approx 0.2. \tag{2.48}$$

One should note that the far more reliable data from binary pulsars indicate a narrower range of

$$\delta M_n / \bar{M}_n \approx 0.05. \tag{2.49}$$

However, the number of observed objects is still rather small so in the following we will consider both these ranges in turn.

The existence of binaries consisting of two neutron stars offers an opportunity for even more accurate determination of source's redshift. As we mentioned earlier, the (redshifted) chirp mass, $M_c' \equiv M_c(1+z)$, will be determined with high accuracy which, contrary to individual masses, does not suffer from spin effects. Since the spread of chirp masses for NS-NS binaries is comparable to that of neutron masses themselves, this will, obviously, enable the observer to pinpoint the redshift with far more certainty than in the case of BH-NS binaries.

4 Determination of cosmological parameters from gravitational wave measurements

As we noted in Sec. 3, the errors quoted in Eqs. (2.47) are estimated in the limit of large signal to noise ratios and, correspondingly, small errors. As we receive signals from larger distances, the mean errors will, naturally, increase. The larger errors will not have a strictly Gaussian distribution, which is obvious at least from the fact that measured distances and masses cannot be negative. However, the known statistical properties of the noise should make it possible to find the actual distribution of errors, away from the Gaussian regime. Thus, one would be able to use in the statistical analysis not only the relatively few events with large signal to noise ratios, but also those more numerous, coming from very large distances as well.

We will first discuss the utility of NS-NS binaries for estimation of the cosmological parameters. While on one hand the gravitational waves from coalescing NS-NS binaries are weaker than those from BH-NS binaries, hence allowing detection of events at relatively smaller distances, they can provide redshifts with far greater accuracy. The latter point will be strengthened even further if it turns out that the chirp masses of binary neutron stars fall within the narrower of the two ranges mentioned at the end of the last section. One can reasonably hope that this uncertainty will ultimately be resolved on the basis of continued observations of binary pulsars and/or detection of gravitational waves from relatively nearby (say $z \lesssim 0.1$) binaries.

From the distribution of errors induced by noise in the detectors (once the distribution is known), one can compute the distribution $\mathcal{P}(z, D|z_s, D_s, M_c, \omega)dzdD$ which gives the probability that a source of redshift z_s, distance D_s, having chirp mass M_c and relevant angles $(\theta, \phi, \psi, \iota)$ denoted here together by ω (see Sec. 3) will be detected in the element $dzdD$ of the redshift-luminosity distance plane. Then, given the distribution of binary neutron star chirp masses $p_c(M_c)$ ($\int p_c dM_c = 1$), discussed above, along with conveniently chosen bounds $M_c^{\rm u}$ and $M_c^{\rm d}$, one can find the probability density

$$\mathcal{P}(z, D|z_s, D_s(z_s)) = \int_{M_c^{\rm d}}^{M_c^{\rm u}} p_c(M_c)dM_c \int d\omega \mathcal{P}(z, D|z_s, D_s(z_s), M_c, \omega), \tag{2.50}$$

of observing at z and D a source which is actually positioned at z_s and D_s. Here $D_s(z_s)$ is the cosmological distance-redshift relation we seek to determine. If we know the rate $n_0(z_s)dz_s$ (measured in year^{-1}) of binary mergers in the redshift interval dz_s, we can compute the total number of events $N_{\mathbf{c}}(z, D)$ observed in a patch $dzdD$ of unit area

$$N_{\mathbf{c}}(z, D) = \int_0^{z_{\rm max}} \mathcal{P}(z, D|z_s, D_s(z_s))n_0(z_s)dz_s, \tag{2.51}$$

where $\mathbf{c}$ denotes the three cosmological parameters which determine the distance - redshift relation of the source ($c_1 = h_0$, $c_2 = \Omega_0$, $c_3 = \lambda_0$). In the above expression we have assumed that the NS-NS binaries do not exist beyond some redshift $z_{\rm max}$. Another assumption is that the chirp mass function p_c does not change with time (redshift).

Expression (2.51) implicitly contains the requirement that the signal to noise ratios ρ_k, Eq. (2.46), of events which are accepted as true binary mergers (as opposed to mere glitches in the noisy detectors) should exceed some minimum threshold $\rho_{\rm t}$ in all three detectors. In this article we have adopted $\rho_{\rm t} = 5$. In reality ρ is a random variable, dependent on the actual realization of the noise as well as on the "real" parameters of the binary. Therefore, an exact treatment would include a probability distribution for ρ given the real binary parameters $(M_c, D_s, \iota, \cdots)$. This distribution can be provided in the future by the same token as the error distributions mentioned above. However, in order to simplify our treatment, we will work only with the noise averaged values of signal to noise ratio $\rho(M_c, D, \theta, \phi, \psi, v \equiv \cos\iota)$, actually given by Eq. (2.46), and assume that only events with

$$\chi_{\min} \geq \bar{\chi}(z_s, D_s) \equiv 5\frac{D_s}{r_0(1+z)^{5/6}} \tag{2.52}$$

are detected. Thus only the fraction $P(>\bar{\chi}(D_s))$(see Fig. 2.4) of all sources at given $D_s(z_s)$ will be detected. Of course, if $\bar{\chi} > 0.74$ (the maximum value of $\chi_{\min}$ for the configuration of detectors we have assumed in this article) no coalescences will be observed at the given distance and redshift. We emphasize that this simplifying limit is imposed "at the source" so that only the binaries whose *real* parameters satisfy the above requirement are considered to be actually detected.

From the point of view of the observer, the signal to noise ratio is computed on the basis of inferred parameters M_c', D. Then the observer accepts or rejects the signal as a true binary merger based on whether the signal to noise ratio so computed is larger or smaller than ρ_t. Hence, consistent with the limit at the source, given some reasonable maximum chirp mass M_c^u, the observable region is limited from above by

$$D < D_{\max}(z, M_c^u) = 0.74 r_0(M_c^u)\frac{(1+z)^{5/6}}{\rho_t}. \tag{2.53}$$

Note that the distribution of observed signal to noise ratio for a given source would follow directly from the realistic noise-induced distribution of inferred parameters of a binary. However, since we will be working with model distribution functions in the following, we shall impose the signal to noise limit "at the source" separately.

Following the above assumptions, one can write down the probability distribution,

$$P_c(z, D) = \frac{N_c(z, D)}{\int_S N_c dz dD}, \tag{2.54}$$

of events in region S accessible to our detectors [defined by Eq. (2.53)]. This probability function, computed theoretically on the basis of statistical properties of the noise and the distribution of neutron star masses, can serve as foundation for an estimation of the cosmological parameters. Specifically, given a set of n observed events (z_i, D_i), the cosmological parameters can be estimated by the method of maximum likelihood (see Appendix B) which consists of searching for those values of c such that the likelihood function,

$$\mathcal{L}(\{z, D\}, \mathrm{c}) = P_c(z_1, D_1) P_c(z_2, D_2) \cdots P_c(z_n, D_n), \tag{2.55}$$

is maximized. Since the number of events observed will be fairly large (see below), the error of such an estimation will approach the so-called Frechet - Cramer - Rao limit in which the bias of estimation (see Appendix B) is zero and the average errors Δc_μ are

$$\Delta c_\mu \equiv \sqrt{< (c_\mu - c_\mu^o)^2 >} = \sqrt{\Sigma^{(n)}_{\mu\mu}}, \tag{2.56}$$

where c_μ^o are the correct cosmological parameters and $\Sigma^{(n)}_{\mu\nu}$ is the inverse of matrix $I^{(n)}_{\mu\nu}$, defined as

$$I^{(n)}_{\mu\nu} \equiv n \int_S (\ln P_c(z,D))_{,\mu} (\ln P_c(z,D))_{,\nu} P_c(z,D) dz dD \tag{2.57}$$

[See also Eqs. (2.93) and (2.94) in Appendix B].

As hinted above, in order to estimate the accuracy of the determination of the cosmological parameters in absence of the "real" distribution, we will assume that the measured quantities z and D are related to the real values z_s, $D_s(z_s)$ by

$$\begin{aligned} z &= z_s \left(1 + \frac{\Delta z_s}{z_s}\right)^{x_1}, \\ D &= D_s \left(1 + \frac{\Delta D_s}{D_s}\right)^{x_2}, \end{aligned} \tag{2.58}$$

where x_1 and x_2 are random Gaussian numbers with standard deviation 1. ΔD_s is, in our model, computed according to Eq. (2.47) with ε taken with equal probabilities from the set of five functions $\varepsilon_j(\bar{\chi})$. We can, then, express the probability of observing an event in the range $dzdD$, centered on z and D if the real position of the source is z_s, D_s, as

$$\mathcal{P}(z, D|z_s, D_s) = \sum_{j=1}^{5} \mathcal{P}_j(z, D|z_s, D_s), \tag{2.59}$$

where

$$\begin{aligned} \mathcal{P}_j(z, D|z_s, D_s) = \;& C_j \;\; \exp\left[-\frac{1}{2}\left(\frac{\ln(z/z_s)}{\ln(1+\Delta z_s/z_s)}\right)^2\right] / z \\ & \times \;\; \exp\left[-\frac{1}{2}\left(\frac{\ln(D/D_s)}{\ln(1+\Delta D_{s_j}/D_s)}\right)^2\right] / D, \end{aligned} \tag{2.60}$$

where C_j are normalization constants chosen so that $\int_S \mathcal{P}_j(z, D|z_s, D_s) dz dD = 1$. For fixed j, $\ln(z/z_s)$ and $\ln(D/D_s)$ are distributed according to Gaussian distributions with standard deviations $\ln(1 + \Delta z_s/z_s)$ and $\ln(1 + \Delta D_{s_j}/D_s)$, respectively. In the limit of large signal to noise ratio and small errors, we can write

$\log(z/z_s) \approx (z - z_s)/z_s$ (similarly for D), and the above model distributions approach the familiar Gaussian expressions

$$\mathcal{P}_j(z, D|z_s, D_s) \approx \frac{1}{2\pi \Delta z_s \Delta D_s} \exp\left[-\frac{1}{2}\left(\frac{z - z_s}{\Delta z_s}\right)^2 - \frac{1}{2}\left(\frac{D - D_s}{\Delta D_{s_j}}\right)^2\right]. \tag{2.61}$$

The model distribution (2.60) that we have adopted as a substitute for the more realistic distribution (2.50) is a version of the so-called "log - normal" distribution [14]. Accommodating the positive definiteness of both redshift and distance, the distribution (2.60) is asymmetrical for large errors, giving typically larger upward than downward "shifts" in z and D.

The error Δz_s, appearing in Eqs. (2.60) and (2.61), is primarily due to the fact that the observer is computing the redshift z as

$$z = \frac{M'_c}{\bar{M}_c} - 1, \tag{2.62}$$

where $\bar{M}_c$ is the *a priori* average of the proper, i.e., not redshifted, binary neutron star chirp masses. Since $M'_c \equiv M_c(1 + z)$ will be measured very accurately, we can write

$$\Delta z_s = (1 + z_s)\frac{\delta M_c}{\bar{M}_c}. \tag{2.63}$$

This deviation, stemming entirely from the spread δM_c of proper binary chirp masses, Eqs. (2.48) or (2.49), simulates in effect the distribution function $p_c(M_c)$ and will, for our purposes, substitute for it, thus eliminating the need to integrate over M_c as it would be done in Eq. (2.50).

All the approximations and assumptions, discussed so far in this section, concern the reasonably predictable statistical properties of detector noise and the neutron star mass distribution. Those approximations should not influence significantly our estimation of accuracy with which we will be able to measure the cosmological parameters. However, in order to obtain the c-dependent distribution (2.51) we also need to know the rate $n_0(z_s)dz_s$, defined as the number of mergers in the redshift interval dz_s that occur during one year of time measured by clocks on earth. Assuming that the coalescence rate in the comoving volume is constant throughout the universe, we obtain

$$n_0(z_s) = \bar{N}_0 \frac{4\pi r_c^2}{(1 + z)\sqrt{1 - kH_0^2 r_c^2}} \frac{dr_c}{dz_s}, \tag{2.64}$$

where $r_c(z)$ was defined in Eq. (2.12), and

$$\begin{aligned} \bar{N}_0 &= 125\frac{3}{4\pi}N_{200}\left(\frac{h}{0.75}\right)^3 \mathrm{Gpc}^{-3}\mathrm{year}^{-1} \\ &= 90\left(\frac{N_{200}}{3}\right)\left(\frac{h}{0.75}\right)^3 \mathrm{Gpc}^{-3}\mathrm{year}^{-1} \end{aligned} \tag{2.65}$$

is the proper number, counted in the local rest frame, of events per cubic gigaparsec in one year. We will assume that $N_{200} = 3$ consistent with the estimates of Phinney and of Narayan et al. [3].

The premise of constant proper rate, which is roughly equivalent to a constant average rate in a typical galaxy or cluster of galaxies, might potentially be the most unreliable of those adopted in this section. Indeed, due to complex evolutionary processes in galaxies, this rate might change even at moderately low redshifts. Even so, given many observed events, one could be able to "invert" the statistical map $\{z_s, D_s\} \mapsto \{z, D\}$ described by the calculable distribution (2.50), and, by using the powerful machinery of statistical analysis and hypothesis testing, obtain not only the cosmological parameters, but also the rate $n_0(z_s)$ as a bonus. Of course, the increased uncertainty might reduce somewhat the accuracy with which the cosmological parameters are estimated [15].

Finally, from Eqs. (2.59), (2.60) [using Eqs. (2.63) and (2.47)] and (2.64) we obtain a model distribution

$$P_{\mathbf{c}}(z, D) = C' \int_0^{z_{\max}} \mathcal{P}(z, D|z_s, D_s(z_s)) n_0(z_s) P[> \bar{\chi}(D_s(z_s))] dz_s, \tag{2.66}$$

where C' is a normalization constant ($\int_S P_{\mathbf{c}} dz dD = 1$). The factor $P(> \bar{\chi})$ is the fraction of events at given z_s actually detected, as discussed in connection with Eq. (2.52). It is included explicitly because of the normalization of $\mathcal{P}$, Eq. (2.60). This simply means that the total number of events observed in one year is $\int_0^{z_{\max}} n_0 P(> \bar{\chi}) dz_s$ (see Fig 2.5). Once again $P_{\mathbf{c}}$ depends on the cosmological parameters $\mathbf{c}$ through the distance-redshift relation $D_s(z_s)$. We will sometimes emphasize this fact by using the notation $P(z, D|\mathbf{c})$ for $P_{\mathbf{c}}(z, D)$.

The distribution function (2.66) can now be used in Eqs. (2.56) and (2.57) to estimate the average errors one will make in using binary coalescence measurements to infer the cosmological parameters.

The results of numerical computation of errors (2.56), based on the model distribution (2.66), are shown in Fig. 2.1 for different values of r_0. It was assumed that $z_{\max} = 3$, $N_{200} = 3$ and that the data were collected for one year. The

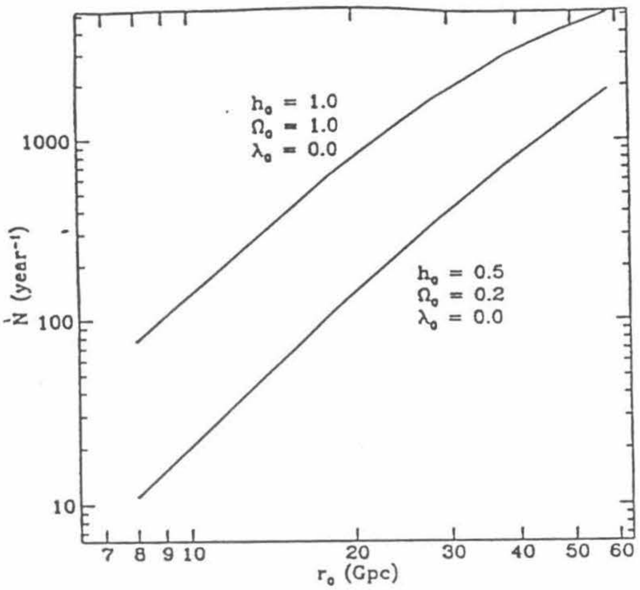

Figure 2.5: Average numbers of events with $\rho_{\rm min} > 5$ detected in one year as functions of r_0, for two sets of cosmological parameters.

errors of cosmological parameter estimation are presented for the two values of $\delta M_c/\bar{M}_c$, 0.20 and 0.05, and for two sets of cosmological parameters, ($h_0 = 1.0$, $\Omega_0 = 1.0$, $\Lambda_0 = 0$) and ($h_0 = 0.5$, $\Omega_0 = 0.2$, $\Lambda_0 = 0$, which we call "compact" and "spacious" universe respectively). These results have already been discussed in the Introduction.

We turn attention now from NS-NS binaries to BH-NS binaries. As we pointed out above, the main advantage of BH-NS binaries for cosmological measurements comes from the relatively greater strength of a typical signal at a given distance compared to the case of NS-NS binaries. This obviously translates to a greater distance accessible to BH-NS merger detection by a set of earth based detectors (see Eq. (2.24)). However, apart from greater uncertainties regarding the rates of BH-NS mergers, the main disadvantage stems from the broader range of black hole masses and, equivalently, very little *a priori* knowledge about typical chirp masses. In addition, we can use only the rather inaccurately measured (see Eq. (2.47)) redshifted neutron star mass $M_n' = (1+z)M_n$ to infer the binary's redshift. Combined with the independent uncertainty of proper neutron star masses δM_n, the resulting error in redshift determination can be estimated roughly as

$$\Delta z_s = (1+z)\left[\left(\frac{1.4}{\rho(\bar{\chi})}\right)^2 + \left(\frac{\delta M_n}{\bar{M}_n}\right)^2\right]^{1/2} \tag{2.67}$$

(see Eq. (2.47)), which can, in principle, be quite larger than the error (2.63) in redshift for NS-NS binaries.

Though equipped with a fairly accurately determined redshifted chirp mass M_c', we have to contend with a wide range of both proper $M_h \approx M_c^{5/2} M_n^{-3/2}$ and redshifted $M_h' \approx M_c'^{5/2} M_n'^{-3/2}$ black hole masses. Therefore, in order to construct an *a priori* distribution $P_{\mathbf{c}}(z,D) \equiv P(z,D|\mathbf{c})$, similar to the one associated with NS-NS binaries, one would need to know the black hole mass function $p_h(M_h)$ ($\int p_h dM_h = 1$). Given such (presumably redshift independent) $p_h(M_h)$, one would compute

$$P(z,D|\mathbf{c}) = \int_{M_h^d}^{M_h^u} P_{M_h}(z,D|\mathbf{c}) p_h(M_h) dM_h, \tag{2.68}$$

where P_{M_h} is a distribution computed following the same sequence of steps outlined above for the NS-NS case with an additional assumption of a fixed black hole mass M_h. In Eq. (2.68) we have assumed that the distribution of neutron star masses is independent of the companion black hole mass, so that we could write the joint mass function of the BH-NS binaries as $p(M_h, M_n) = p_h(M_h)p_n(M_n)$, where p_n would be the neutron star mass function used earlier in this section.

However skeptical one might be regarding the prospects of knowing the neutron star mass function in advance of the cosmological applications proposed in this article, the mass function of black holes will, in all likelihood, remain only a matter of speculation until a large number of BH-NS or BH-BH binary mergers are observed. In fact one might be more ambitious than we have been so far and try to obtain $p_h(M_h)$, in addition to $\mathbf{c}$, by matching the measured parameters z, D, M_n', M_h' (or M_c'), and a "grand" distribution $\mathrm{P}(z, D, M_n', M_h'|\mathbf{c}, p_h)$, assuming again a known neutron star mass function p_n.

Since in this article we focus on the determination of cosmological parameters, it is important to see how sensitive our method really is to the actual black hole mass function. In other words: Through r_0 (see Eq. (2.24)) the distribution P_{M_h} depends on the mass M_h black holes are assumed to have. Different black hole masses will produce different spreads of observed events (z, D) around the real cosmological curve $D_s(z_s)$. To evaluate the importance of p_h we will consider the following question: Given a universe with BH-NS binaries containing black holes of a single mass $M_h^{(0)}$, how large a systematic error (or bias - see Appendix B) is introduced if we try to fit a distribution function $P_{M_h}(z, D|\mathbf{c})$, with the "wrong" M_h to data which are actually distributed according to $P_{M_h^{(0)}}(z, D|\mathbf{c})$. More specifically, we are interested in finding

$$b_\mu^{(M_h)} \equiv < \hat{c}_\mu > - c_\mu^o, \tag{2.69}$$

where $< \hat{c}_\mu >$ would be the average over an ensemble of "gravity wave detection projects" of the best fit parameters $\hat{c}_\mu$ obtained by the method of maximum likelihood (see Appendix B) using the wrong function P_{M_h}. As explained in the Appendix B, $b_\mu^{(M_h)}$ can be estimated by maximizing

$$\Psi^{(M)}(\mathbf{c}|\mathbf{c}^0) = \int_S P_{M_h^{(0)}}(z, D|\mathbf{c}_0) \ln P_{M_h}(z, D|\mathbf{c}) dz dD \tag{2.70}$$

with respect to $\mathbf{c}$.

In order to compute model distribution functions $P_{M_h^{(0)}}$ and P_{M_h}, that appear in Eq. (2.70), we use Eq. (2.66), where the distribution $\mathcal{P}(z, D|z_s, D_s)$, Eq. (2.60), is computed by taking ΔD_s from Eq. (2.47) and Δz_s from Eq. (2.67). In all these formulas $r_0(M_c)$ is given by Eq. (2.24) where $M_c = (M_h M_n)^{3/5}/(M_h + M_n)^{1/5}$ increases with M_h.

Assuming $\delta M_n/M_n = 0.05$ and using $M_h = 10 M_\odot$, we have computed this bias for different values of $M_h^{(0)}$. The results for $h_0 = 1$, $\Omega_0 = 1$, $\lambda_0 = 0$ and $r_0 = 28$Gpc are shown in Fig. 2.6.

We can see that while h_0 and Ω_0 are very weakly affected by our ignorance of the real black hole mass, the ensuing bias in λ_0 can be significant.

To put these results into perspective, we compute the average random (as opposed to systematic) errors that would be obtained if, somehow, we knew exactly the black hole mass, $M_h = M_h^{(0)}$. These errors are obtained in the same way as in the case of NS-NS binaries, using now $P_{M_h}(z, D|\mathbf{c})$ (instead of $P_\mathbf{c}(z, D) \equiv P(z, D|\mathbf{c})$), with $M_h = 10 M_\odot$ in Eq. (2.57), and are shown in Fig. 2.2 for the indicated values of cosmological parameters and neutron star mass range. We have discussed these results in the introduction and given analytic power-law fits in the abstract where the noise level was expressed in units of the predicted "advanced" LIGO noise level, $N \equiv \sqrt{S_m}/1.7\ 10^{-24}\mathrm{Hz}^{-1/2}$.

A comparison of Figs. 2.6 and 2.2 suggests that as far as h_0 and Ω_0 are concerned, our ignorance of the black hole mass function does not really matter. In other words, even if we have only a very limited knowledge of typical black hole

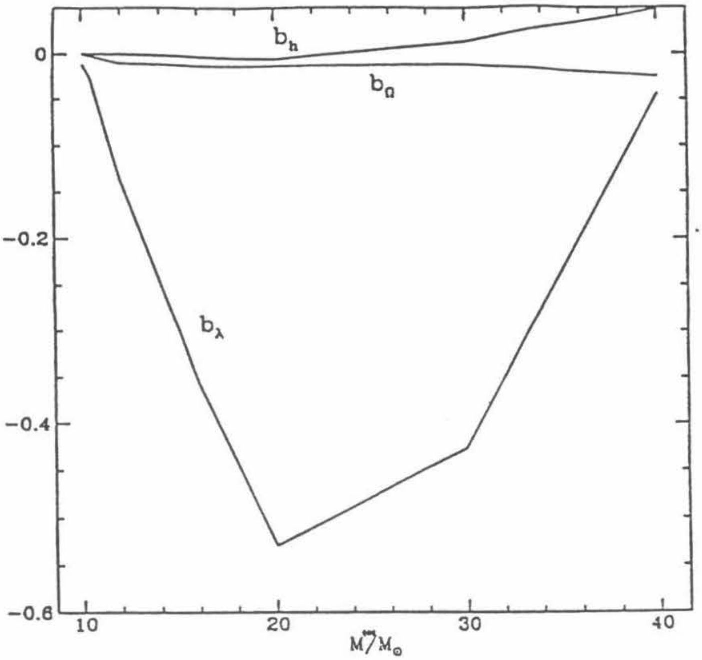

Figure 2.6: Systematic errors b_{c_μ} due to the uncertainty of the typical mass of black holes in BH-NS binaries as functions of $M_h^{(0)}$ assuming $M_h = 10M_\odot$ is used in the statistical inference.

masses in the universe, we can determine those two parameters with a high accuracy. On the other hand, a determination of λ_0 with accuracy approaching that "promised" in Fig. 2.2 (e.g., $\Delta\lambda \approx 0.2$, for $r_0 = 28$Gpc and a "compact' universe) would require some familiarity with the "fine" structure (on scales of about $3M_\odot$) of the black hole mass function entering Eq. (2.68).

5 The effects of gravitational lensing

5.1 General considerations

In the preceding section we have assumed that the gravitational waves emitted by distant, compact binaries propagate to the earth through a homogeneous Friedmann universe, neglecting possible effects of local inhomogeneities in the form of individual stars, galaxies, clusters of galaxies, superclusters, etc., which abound in the real universe. As we mentioned earlier, these inhomogeneities can affect the propagation of gravitational waves only through their local gravitational fields or, in different words, through the local curvature of spacetime they generate. As for electromagnetic radiation, the effect of those intervening inhomogeneities consists of amplification of the gravitational waves and, sometimes, analogously to multiple imaging of quasars, the appearance of more than one signal from a single astrophysical event. On the other hand, if there are no intervening clumps of matter in the vicinity of the wave's path (so called "empty cone"), the gravitational wave, received on earth, will be weaker than the wave that would propagate from the same coalescence through a smoothly filled ("full cone") Friedmann universe [16]. The latter phenomenon is, somewhat awkwardly, referred to as "deamplification." In this section we will treat this gravitational deflection (lensing) within the framework of geometric optics, neglecting the effects of the finite wavelength of gravitational radiation. This is a very good approximation in all realistic situation.

Since deflection does not change the phase properties of the wave, the amplification results only in a change of the apparent distance of the source as measured by the observer on earth. This implies that even if we had perfectly accurate and noise-free detectors ("perfect observer") we would still observe dispersion of measured distances away from the ideal Friedman curve $D_F(z_s)$. At least in principle, this phenomenon can be described by a probability distribution $\mathcal{P}_L^{(0)}(D|D_F(z_s))$ ($\int P_L^{(0)} dD = 1$), where $D_F(z_s)$ is the distance corresponding to a (hypothetical) propagation of the signal through a completely homogeneous Friedmann universe and D is the distance as observed by the imagined perfect observer. In reality the noise in the detectors compounds this uncertainty so that the probability density that the signal originating at z_s will be interpreted as coming from redshift z and distance D is

$$\mathcal{P}_L(z, D|z_s, D_F(z_s)) = \int_0^\infty \mathcal{P}(z, D|z_s, D')\mathcal{P}_L^{(0)}(D'|D_F(z_s))dD', \qquad (2.71)$$

where $\mathcal{P}(z, D|z_s, D')$ is the distribution discussed in the previous section (see Eq. (2.50) or the model distribution (2.60)). In order to pursue our main task of finding the cosmological parameters $\mathbf{c}$ we might, again in principle, follow the method described in the previous section: (i) integrate the distribution $\mathcal{P}_L$ over the source redshifts exactly as it was done in Eqs. (2.51) - (2.54) for NS-NS binaries or similarly for BH-NS binaries, (ii) thereby obtain the distribution $P_L(z, D|\mathbf{c})$, and (iii) finally adjust $\mathbf{c}$ to find the maximum likelihood for a set of observed redshifts and distances. One necessary ingredient, the knowledge of the "primary" lensing statistics $\mathcal{P}_L^{(0)}$ might, however, remain elusive. By analogy with the problem of uncertain black hole mass we faced in the last section, we can inquire about the real price we pay for our ignorance about the distribution $\mathcal{P}_L^{(0)}$. In the most extreme case we would like to know just how much additional error is introduced in the determination of c if we ignore the effect of local inhomogeneities in the universe and stubbornly use the lensing-free distribution $P(z, D|\mathrm{c})$, discussed in the last section, in fitting to the observed redshifts and distances. Of primary interest, then, is an estimate of the systematic shift (bias) of the parameters $\hat{\mathrm{c}}$, inferred in this way, from the real ones c^0.

Similarly to the case of uncertain black hole masses in BH-NS binaries (see also Appendix B), this bias can be estimated by maximizing

$$\Psi_L \equiv \int_S P_L(z, D|\mathrm{c}^0) \ln P(z, D|\mathrm{c}) dz dD \tag{2.72}$$

with respect to c. Of course, in computing this expression, instead of the unknown real $\mathcal{P}_L^{(0)}$, we must use a model function which, hopefully, captures the main features of the propagation of light in an inhomogeneous universe.

That one should, in general, expect non-zero bias is due to a typical asymmetry between amplification and deamplification, which is reflected in the asymmetry of the distribution $\mathcal{P}_L^{(0)}(D|D_s(z_s))$ around D_F. More specifically, usually many sources are weakly demagnified (effectively "shifted" farther away) and relatively few are strongly magnified. This can be seen at least from the fact that, on one hand, the total flux from all sources at given z_s is conserved, and, on the other, although a point source can, naively speaking, be magnified by an arbitrary amount, there is a limit to demagnification corresponding to the so-called Dyer-Roeder empty cone distance [17] (see below). This Dyer-Roeder distance arises in the extreme and idealized case of a ray remote enough from any clumps of matter to be totally unaffected by any shear.

This asymmetry between amplification and deamplification is only augmented by splitting of a wave (binary merger in our case) into several "image" signals, some of which are too weak to be observed. It should be intuitively clear that in any "egalitarian" statistical method the preponderance of weakened sources will shift the measured values of the cosmological parameters c towards those of a more spacious universe (e.g., smaller Ω_0), assuming we are not able to deconvolve the effects of lensing due to our ignorance of $\mathcal{P}_L^{(0)}$.

5.2 Quantitative estimates

In order to estimate quantitatively the effects of the propagation of waves through the inhomogeneous universe, we will assume that a certain fraction $1 - \zeta$ of the total mass of the universe is in the form of Schwarzschild lenses, while the rest, ζ, is smoothly distributed. Strictly speaking, Schwarzschild lenses correspond only to the more compact astrophysical objects like stars and black holes. However, since we are primarily interested in the possibility of systematic effects of lensing on the determination of cosmological parameters, we shall use Schwarzschild lenses to represent lensing in general including that due to galaxies. Since the propagation of the gravitational wave amplitude in a curved background space obeys the same laws that govern the propagation of electromagnetic waves [18], we can simply use the results known for the lensing of electromagnetic radiation [16]. For simplicity we will also assume throughout this section that the real cosmological parameters are $\Omega_0 = 1, \lambda_0 = 0$.

Due to the long-range nature of the gravitational interaction, many Schwarzschild lenses will affect the propagation of the wave. Therefore, the "distortion" matrix describing the deformation of a ray bundle,

$$\mathcal{B} \equiv \frac{\partial \vec{\theta}_s}{\partial \vec{\theta}_i}, \tag{2.73}$$

where $\vec{\theta}_i$ and $\vec{\theta}_s$ are the angular positions of the image and source respectively [16], will, in general, be a nonlinear function of shears from many individual deflectors. However, it seems likely that rays weakly influenced by shear will give the dominant contribution to the systematic errors in cosmological parameters **c**. Therefore, as proposed by Schneider and Weiss [19], we shall keep only the terms linear in shear, and, after taking a continuous limit, obtain

$$\mathcal{B}_s = b_s \mathbf{1} - \begin{pmatrix} \sigma_1 & \sigma_2 \\ \sigma_2 & -\sigma_1 \end{pmatrix}. \tag{2.74}$$

In this formula the first (demagnifying) term is due to the fact that we have actually removed a fraction $1-\zeta$ from the smooth component of the mass and converted it into a population of Schwarzschild lenses whose total shear is modeled by the second term. Then if we randomly choose a ray we can, still following Schneider and Weiss, derive the probability distribution $P_\sigma(\sigma_1, \sigma_2) d\sigma_1 d\sigma_2$ for the components of the total shear

$$P_\sigma(\sigma_1, \sigma_2) = \frac{1}{2\pi} \frac{Y_s}{(Y_s^2 + \sigma_1^2 + \sigma_2^2)^{3/2}}, \tag{2.75}$$

associated with the ray. In the above equations b_s is the ratio of the Dyer-Roeder distance to the Friedmann distance, while $Y_s \equiv Y(z_s)$ is the solution of the integral equation

$$Y(z) = b(z) - 1 + \int_0^z dx \kappa'(x)\beta(x,z)Y(x), \tag{2.76}$$

where $\kappa'(z) = (3/2)(1-\zeta)D_A(z)H_0\sqrt{1+z}$. D_A is the angular diameter distance defined in Sec. 2; $\beta(x,z) \equiv D_A(x,z)/D_A(z)$, where $D_A(x,z)$ is the angular diameter distance of a source at z as observed by an observer at redshift x between the source and earth.

The ratio of the apparent distance (D) resulting from gravitational lensing to the distance (D_F) corresponding to a completely smooth ($\zeta = 1$) Friedmann universe (D_F) is equal to the square root of the determinant of the matrix $\mathcal{B}_s$

$$D = D_F|b_s^2 - \sigma_1^2 - \sigma_2^2|^{1/2}. \tag{2.77}$$

For the rays carrying images of positive ($\det\mathcal{B}_s > 0$) or negative ($\det\mathcal{B}_s < 0$) parity, one can derive from Eq. (2.75) the probability distribution for the distance ratio $m_\pm \equiv D/D_F$,

$$P_{m_\pm} = \frac{Y_s m_\pm}{(Y_s^2 + b_s^2 \mp m_\pm^2)^{3/2}}, \tag{2.78}$$

where $0 \leq m_+ \leq b_s$ and $0 \leq m_- < \infty$. Of course,

$$\int_0^{b_s} P_{m_+} dm_+ + \int_0^\infty P_{m_-} dm_- = 1. \tag{2.79}$$

It is important to understand that the above probabilities pertain to a ray randomly chosen from the 4π angle around earth or any other reference point. As we follow a bundle of rays back to the source, its opening solid angle $\delta\Omega$ will change according to whether the source is amplified or deamplified. Since $\delta\Omega_s = m_\pm^2 \delta\Omega_o$, where Ω_o is the solid angle at the observer and Ω_s is the solid angle at the source, the differential solid angle in the source plane inhabited by the sources whose distance is shifted by factor $m_\pm$ is

$$\frac{d\Omega_s^{(\pm)}}{dm_\pm} = 4\pi m_\pm^2 P_{m_\pm} = 4\pi \frac{Y_s m_\pm^3}{(Y_s^2 + b_s^2 \mp m_\pm^2)^{3/2}}. \tag{2.80}$$

Note that $(4\pi)^{-1}\int_0^{b_s}(d\Omega_s^{(+)}/dm_+)dm_+ = \left(\sqrt{b_s^2 + Y_s^2} - Y_s\right)^2$, which can be shown to be greater than or equal to one, in agreement with every source having at least one image of positive parity. On the other hand, in the simple model we are considering here, the integral $\int_0^\infty (d\Omega_s^{(-)}/dm_-)dm_-$ is infinite, which, within our interpretation, would mean that there should be an "infinite" number of negative parity images for each source. This is hardly relevant from the observer's point of view, for not only is the total flux of those images finite, but only few sources produce negative parity images strong enough to be observed. In fact, as interpreted here, the total flux conservation law [20]

$$\frac{1}{4\pi}\left(\int_0^{b_s}\frac{d\Omega_s^{(+)}}{dm_+}\frac{1}{m_+^2}dm_+ + \int_0^{\infty}\frac{d\Omega_s^{(-)}}{dm_-}\frac{1}{m_-^2}dm_-\right) = 1, \tag{2.81}$$

is nothing but the statement that the total probability, Eq. (2.79), for a single, randomly chosen ray, is one. This conclusion, of course, is independent of the simple model we have been working with.

Angular distribution of magnification in the source plane, Eq.(2.80), is easily translated into the probability distribution $\mathcal{P}_L^{(0)}(D|D_F)$ by

$$\frac{d\mathcal{P}_L^{(0)}(D|D_F)}{dD} = \mathcal{C}\frac{1}{D_F}\frac{1}{4\pi}\frac{d\Omega_s^{(+)}}{dm_+}, \tag{2.82}$$

where we have taken only the images of positive parity into account. The normalization constant $\mathcal{C}$ is necessary to compensate for the fact that in general $(4\pi)^{-1}\int_0^{b_s}(d\Omega_s^{(+)}/dm_+)dm_+ \geq 1$. We thus consider every source to have exactly one image of positive parity.

Equipped with the model distribution (2.82), we can use Eq. (2.71), where $\mathcal{P}$ is given by Eq. (2.60), to maximize expression (2.72) with respect to c and so find an estimate of the bias introduced by gravitational lensing. The numerical computation we actually perform is based on BH-NS binaries with $r_0 = 28$Gpc. As assumed in this section $\lambda_0 = 0$, $\Omega_0 = 1$. We also take $h_0 = 1$. In Fig. 2.7 we depict three cases, $\zeta = 0.8, 0.5, 0.2$ respectively. On the left hand side are typical, Monte-Carlo generated, samples of events in the inhomogeneous universe as they would be observed by perfect, noise-free detectors. The shift of most events towards larger distances relative to the Friedmann redshift-distance curve $D_F(z_s)$ is obvious. Naturally, this effect increases as ζ is lowered. On the right hand side we see those same events as "processed" by noisy detectors. We also show (dashed lines) the redshift-distance curves computed using the corresponding biased parameters $< \hat{c}_\mu >$ as obtained by minimizing Expression (2.72). In the same way we compute the values of bias $b_{c_\mu} \equiv < \hat{c}_\mu > - c_\mu^0$, where c_μ^0 are the real parameters, as functions of $1-\zeta$ which are shown in Fig. 2.8. While b_{c_μ} can be complicated functions of ζ individually, they combine so to give the expected systematic upward shift of the average best-fit curve $D(z)$ (Fig. 2.7). We note that the shift in h_0 is rather small — in fact comparable to the error of statistical inference itself (see Fig. 2.2 with $r_0 = 28$). Roughly the same conclusion seems to

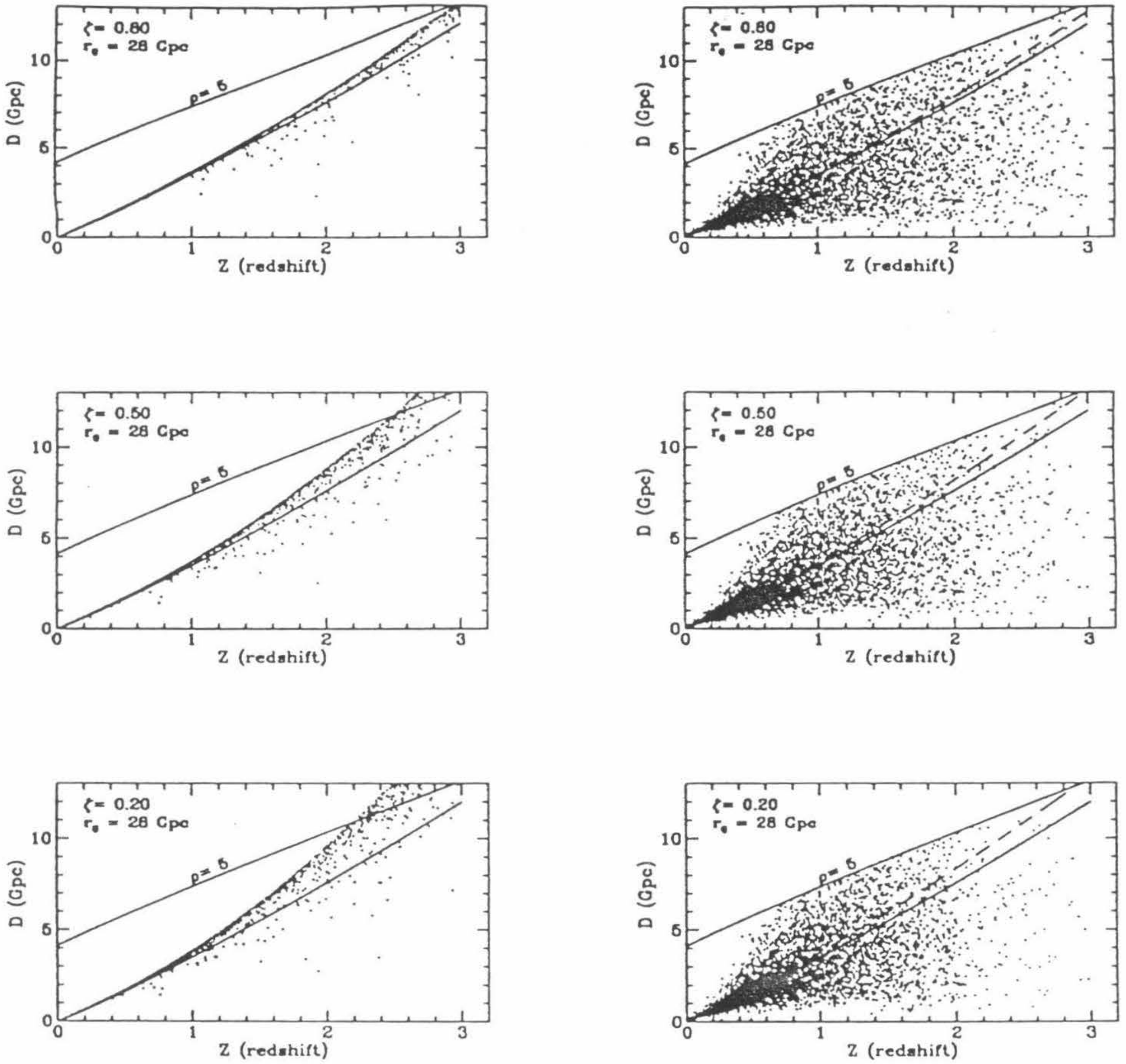

Figure 2.7: The effect of propagation in the inhomogeneous universe for three values of the parameter ζ: 0.8, 0.5, 0.2. $\rho = 5$ curves show the signal to noise limit, Eq. (2.53).

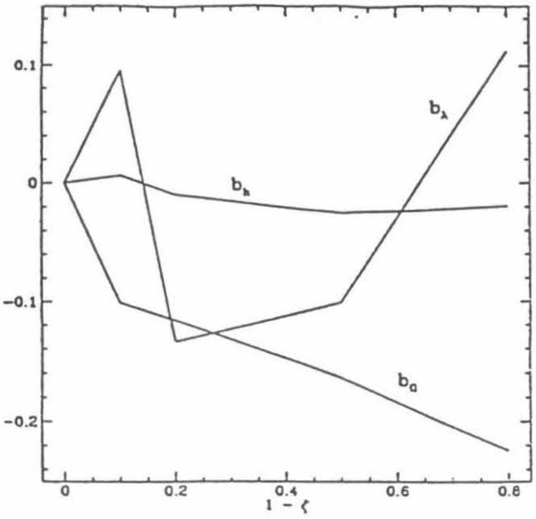

Figure 2.8: Systematic errors due to lensing. See text after Eq. (2.82) for explanation.

hold for Ω_0, while the bias in λ_0, for a strongly clumped universe, can be up to twice as large as the statistical error.

In our computation we have actually taken into account only the main, positive parity images when computing $\mathcal{P}_L^{(0)}(D'|D_F(z_s))$. In reality, the observer might attempt to reduce the bias by using $D = (1/D_+^2 + 1/D_-^2)^{-1/2}$ as a better measure of the distance of a source whose two images were observed at distances D_+ and D_-. That way he would take more observed flux into account, hopefully shift the best-fit curve $D(z)$ a little downward and perhaps get more accurate estimates for c. The two images are indeed likely to be recognized as belonging to the same source because they would have the same waveforms (though with reversed polarizations) and they would come from the same portion of the sky.

To conclude, we emphasize that the arguably large inhomogeneity - induced systematic shifts in observed cosmological parameters, obtained above, should really be considered extremal, since the Schwarzschild lens model we adopted somewhat unrealistically overestimates the number of sources within empty or semi-empty cones, as, indeed, its authors [19] conclude on the basis of more reliable Monte-Carlo computations. Nevertheless, relying on the more general considerations presented earlier in the section, one can expect that the biasing would persist even in much more realistic models, though with smaller, possibly unnoticable magnitude.

Acknowledgments

The author wishes to thank Lars Bildsten, Curt Cutler, L. Samuel Finn, Eanna Flanagan, Eric Poisson, Bernard Schutz, Clifford Will, Allan Wiseman and especially Kip Thorne for invaluable discussions regarding this research and related topics. This research was supported in part by the National Science Foundation, grant No. PHY-9213508 .

Appendix A: Functions F_+ and $F_\times$

We delineate the basis for obtaining numerical values of angle-dependent functions F_+ and $F_\times$ which are used extensively in this article.

The response of a detector [21], whose arms are directed along mutually orthogonal unit vectors $\hat{\mathrm{a}}$ and $\hat{\mathrm{b}}$, to a gravitational wave expressed in "transverse-traceless" coordinates with unit basis vectors e_x^R and e_y^R orthogonal to the direction of propagation,

$$\underline{h} = h_+(\mathrm{e}_x^R \otimes \mathrm{e}_x^R - \mathrm{e}_y^R \otimes \mathrm{e}_y^R) + h_\times(\mathrm{e}_x^R \otimes \mathrm{e}_y^R + \mathrm{e}_y^R \otimes \mathrm{e}_x^R), \tag{2.83}$$

is proportional to

$$h \equiv \mathrm{Tr}\,(\mathrm{D} \cdot \underline{h})\,, \tag{2.84}$$

where

$$\mathrm{D} \equiv \frac{1}{2}(\hat{\mathrm{a}} \otimes \hat{\mathrm{a}} - \hat{\mathrm{b}} \otimes \hat{\mathrm{b}}) \tag{2.85}$$

is the matrix "projecting" the gravitational wave onto the detector. h is a linear function of h_+ and $h_\times$

$$h = F_+(\alpha, \beta, \gamma; \theta, \phi, \psi)h_+ + F_\times(\alpha, \beta, \gamma; \theta, \phi, \psi)h_\times, \tag{2.86}$$

whose angle-dependent coefficients are

$$\begin{aligned} F_+ &= \frac{1}{2}\left[(\hat{\mathrm{a}} \cdot \mathrm{e}_x^R)^2 - (\hat{\mathrm{b}} \cdot \mathrm{e}_x^R)^2 - (\hat{\mathrm{a}} \cdot \mathrm{e}_y^R)^2 + (\hat{\mathrm{b}} \cdot \mathrm{e}_y^R)^2\right] \\ F_\times &= (\hat{\mathrm{a}} \cdot \mathrm{e}_x^R)(\hat{\mathrm{a}} \cdot \mathrm{e}_y^R) - (\hat{\mathrm{b}} \cdot \mathrm{e}_x^R)(\hat{\mathrm{b}} \cdot \mathrm{e}_y^R). \end{aligned} \tag{2.87}$$

In the geocentric frame whose $\hat{\mathrm{k}}$ axis is directed through the northern pole, $\hat{\imath}$ through the intersection of the Greenwich meridian and equator and $\hat{\jmath} \equiv \hat{\mathrm{k}} \times \hat{\imath}$, the relevant vectors are

$$\mathrm{e}_x^R = (\cos\psi\cos\theta\cos\phi + \sin\psi\sin\phi)\hat{\imath}$$

$$\begin{aligned}
& +(\cos\psi\cos\theta\sin\phi - \sin\psi\cos\phi)\hat{\jmath} \\
& -\cos\psi\sin\theta\hat{\mathbf{k}} \\
\mathbf{e}_y^R &= (-\sin\psi\cos\theta\cos\phi + \cos\psi\sin\phi)\hat{\imath} \\
& +(-\sin\psi\cos\theta\sin\phi - \cos\psi\cos\phi)\hat{\jmath} \\
& +\sin\psi\sin\theta\hat{\mathbf{k}} \\
\hat{\mathbf{a}} &= (-\cos\gamma\sin\alpha - \sin\gamma\sin\beta\cos\alpha)\hat{\imath} \\
& +(\cos\gamma\cos\alpha - \sin\gamma\sin\beta\sin\alpha)\hat{\jmath} \\
& +\sin\gamma\cos\beta\hat{\mathbf{k}} \\
\hat{\mathbf{b}} &= (\sin\gamma\sin\alpha - \cos\gamma\sin\beta\cos\alpha)\hat{\imath} \\
& +(-\sin\gamma\cos\alpha - \cos\gamma\sin\beta\sin\alpha)\hat{\jmath} \\
& +\cos\gamma\cos\beta\hat{\mathbf{k}}.
\end{aligned} \tag{2.88}$$

The above vectors can then be used to compute functions F_+ and $F_\times$. It is straightforward to show that in the special case, $\alpha = 0, \beta = \pi/2, \gamma = -\pi/2$, the expressions for F_+ and $F_\times$ reduce to the more familiar form [5]

$$\begin{aligned}
F_+ &= \frac{1}{2}\cos 2\psi(1+\cos^2\theta)\cos 2\phi + \sin 2\psi\cos\theta\sin 2\phi \\
F_\times &= -\frac{1}{2}\sin 2\psi(1+\cos^2\theta)\cos 2\phi + \cos 2\psi\cos\theta\sin 2\phi.
\end{aligned} \tag{2.89}$$

Appendix B: Bias and error in mathematical statistics

In this appendix we summarize some known mathematical results pertinent to the problem of estimating parameters of a probability distribution, given a set of measurements [22]. Suppose we have a set of measurement results $\mathbf{x}_1, \mathbf{x}_2, \ldots, \mathbf{x}_n$. Each of the results is itself a set of m numbers. Suppose also that the measurements are distributed within an m-dimensional set S according to the probability distribution $P(\mathbf{x}|\mathbf{c})$ ($\int_S P d^m x = 1$), where $\mathbf{c}$ denotes a set of p parameters which are *a priori* unknown.

Having performed the n measurements, we find the best-fit parameters $\hat{\mathbf{c}}$ by choosing them to maximize the likelihood function

$$\mathcal{L}(\{\mathbf{x}\}, \mathbf{c})) \equiv P(\mathbf{x}_1|\mathbf{c})P(\mathbf{x}_2|\mathbf{c})\cdots P(\mathbf{x}_n|\mathbf{c}). \tag{2.90}$$

Any statistical inference is, in principle, subject to error and bias in the inferred parameters. For each parameter c_μ the variance of estimation is defined as

$$\sigma^2_{c_\mu} \equiv < \hat{c}^2_\mu > - < \hat{c}_\mu >^2, \tag{2.91}$$

where $< >$ denotes the expectation value of an ensemble whose each member consists of n measurements under the same conditions; $\hat{c}_\mu$ are the values of parameters estimated from the n measurements in a member of the ensemble. On the other hand, the bias

$$b_\mu \equiv < \delta c_\mu > = < \hat{c}_\mu > - c^0_\mu \tag{2.92}$$

is the systematic departure of estimated parameters from the "true parameters" $\mathbf{c}^0$. One can show [22] that, in the limit of large number of measurements n, the maximum likelihood method gives unbiased estimation ($b_\mu = 0$), with the covariance matrix,

$$\Sigma^{(n)}_{\mu\nu} \equiv < (\hat{c}_\mu - c^0_\mu)(\hat{c}_\nu - c^0_\nu) > \tag{2.93}$$

equal to the inverse of the so called "information matrix"

$$I^{(n)}_{\mu\nu} \equiv n \int_S \left(\ln P(\mathbf{x}|\mathbf{c}^0)\right)_{,\mu} \left(\ln P(\mathbf{x}|\mathbf{c}^0)\right)_{,\nu} P(\mathbf{x}|\mathbf{c}^0) d^m x, \tag{2.94}$$

where $(\ln P)_{,\mu}$ denotes derivative with respect to the μ-th parameter c_μ. These asymptotic values are known as the Frechet - Cramer - Rao (FCR) limit. One can actually prove that the above covariance is the minimum that can be achieved by any unbiased statistical method.

Assume now that, due to our ignorance about the actual functional dependence $P(\mathbf{x}|\mathbf{c})$, we are trying to fit the results of measurements to a (slightly) wrong distribution $P(\mathbf{x}|\mathbf{c})$ instead of to the correct one $P_0(\mathbf{x}|\mathbf{c})$. We therefore are searching for the maximum of the logarithm of the likelihood function (4.68),

$$(\ln \mathcal{L})_{,\mu} = \sum_{i=1}^{n} \frac{P_{,\mu}(\mathbf{x}_i|\mathbf{c})}{P(\mathbf{x}_i|\mathbf{c})} = 0. \tag{2.95}$$

Again, we denote by $\hat{\mathbf{c}}$ the parameters inferred in that way.

Averaged over the "real" distribution P_0, Eq. (2.95) gives

$$\Psi_{,\mu} = 0, \tag{2.96}$$

where

$$\Psi(\mathbf{c}|\mathbf{c}_0) = \int_S P_0(\mathbf{x}|\mathbf{c}_0) \ln P(\mathbf{x}|\mathbf{c}) d^m x. \tag{2.97}$$

Then, in the limit of large n a good estimate of bias, Eq. (4.70), at a given $\mathbf{c}^0$ can be obtained by finding that value of $\mathbf{c}$ which maximizes $\Psi(\mathbf{c}|\mathbf{c}^0)$, or, equivalently, satisfies condition (2.96).

For a set of n measurements, one can expand $\ln \mathcal{L}$ around the maximum

$$\ln \mathcal{L} = (\mathcal{L})_{\hat{\mathbf{c}}} + \frac{1}{2} (\ln \mathcal{L})_{,\mu\nu} \, \Delta c_\mu \Delta c_\nu + \cdots . \tag{2.98}$$

For large n one can approximate the coefficients in the above equation by their average values with respect to distribution P_0. One thereby obtains an approximately Gaussian distribution for shifts $\Delta\mathbf{c}$ of the parameters about $\mathbf{c}^B \equiv \mathbf{c}^0 + \mathbf{b}$

$$\mathcal{L} \propto \exp\left(-\frac{1}{2} I^{B(n)}_{\mu\nu} \Delta c_\mu \Delta c_\nu \right), \tag{2.99}$$

where $I^{B(n)}_{\mu\nu} = -n \, (\ln \Psi)_{,\mu\nu}$, computed at $\mathbf{c}^B$. Defining $\delta P \equiv P_0 - P$, one obtains

$$I^{B(n)}_{\mu\nu} = n \int_S \frac{P_{,\mu} P_{,\nu}}{P} d^m x + n \int_S \delta P \left(\frac{P_{,\mu} P_{,\nu}}{P^2} - \frac{P_{,\mu\nu}}{P} \right) d^m x. \tag{2.100}$$

The mean spread of inferred parameters $\hat{\mathbf{c}}$ around the biased means is now given by the matrix

$$\Sigma^{B(n)}_{\mu\nu} = < (\hat{c}_\mu - c^B_\mu)(\hat{c}_\nu - c^B_\nu) >, \tag{2.101}$$

which is the inverse of $I^{B(n)}_{\mu\nu}$. Naturally, in the lowest order in δP, the spread is the same as in Eqs. (2.93) and (2.94) for the unbiased case.

Bibliography

[1] A. Abramovici *et al.*, Science **256**, 325 (1992).

[2] C. Bradaschia *et al.*, Nucl. Instrum. and Methods **A289** 518 (1990).

[3] E. S. Phinney, Astrophys. J. **380**, L17 (1991); R. Narayan, T. Piran and A. Shemi, *ibid.* **379**, L17 (1991).

[4] E.Flanagan and K.S. Thorne, Phys. Rev. D, in preparation.

[5] K. S. Thorne, in *300 Years of Gravitation*, eds. S. W. Hawking and W. Israel (Cambridge University Press, Cambridge, 1987), p. 330.

[6] B. F. Schutz, Nature **323**, 310 (1986); A. Krolak and B.F. Schutz, Gen. Rel. Gravit., **19**, 1163 (1987). B. F. Schutz, Class. Quantum Gravity **6**, 1761 (1989).

[7] C. Cutler *et al.*, Phys. Rev. Let., **70**, 2984 (1993).

[8] L. S. Finn and D. F. Chernoff, Phys. Rev. D **47**, 2198 (1993); C. Cutler and E. E. Flanagan, Phys. Rev., in preparation.

[9] E. Poisson, Phys. Rev. D **47**, 1497 (1993); Kidder, Wiseman, Will, *ibid.* **47**, 4183 (1993).

[10] J. E. Felten, Rev. Mod. Phys. **58**, 689 (1986); S. M. Carrroll, W. H. Press and E. L. Turner, Ann. Rev. Astr., **30**, 499 (1992); S. Weinberg, *Gravitation and Cosmology*, (Wiley, New York, 1972).

[11] G. Börner, *The Early Universe* (Springer-Verlag, Berlin-New York, 1992).

[12] L. A. Wainstein and V. D. Zubakov, *Extraction of Signals from Noise* (Dover, New York, 1970).

[13] F. Nagase, Publ. Astron. Soc. Japan **41**, 1 (1989); A. Wolszcan, Nature **350**, 25 (1991); T. A. Prince, Astrophys. J. **374** L41 (1991).

[14] J. Aitchison and J. A. C. Brown, *The Lognormal Distribution*, (Cambridge at the University Press, Cambridge, 1957).

[15] Preliminary results of numerical computations along these lines indicate increase in errors for the cosmological parameters of less than about 50% relative to those quoted in the text, at the advanced LIGO level. In these computations $n_0(z_s)$ was modeled by a function dependent on a set of (four) parameters which were inferred together with the cosmological parameters by the method of maximum likelihood. Furthermore, as one could expect, this relative increase in error tends to fall itself with an increasing r_0.

[16] R. D. Blandford and R. Narayan, Ann. Rev. Astr., **30**, 311 (1992); P. Schneider, J. Ehlers and E. E. Falco, *Gravitational Lensing* (Springer-Verlag, Berlin-New York, 1992).

[17] C. C. Dyer and R. C. Roeder, Astrophys. J. **180**, L31 (1973).

[18] C. W. Misner, K. S. thorne and J. A. Wheeler, *Gravitation* (Freeman, New York, 1973).

[19] P. Schneider and A. Weiss, Astrophys J. **327**, 526 (1988).

[20] S. Weinberg, Astrophys. J. **208** L1 (1976).

[21] R. L. Forward, Phys. Rev. D **17**, 379 (1978).

[22] H. Cramer, *Mathematical Methods of Statistics* (Princeton University Press, Princeton, 1946); S. L. Meyer, *Data Analysis for Scientists and Engineers* (Wiley, New York, 1975).

Chapter 3

Vacuum for a massless scalar field outside a collapsing body in de Sitter spacetime [Co-authored with William G. Unruh]

(Originally appeared in Phys. Rev. in Phys. Rev. D **43**, 332 (1991).)

Abstract

We present a general way to define regular vacuum states of a quantized massless scalar field in two-dimensional spacetimes with horizons. We discuss in more detail the cases of Schwarzschild-de Sitter spacetime and especially the exterior of a massive shell that collapses to form a black hole in a two-dimensional de Sitter spacetime. In the latter case a vacuum state is defined using modes of positive frequency with respect to the past cosmological horizon's affine parameter. In this vacuum static observers, long after the shell has collapsed, detect thermal fluxes coming from both the cosmological and the black hole horizons, and characterized by the corresponding Hawking temperatures. The renormalized stress-energy tensor in this vacuum state is regular everywhere and has precisely the form one would expect from prior experience with de Sitter spacetime and with gravitational collapse spacetimes that have a vanishing cosmological constant.

1 Introduction

During the sixteen years since Hawking [1] discovered that black holes should emit thermal radiation, a clear understanding of the quantum field theory properties of spacetime horizons has emerged [2]-[6]. Among the horizons that have been studied are those of Schwarzschild spacetime, Kerr spacetime, and de Sitter spacetime, as well as gravitational collapse spacetimes that are asymptotically Schwarzschild or Kerr in the future. In each of these spacetimes, when a quantum field is in an "Unruh-type" [2] vacuum state, the field's properties are remarkably simple and aesthetic: (i) Particle detectors at rest just above the horizon, and also detectors at rest far from the horizon ("static detectors"), measure the horizon to emit perfectly thermal radiation at the "Hawking temperature"; (ii) the renormalized stress-energy tensor $T^{\mu\nu}$ is regular at the horizon; (iii) far from the horizon $T^{\mu\nu}$ has the form of outgoing, thermal radiation; (iv) near the horizon $T^{\mu\nu}$ has the form of downgoing thermal radiation, but with negative energy density rather than positive — as is required by energy-momentum conservation; (v) the near-horizon renormalized $T^{\mu\nu}$ can be regarded as the naive flat spacetime stress-energy tensor corresponding to the quanta measured by static particle detectors, minus a contribution from vacuum polarization which is precisely thermal at the horizon's temperature [6, 7].

Recently Hiscock [8] has argued that there is a breakdown in these properties in the case of a body that collapses to form a black hole in de Sitter spacetime. Such a spacetime is more complex than those studied previously because it has two horizons, the black hole horizon and the cosmological horizon, with two different temperatures, T_h and T_c. The temperature difference, Hiscock speculated, forces the renormalized stress-energy tensor in every vacuum state to be divergent at at least one of the horizons. Correspondingly, Hiscock implied, if Nature chooses a vacuum state that is well behaved at the cosmological horizons (as one would expect), gravitational collapse will produce a black hole horizon that has a divergent renormalized $T^{\mu\nu}$. If true, this would mean that quantum field theory produces an instability of the black hole horizon. As evidence for this speculation, Hiscock enumerated several possible vacuum states for a massless scalar field and showed that each of them had a divergent $T^{\mu\nu}$ at one of the horizons.

In this paper we show that Hiscock's conjecture is incorrect: There do exist states in both the "eternal" black-hole/de Sitter spacetime (otherwise called Schwarzschild - de Sitter spacetime) and the gravitational collapse/de Sitter spacetime which are regular on all of the horizons, cosmological and black hole. These states have the nice properties enumerated above, including renormalized stress-energy tensors, $T_{\mu\nu}$, which are regular at all of the horizons.

Throughout this paper we will restrict our attention to two-dimensional model spacetimes in which the θ ϕ dependence of the metric is suppressed. Consider, first, the two-dimensional eternal black-hole/de Sitter spacetime [3]. In this spacetime the left and right moving modes are uncoupled. As an aid in defining our vacuum state, we choose two null geodesics which cross in the region between the black hole horizon and the cosmological horizon. For each of the left and right moving modes, we define positive frequency with respect to the affine parameters along these null geodesics. Since the affine parameters are regular along each of these null geodesics as they cross the horizons, the vacuum state defined with respect to these affine parameters will also be regular on the horizons, leading to regular stress energy tensors at each of the horizons. One can easily see that this vacuum state is not invariant with respect to the time translation isometry of Schwarzschild-de Sitter spacetime. This property is indeed inevitable according to Kay and Wald [9], who have proved the nonexistence of stationary, nonsingular states in Schwarzschild-de Sitter spacetime.

In the case of the gravitational collapse/de Sitter spacetime, to which we will devote more attention, we define the vacuum state with respect to the affine parameter along the past cosmological horizon. The positive frequency modes come into the collapsing star, reflect off the origin $r = 0$ within the collapsing body, and propagate outward again. These modes will again be regular along any null line traveling from the past cosmological horizon into the future black hole horizon. This regularity of the outward propagating positive frequency modes along inward propagating surfaces at the horizon again ensures that the stress energy tensor will be regular at the black hole horizon, besides being regular at the past and future cosmological horizons — just as in the case of usual black hole spacetimes [2].

This paper is organized as follows: In Sec. 2 we examine the stress energy tensor for "vacuum" states for a massless scalar field in a static spacetime with a horizon. As did Hiscock, we restrict attention to a two-dimensional version of the spacetime in which the angles (θ, ϕ) are suppressed [10] (this simplifies the calculations). We show that for the stress energy to be regular on the horizon, the null coordinate used to define the vacuum state in the manner of Davies, Fulling and Unruh (DFU) [11] must have certain smoothness properties across the horizon. As mentioned above, the null coordinates defined as the affine parameters of a pair of crossing null geodesics indeed have these smoothness properties. We also briefly outline the application of these ideas to to the eternal black-hole/de Sitter spacetime. In Sec. 3 we specialize to the geometry of the gravitational collapse/de Sitter spacetime. For simplicity we take the collapsing body to be a thin, spherical, massive shell. In Sec. 4 we introduce the vacuum state which we designate by $| \mathcal{V}\rangle$, and in Sec. 5 we explore its properties at early times, before the collapse begins, and at late times, after the black hole horizon forms. Among other things, we show that in this vacuum state static particle detectors measure incoming modes to be precisely thermally populated at the temperature of the cosmological horizon (which is where these modes originate). Outgoing modes, by contrast, are measured by static detectors to be populated in different manners before the collapse and after the collapse: before, they are thermally populated at the cosmological temperature; afterward, they are thermally populated at the black hole temperature. In Sec. 6 we evaluate the renormalized stress-energy tensor in the $| \mathcal{V}\rangle$ vacuum and show that it has all the nice properties that one might expect from prior experience: It is regular at all horizons; and near each future horizon it is the $T^{\mu\nu}$ of radiation flowing into the horizon — radiation that is a superposition of perfectly thermal radiation at the black hole temperature and at the cosmological temperature, with positive energy associated with the temperature of the distant horizon and negative energy with that of the nearby one. This $T^{\mu\nu}$ has just the form that one expects from the "membrane paradigm" [6, 7]: it is the naive stress-energy corresponding to the measurements made by static particle detectors, minus that of perfectly thermal radiation at the temperature of the nearby horizon.

2 Regular states on a static horizon

In this section we will be concerned with requirements that a state must satisfy in order that the stress energy tensor be regular on a horizon. We will show that the requirement is that the state itself be regular on the horizon. We will work in a two-dimensional static spacetime, with the field of interest being a massless scalar field.

By a suitable choice of the spatial coordinate r, we can bring the metric into the form

$$ds^2 = f(r)\, dt^2 - \frac{dr^2}{f(r)}, \tag{3.1}$$

where $f(r)$ is assumed to be zero at $r = r_h$ (the horizon), and to be smooth (have a power series expansion in $r - r_h$) near $r = r_h$.

Using the usual null coordinates in the region exterior to the horizon

$$u = t - r_*, \tag{3.2}$$

and

$$v = t + r_*, \tag{3.3}$$

where $dr_* = dr/f$, we get the following two-dimensional metric:

$$ds^2 = f(r(v-u))dudv. \tag{3.4}$$

If we define new null coordinates

$$V = \int h_v(v)dv, \tag{3.5}$$

and

$$U = \int h_u(u)du, \tag{3.6}$$

where $h_v(v)$ and $h_u(u)$ are some as yet unspecified functions, we can rewrite the metric as

$$ds^2 = \frac{f(r(v-u))}{h_v(v)h_u(u)}dUdV \equiv CdUdV. \tag{3.7}$$

As in Davies, Fulling, and Unruh (DFU) [11] we can define a vacuum state with respect to these UV coordinates by choosing the positive frequency modes of the Klein Gordon field to have the form $e^{-i\omega U}$ and $e^{-i\omega V}$ for $\omega > 0$. The energy momentum tensor in this UV-vacuum is then given in DFU by

$$T_{UU} = -\frac{1}{12\pi}C^{\frac{1}{2}}\partial_U\partial_U C^{-\frac{1}{2}}, \tag{3.8}$$

$$T_{VV} = -\frac{1}{12\pi}C^{\frac{1}{2}}\partial_V\partial_V C^{-\frac{1}{2}}, \tag{3.9}$$

$$T_{UV} = -\frac{1}{96\pi}C\mathcal{R}, \tag{3.10}$$

where $\mathcal{R}$ is the curvature scalar for the spacetime.

This tensor obeys the usual conservation law

$$T^{\mu\nu}{}_{;\nu} = 0, \tag{3.11}$$

which in this case reduces to

$$\begin{aligned} T_{\tilde U\tilde U,\tilde V} &= \frac{\tilde C}{96\pi}\mathcal{R}_{,\tilde U}\,, \\ T_{\tilde V\tilde V,\tilde U} &= \frac{\tilde C}{96\pi}\mathcal{R}_{,\tilde V}\,, \end{aligned} \tag{3.12}$$

in any null coordinate system, $\tilde U\tilde V$. Thus along the null ray $\tilde U = \mathrm{const}$, we have

$$T_{\tilde U\tilde U} = T^0_{\tilde U\tilde U} + \frac{1}{96\pi}\int \tilde C\mathcal{R}_{,\tilde U}d\tilde V, \tag{3.13}$$

and similarly for $T_{\tilde V\tilde V}$ along a $\tilde V = \mathrm{const}$ ray.

We are interested in the behavior of the stress energy tensor at the horizon, $r = r_h$. We define a $\tilde U\tilde V$ coordinate system in which the metric coefficients are regular along the horizon by

$$\begin{aligned} \tilde U &= -e^{-\kappa u}, \\ \tilde V &= e^{\kappa v}, \end{aligned} \tag{3.14}$$

where $\kappa = \frac{1}{2}f'(r_h)$ and where $'$ denotes a derivative with respect to r. In these coordinates the horizon $r = r_h$ is located at $\tilde U = 0$. Using the relation (13), the value of $T_{\tilde V\tilde V}$ on the horizon can be found from the value off the horizon in the interior region. Assuming that the curvature $\mathcal{R}$ is regular everywhere, including on the horizon, we see that $T_{\tilde V\tilde V}$ will be regular on the horizon if it is regular in the rest of the spacetime. We thus need worry only about the behavior of $T_{\tilde U\tilde U}$ on the horizon.

We have

$$T_{\tilde U\tilde U} = \left(\frac{\partial U}{\partial\tilde U}\right)^2 T_{UU}. \tag{3.15}$$

Writing

$$\tilde U = \int \tilde h_u(u)du, \tag{3.16}$$

this becomes

$$\begin{aligned} T_{\tilde U\tilde U} &= \frac{h_u^2(u)}{\tilde h_u^2(u)}T_{UU} \\ &= \frac{1}{48\pi}\frac{1}{\tilde h_u^2(u)}\left[2\frac{\ddot f}{f} - 3\frac{\dot f^2}{f^2} - 2\frac{\ddot h_u}{h_u} + 3\frac{\dot h_u^2}{h_u^2}\right] \\ &= \frac{1}{48\pi}\frac{e^{2\kappa u}}{\kappa^2}\left[\frac{f''f}{2} - \frac{f'^2}{4} - 2\frac{\ddot h_u}{h_u} + 3\frac{\dot h_u^2}{h_u^2}\right], \end{aligned} \tag{3.17}$$

where a dot, $\dot{}$, denotes a derivative with respect to u. The horizon occurs at $u = \infty$, and in order that the stress energy tensor be regular on the horizon, the quantity in brackets must fall off at least as fast as $e^{-2\kappa u}$. The terms in f go as

$$2f''f - f'^2 \approx -f_0'^2 + \mathcal{O}((r - r_h)^2) = -f_0'^2 + \mathcal{O}(e^{-2\kappa u}), \tag{3.18}$$

where $f_0' = df/dr\,|_{r=r_h}$. We must then have

$$2\frac{\ddot{h}_u}{h_u} - 3\frac{\dot{h}_u^2}{h_u^2} = -\frac{f_0'^2}{4} + \mathcal{O}(e^{-2\kappa u}) = -\kappa^2 + \mathcal{O}(e^{-2\kappa u}), \tag{3.19}$$

or

$$4h_u^{\frac{1}{2}}\partial_u^2 h_u^{-\frac{1}{2}} = \kappa^2 + \mathcal{O}(e^{-2\kappa u}). \tag{3.20}$$

Thus for the stress energy to be regular, we must have

$$h_u(u) = e^{\mp\kappa u}(\mathrm{Const.} + \mathcal{O}(e^{-2\kappa u})), \tag{3.21}$$

or

$$\begin{aligned} U &= \int h_u(u)du \\ &= e^{\mp\kappa u}(\mathrm{const.} + \mathcal{O}(e^{-2\kappa u})) \\ &= \tilde{U}^{\pm 1}(\mathrm{const.}' + \mathcal{O}(\tilde{U}^2)). \end{aligned} \tag{3.22}$$

U is the coordinate which is used to define the vacuum state, while $\tilde{U}$ is the coordinate regular on the horizon. Thus this relation states that the coordinates defining the state must be related to the coordinate regular on the horizon either by direct or inverse proportionality. Direct proportionality is easily obtained. Take any null geodesic which intersects the horizon. Define the U coordinate to be the affine parameter along this geodesic. This coordinate will obey the required condition.

The inverse relation is somewhat harder to arrange. The simplest way is to place reflective boundary conditions on the scalar field at some point $r = r_0$ within the spacetime. If we now choose the state such that positive frequencies are defined with respect to the affine parameter, $\tilde{V}$ along the $\tilde{U} = 0$ horizon, then the boundary conditions at $r_0 = r(v - u) = r(ln(-\tilde{V}\tilde{U})/\kappa)$ mean that positive frequencies in the $\tilde{U}$ direction are given by $e^{i\omega'\tilde{U}^{-1}}$ for $\omega' > 0$, which is the required condition. The state we shall examine below for the collapse/de Sitter spacetime is of just such a form.

This inverse relationship is a general one. If we have two coordinates U and $\bar{U}$ where $\bar{U} = 1/U$, then states defined with respect to these two coordinates lead to exactly the same stress energy tensors.

$$\begin{aligned}
\bar{T}_{UU} &= \left(\frac{\partial \bar{U}}{\partial U}\right)^2 \bar{T}_{\bar{U}\bar{U}} \\
&= -\frac{1}{12\pi} U^{-4} \bar{C}^{\frac{1}{2}} \partial^2_{\bar{U}} \bar{C}^{-\frac{1}{2}} \\
&= -\frac{1}{12\pi} U^{-3} C^{\frac{1}{2}} (U^2 \partial_U)^2 C^{-\frac{1}{2}} / U \\
&= -\frac{1}{12\pi} \frac{1}{U} C^{\frac{1}{2}} \partial_U U^2 \partial_U \frac{C^{-\frac{1}{2}}}{U} \\
&= -\frac{1}{12\pi} C^{\frac{1}{2}} \partial^2_U C^{-\frac{1}{2}} \\
&= T_{UU},
\end{aligned} \tag{3.23}$$

while T_{VV} is obviously left unchanged, as is $T_{UV} \propto \mathcal{R}$.

The energy momentum tensor can be simply calculated everywhere in the static spacetime if we choose U and V to be affine parameters along some curves $u = u_0$ and $v = v_0$. In the uv coordinates, the Ricci curvature, $\mathcal{R}$ depends only on $v - u$. Thus the conservation equation reads

$$T_{uu,v} = \frac{f}{96\pi} \mathcal{R}(v-u)_{,u} = -\frac{f}{96\pi} \mathcal{R}(v-u)_{,v} \tag{3.24}$$

so that

$$T_{uu} + \frac{f}{96\pi} \mathcal{R} = \int \frac{f_{,v}}{96\pi} \mathcal{R} dv \tag{3.25}$$

along a u =constant null surface. Now, along the surface $v = v_0$, we choose U to be the affine parameter. Thus the metric $C = 2g_{UV}$ is independent of U along $v = v_0$, and thus T_{UU} (and T_{uu}) is zero along this surface. Furthermore, f depends only on r, so that $f_{,v} = \frac{1}{2} f' f$. We thus have

$$T_{uu} = -\frac{1}{96\pi} \left(f(v-u)\mathcal{R}(v-u) - f(v_0 - u)\mathcal{R}(v_0 - u) - \int_{v_0}^{v} \frac{1}{2} f' f \mathcal{R} dv \right), \tag{3.26}$$

and similarly for T_{vv}.

Finally, we calculate the change in the energy momentum tensor component $T_{\tilde{U}\tilde{U}}$ along the $\tilde{U} = 0$ horizon. We have

$$T_{\tilde{U}\tilde{U}} = T^0_{\tilde{U}\tilde{U}} + \frac{1}{96\pi} \int \tilde{C} \mathcal{R}_{,\tilde{U}} \, d\tilde{V}. \tag{3.27}$$

For our spacetime, $\mathcal{R}$ is a function only of r and is independent of where one is on the horizon. Thus we can write

$$\begin{aligned}
\tilde{C}\mathcal{R}_{,\tilde{U}} &= \mathcal{R}_{,r}\,\tilde{C}f(r)\left(-\frac{1}{2\kappa}\right)e^{\kappa u} \\
&\approx -\tilde{C}\mathcal{R}_{,r}\,(r-r_h)e^{\kappa u} \\
&\approx -\frac{1}{\kappa}\tilde{C}\mathcal{R}_{,r}\,e^{\kappa v} \\
&\approx -\frac{1}{\kappa}\tilde{C}\mathcal{R}_{,r}\,\tilde{V},
\end{aligned} \tag{3.28}$$

and, since $\tilde{C}$ is constant along the horizon, we finally get

$$T_{\tilde{U}\tilde{U}} = T^0_{\tilde{U}\tilde{U}} + \frac{1}{96\pi\kappa}\tilde{C}\mathcal{R}_{,r}\,\frac{\tilde{V}^2}{2}. \tag{3.29}$$

Thus in this affine parameter coordinate system, this component of the stress energy tensor diverges as one travels along the horizon, if $\mathcal{R}_{,r}$ is not equal to zero at the horizon. However, if we transform to the proper reference frames of freely falling observers whose four-velocities are

$$\mathbf{u} = \frac{\sqrt{f_0}}{f}\frac{\partial}{\partial t} - \sqrt{f_0 - f}\,\frac{\partial}{\partial r}, \tag{3.30}$$

where f_0 is f at the points from which the observers are dropped, we find the components of the stress-energy tensor to be finite as $\tilde{V} \to 0$. Specifically, at the horizon we have the following relation:

$$\partial_{\hat{u}} \propto \frac{1}{\tilde{V}}\partial_{\tilde{U}}, \tag{3.31}$$

where $\partial_{\hat{u}}$ is the $\tilde{U}$-directed proper null vector of a freely falling observer. This ensures the finiteness of $T_{\hat{u}\hat{u}}$ as $\tilde{V} \to \infty$ along the horizon.

In order to examine the behavior of $T_{\hat{v}\hat{v}}$, where $\partial_{\hat{v}}$ is the $\tilde{V}$-directed proper null vector of a freely falling observer, we need to see what happens along the null ray $u = u_0$ as $v \to \infty$. There we might approach another horizon, located at $r = r_h' > r_0$, whose surface gravity is κ'. This is indeed the case in the Schwarzschild- de Sitter spacetime [3]. Here r_h is the position of the black hole horizon while r_h' corresponds to r_c, the position of the cosmological horizon (see Sec. 3). Alternatively, there could be a future null infinity ("$\kappa' = 0$"). Again using the relations among $\tilde{V}$-directed vectors at the $r = r_h$ horizon

$$\partial_{\hat{v}} \propto \tilde{V}\partial_{\tilde{V}} \propto \partial_v, \tag{3.32}$$

and the DFU formula we have

$$
\begin{aligned}
T_{\hat{v}\hat{v}} &= \left(\frac{\partial V}{\partial \hat{v}}\right)^2 T_{VV} \\
&\propto h_v^2 C^{\frac{1}{2}} \partial_V^2 C^{-\frac{1}{2}} \\
&\propto \left(e^{\mp\kappa' v}\right)^2 \left(\frac{e^{\kappa(v-u)}}{e^{\mp\kappa u} e^{\mp\kappa' v}}\right)^{\frac{1}{2}} \left(\frac{1}{e^{\mp\kappa' v}}\partial_v\right)^2 \left(\frac{e^{\kappa(v-u)}}{e^{\mp\kappa u} e^{\mp\kappa' v}}\right)^{-\frac{1}{2}} \\
&\propto e^{\pm 2\kappa' v} e^{\mp 2\kappa' v},
\end{aligned}
\tag{3.33}
$$

as $v \to \infty$. Here the upper signs correspond to the choice of affine parameters along $u = u_0$ or $v = v_0$ rays. For instance, near the $v = \infty$ horizon we have either $V \propto \tilde{V}'$ or $V \propto 1/\tilde{V}'$ as discussed above in this section. Hence $h_v(v) \propto \exp(\mp\kappa' v)$. From Eq. (3.33) we see that $T_{\hat{v}\hat{v}}$ is finite at the horizon located at $r = r_h$ even as $\tilde{V} \to \infty$. Together with the finiteness of $T_{\hat{u}\hat{u}}$ and $T_{\hat{u}\hat{v}}$, this guarantees the regularity of the stress energy tensor everywhere on the horizon. Similar arguments can be applied to any horizon that might exist at $u = \pm\infty$ or $v = \pm\infty$.

The eternal black-hole/de Sitter spacetime can be regarded as a special case of the above analysis. By choosing U and V coordinates to be the affine parameters of null lines that cross at the point t_0, r_0 $(r_h < r_0 < r_c)$, we define a vacuum state whose renormalized stress-energy tensor is, according to the above discussion, regular at both the black hole and cosmological horizons. We shall return to this vacuum state at the end of Sec. 4, after first discussing vacua for the gravitational collapse/de Sitter spacetime.

3 The gravitational collapse/de Sitter spacetime

According to the generalization [12] of Birkhoff's theorem to nonzero values of the cosmological constant Λ, the exterior region of a spherically symmetric body of mass M has the Schwarzschild - de Sitter line element:

$$
ds^2 = f(r)dt^2 - \frac{dr^2}{f(r)} - r^2(d\theta^2 + \sin^2\theta d\phi^2),
\tag{3.34}
$$

where $f(r)$ is

$$
f(r) = 1 - \frac{2M}{r} - \frac{\Lambda}{3}r^2.
\tag{3.35}
$$

For the sake of simplicity, we will assume that the massive body is a shell of radius R whose interior is described by the de Sitter line element:

$$ds^2 = g(r)d\tilde{t}^2 - \frac{dr^2}{g(r)} - r^2(d\theta^2 + \sin^2\theta d\phi^2), \tag{3.36}$$

where $g(r)$ is

$$g(r) = 1 - \frac{\Lambda}{3}r^2. \tag{3.37}$$

Requiring that the proper time as measured by a clock on the shell be independent of whether it is calculated using the exterior or interior metric, we obtain:

$$\frac{dt}{d\tilde{t}} = \left\{\frac{1}{f}\left[g + \left(\frac{1}{f} - \frac{1}{g}\right)\left(\frac{dR}{d\tilde{t}}\right)^2\right]\right\}^{1/2}_{r=R(\tilde{t})}. \tag{3.38}$$

We suppose that the radius of the shell is fixed ($R = R_0$) until the moment $\tilde{t} = 0$ when the shell starts imploding. At the moment $\tilde{t} = \tilde{t}_h$, it crosses its horizon radius r_h and forms a black hole.

Of the three zeros of the equation $f(r) = 0$ one, r_-, is negative. The two others, r_h and r_c, are the locations of the black hole and cosmological horizons respectively [13]. The corresponding surface gravities are

$$\begin{aligned} \kappa_h &= \frac{1}{2}\left(\frac{df}{dr}\right)_{r=r_h} = \frac{\Lambda(r_c - r_h)(r_h - r_-)}{6r_h}, \\ \kappa_c &= -\frac{1}{2}\left(\frac{df}{dr}\right)_{r=r_c} = \frac{\Lambda(r_c - r_h)(r_c - r_-)}{6r_c}. \end{aligned} \tag{3.39}$$

The Penrose diagram describing the causal structure of the spacetime is shown in Fig. 3.1.

In this diagram one sees the past ($\mathcal{H}_c^-$) and future ($\mathcal{H}_c^+$) cosmological horizons as well as the future black hole horizon ($\mathcal{H}_h^+$) which is created by the collapse. Note that in this spacetime, by contrast with pure de Sitter, $r = 0$ is uniquely determined: it is the center of the spherical shell.

4 The vacuum state $\mid \mathcal{V}\rangle$

As in Sec. 2, we will ignore the spherical coordinates ϕ and θ, reducing the spacetime to two dimensions.

In addition to u and v, Eqs. (3.2)-(3.4), we shall need a second set of coordinates U and V defined as follows; see Fig. 3.2.

We first define the affine parameter of the past cosmological horizon

$$\mathcal{V} \equiv -e^{-\kappa_c v}. \tag{3.40}$$

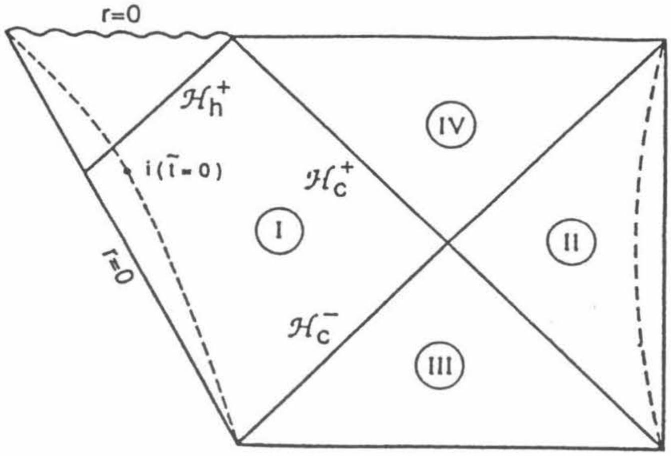

Figure 3.1: Penrose diagram of a gravitational collapse/de Sitter spacetime. The shell in region I starts its collapse at point $\bar{t} = 0$, while the shell in region II remains static forever.

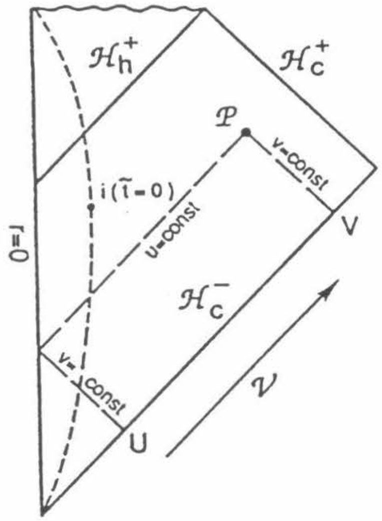

Figure 3.2: The definition of U and V coordinates. For simplicity, only the region I from Fig. 3.1 is depicted.

Then we choose an arbitrary point $\mathcal{P}$ at which the values of U and V are to be defined. The value of $\mathcal{V}$ at which the past directed null ray propagating rightwards from $\mathcal{P}$ hits $\mathcal{H}_c^-$ is the coordinate $V(\mathcal{P})$. This construction gives

$$V = -e^{-\kappa_c v} \tag{3.41}$$

everywhere outside the shell. Similarly, we extend the past directed, leftward propagating null ray from $\mathcal{P}$ through the shell to $r = 0$, and there we reflect it into a past directed, rightward propagating null ray. The value $\mathcal{V}$ at which this ray hits $\mathcal{H}_c^-$ is the coordinate $U(\mathcal{P})$.

Note that the coordinate V can be extended beyond the future cosmological horizon $\mathcal{H}_c^+$.

For $u < u_i$, where $U_i(u_i)$ and $V_i(v_i)$ are the coordinates of the beginning of the implosion, we have the simple relation

$$U = -e^{-\kappa_c u}. \tag{3.42}$$

However for $u > u_i$ this relation is changed. As the point $\mathcal{P}$ gets close to the future black hole horizon, the past directed, leftward propagating ray used to define the coordinate U is strongly affected by the collapsing shell. In this region $(r_* \to -\infty, u \to \infty)$ the metric function f has the following asymptotic behavior:

$$f \propto e^{2\kappa_h r_*} = e^{\kappa_h (v-u)}. \tag{3.43}$$

From this relation and Eq. (3.38) we obtain

$$\frac{dt}{d\tilde{t}} \approx -\frac{\dot{R}}{f} \propto e^{-\kappa_h (v-u)}, \tag{3.44}$$

near the point where the shell crosses its black hole horizon. Using Eqs. (3.43) and (3.44) we can, following the past directed ray through and out of the shell [14], derive the following expression

$$\frac{d \ln(-U)}{du} \propto -e^{-\kappa_h u}, \tag{3.45}$$

which implies

$$e^{-\kappa_h u} \propto -\ln\left(\frac{U}{U_h}\right) \approx \left(1 - \frac{U}{U_h}\right), \tag{3.46}$$

for values of U very close to U_h, the position of the black hole horizon.

We now quantize the real scalar field with respect to the modes proportional to $\exp(-i\omega V)$ or $\exp(-i\omega U)$. Both types of modes originate at the past cosmological horizon $\mathcal{H}_c^-$, where they are positive frequency with respect to the past horizon affine parameter $\mathcal{V}$. Thus, they are a natural extension to our gravitational collapse spacetime of de Sitter invariant modes in a pure de Sitter spacetime. The quantum state which contains no particles in these modes we will call the $\mid \mathcal{V}\rangle$ vacuum. It is a natural generalization of a de Sitter invariant vacuum of de Sitter spacetime. Namely, in the case where the shell has zero mass (pure de Sitter), $\mid \mathcal{V}\rangle$ reduces to the conformal de Sitter vacuum [15]. On the other hand, in the case of a collapsing body in an asymptotically flat spacetime ($\Lambda = 0$), the past horizon affine parameter would be replaced by the advanced time at the past null infinity and our state $\mid \mathcal{V}\rangle$ would become the vacuum state originally discussed by Hawking [1] and subsequently by Unruh [2].

The vacuum $\mid \mathcal{V}\rangle$ is closely related to the vacuum state for the eternal black-hole/de Sitter spacetime discussed in Sec. 2. The vacuum defined there using the affine parameters of any pair of crossing null rays can be shown to exibit late time behavior identical to that of the vacuum $\mid \mathcal{V}\rangle$. By contrast with Schwarzschild/de Sitter, however, in the gravitational collapse/de Sitter spacetime we need only one null ray propagating from the past to the future cosmological horizon to specify the vacuum state $\mid \mathcal{V}\rangle$. This null ray is chosen to coincide with the past cosmological horizon, thereby defining the state's initial conditions in the past relative to all static observers outside the massive body.

5 Properties of $\mid \mathcal{V}\rangle$ as measured by static observers

Because the proper time τ of a static observer ($r = r_{so}$) is proportional to the time coordinate t

$$d\tau = \sqrt{f(r_{so})}dt, \tag{3.47}$$

and hence is also proportional to $u = t - r_*$ and to $v = t + r_*$, a particle detector carried by such an observer detects particles that are of positive frequency with respect to u and v. The corresponding vacuum state $\mid \mathcal{S}\rangle$ ($\mathcal{S}$ for "static observers") is one in which the particle detector sees no quanta in the modes $e^{-i\omega u}$ and $e^{-i\omega v}$.

The relation (41) between the null coordinates V of the $\mid \mathcal{V}\rangle$ vacuum and v of the $\mid \mathcal{S}\rangle$ vacuum implies that when the field is in the $\mid \mathcal{V}\rangle$ state, static observers will see the modes $e^{-i\omega v}$ thermally populated at the cosmological temperature

$$T_c = \frac{\kappa_c}{2\pi}. \tag{3.48}$$

Stated more precisely, when studying observables confined to region I of the spacetime, one can regard the pure state $\mid \mathcal{V}\rangle$ as being equal to a mixed state that is obtained from $\mid \mathcal{S}\rangle\langle\mathcal{S}\mid$ by populating all the incoming modes $e^{-i\omega v}$ thermally at temperature T_c [16].

Similarly, the asymptotic relations between U and u at early and late times imply that, for outgoing modes $e^{-i\omega u}$, the $\mid \mathcal{V}\rangle$ vacuum is seen by static observers as obtained by populating $\mid \mathcal{S}\rangle\langle\mathcal{S}\mid$ thermally at the cosmological temperature T_c at early times (before the collapse) and at the black hole temperature

$$T_h = \frac{\kappa_h}{2\pi} \tag{3.49}$$

at late times (after the collapse).

These thermal population properties of $\mid \mathcal{V}\rangle$ show up not only in the mathematical expressions for $\mid \mathcal{V}\rangle$ in terms of $\mid \mathcal{S}\rangle$, but also in the behavior of static particle detectors. Consider, for concreteness, a model particle detector that is adiabatically switched on at late times (long after the collapse). When the quantum field $\phi(x)$ is in the state $\mid \mathcal{V}\rangle$, its influence on the detector is described by the Wightman function [17]

$$\begin{aligned} D^+_{\mathcal{V}}(x,x') &\equiv \langle\mathcal{V}\mid\phi(x)\phi(x')\mid\mathcal{V}\rangle \\ &= -\frac{1}{4\pi}\ln\left[(V-V'-i\epsilon)(U-U'-i\epsilon)\right]. \end{aligned} \tag{3.50}$$

Using this Wightman function and the asymptotic expression (46) for large u, we find that the transition rate from the ground state of the detector to an excited state of energy E is proportional to the response function

$$\mathcal{F}(E) = \frac{1}{2E}\left(\frac{1}{e^{E\alpha/T_h}-1} + \frac{1}{e^{E\alpha/T_c}-1}\right). \tag{3.51}$$

Here $\alpha(r_{so}) \equiv \sqrt{f(r_{so})}$ is the "lapse function," which blue shifts the temperature. Expression (51) confirms that the detector behaves as though it were bathed by cosmological and black hole thermal fluxes coming from opposite directions and having the temperatures T_c and T_h respectively. That this conclusion does not depend on the position of the detector relative to the horizons is due to the fact that in two spacetime dimensions the quanta propagate freely, without encountering any centrifugal barrier and without scattering off spacetime curvature [2, 5].

6 The vacuum stress-energy tensor

The renormalized stress-energy tensor of the conformally coupled scalar field in the $\mid \mathcal{V}\rangle$ vacuum of our two-dimensional spacetime is given by the DFU formulae, Eqs. (3.8)-(3.10).

Before the collapse starts ($U < U_i$) this stress-energy tensor, transformed to the proper reference frame of a static observer, has the following time independent form:

$$T_{\hat{\mu}\hat{\nu}} = \frac{1}{24\pi}\frac{1}{f}\left[\kappa_c^2 - \frac{\Lambda}{3} + \frac{2M\Lambda}{r} - \frac{2M}{r^3} + \frac{3M^2}{r^4}\right] I_{\hat{\mu}\hat{\nu}} - \frac{\mathcal{R}}{48\pi} g_{\hat{\mu}\hat{\nu}}, \tag{3.52}$$

where $I_{\hat{\mu}\hat{\nu}}$ is the unit 2×2 matrix.

As we approach the cosmological horizon ($r \to r_c$) for $U < U_i$, the first term in Eq. (3.52) vanishes and we are left with the simple expression

$$T_{\mu\nu} = -\frac{\mathcal{R}}{48\pi} g_{\mu\nu}. \tag{3.53}$$

This $T_{\mu\nu}$ is obviously regular at the horizon.

Long after the collapse starts, at $u \gg u_i$, we have

$$\begin{aligned} T_{tt} &= \frac{1}{48\pi}\left[\kappa_c^2 + \kappa_h^2 - 2F(r)\right] - \frac{1}{48\pi}\mathcal{R}f + \mathcal{O}\left(e^{-2\kappa_h u}\right), \\ T_{rr} &= \frac{1}{f^2}T_{tt} + \frac{1}{48\pi}\frac{2\mathcal{R}}{f}, \\ T_{tr} &= \frac{1}{48\pi}\frac{1}{f}\left[\kappa_c^2 - \kappa_h^2\right] + \mathcal{O}\left(e^{-2\kappa_h u}\right), \end{aligned} \tag{3.54}$$

where

$$F(r) \equiv \frac{1}{4}f'^2 - \frac{1}{2}ff''. \tag{3.55}$$

At $u \gg u_i$ static observers observe the thermal radiation coming from the black hole, in addition to the already existing cosmological Hawking radiation. Very close to the black hole horizon, $r \to r_h$ ($v - u \to -\infty$), we have

$$F(r) = \kappa_h^2 + \mathcal{O}\left(e^{2\kappa_h(v-u)}\right). \tag{3.56}$$

In that region the renormalized stress-energy tensor (54) in a static observer's proper frame is:

$$T_{\hat{t}\hat{t}} \;=\; \frac{\pi}{12}\left[\left(\frac{T_c}{\alpha}\right)^2 - \left(\frac{T_h}{\alpha}\right)^2\right] - \frac{\mathcal{R}}{48\pi} + \text{h.o.},$$

$$\begin{aligned} T_{\hat{r}\hat{r}} &= \frac{\pi}{12}\left[\left(\frac{T_c}{\alpha}\right)^2 - \left(\frac{T_h}{\alpha}\right)^2\right] + \frac{\mathcal{R}}{48\pi} + \text{h.o.}, \\ T_{\hat{t}\hat{r}} &= T_{\hat{r}\hat{t}} = \frac{\pi}{12}\left[\left(\frac{T_c}{\alpha}\right)^2 - \left(\frac{T_h}{\alpha}\right)^2\right] + \text{h.o.}, \end{aligned} \tag{3.57}$$

where h.o. denotes terms of second order or higher in $\alpha \equiv \sqrt{f}$.

The leading, $\mathcal{O}(\alpha^{-2})$ terms in (57) have precisely the form of ingoing thermal radiation in two-dimensional spacetime, except that the sign of the component at temperature T_h is negative rather than positive. This result, obtained directly from the Davies-Fulling-Unruh formulae, Eqs. (3.8)-(3.10), has a simple interpretation in terms of measurements made by static observers — an interpretation embodied in the "membrane paradigm" for black holes [6, 7]: The static observers, near the horizon, measure outgoing modes to be precisely thermally populated at the temperature T_h, and incoming modes precisely thermal at temperature T_c. The rule for renormalization, in terms of these static observers' measurements, is to subtract off, in all modes, a thermal contribution with temperature T_h. Doing so leaves zero net renormalized stress-energy in the outgoing modes and leaves in the incoming modes the difference between a thermal flux at temperature T_c and that at T_h — which is precisely the $\mathcal{O}(\alpha^{-2})$ contribution to expression (57).

Turn attention now from the vicinity of the black hole horizon to the vicinity of the future cosmological horizon, long after the collapse. Near the cosmological horizon, $r \to r_c$ $(v - u \to \infty)$, we have

$$F(r) = \kappa_c^2 + \mathcal{O}\left(e^{-2\kappa_c(v-u)}\right). \tag{3.58}$$

There the renormalized stress-energy tensor (54) in the proper reference frame of a static observer takes the following form

$$\begin{aligned} T_{\hat{t}\hat{t}} &= \frac{\pi}{12}\left[\left(\frac{T_h}{\alpha}\right)^2 - \left(\frac{T_c}{\alpha}\right)^2\right] - \frac{\mathcal{R}}{48\pi} + \text{h.o.}, \\ T_{\hat{r}\hat{r}} &= \frac{\pi}{12}\left[\left(\frac{T_h}{\alpha}\right)^2 - \left(\frac{T_c}{\alpha}\right)^2\right] + \frac{\mathcal{R}}{48\pi} + \text{h.o.}, \\ T_{\hat{t}\hat{r}} &= T_{\hat{r}\hat{t}} = -\frac{\pi}{12}\left[\left(\frac{T_h}{\alpha}\right)^2 - \left(\frac{T_c}{\alpha}\right)^2\right] + \text{h.o.}, \end{aligned} \tag{3.59}$$

Like the $T_{\mu\nu}$ near the black hole horizon, this has the simple, standard membrane-paradigm interpretation of being, at $\mathcal{O}(\alpha^{-2})$, the stress-energy tensor measured by static observers, minus the contribution of perfectly thermal radiation at temperature T_c in all modes.

Expressions (57) and (59) exhibit the usual blue shift of temperature (factors α^{-2}), which causes the stress-energy as measured by static observers to become infinite as either of the horizons is approached. This divergence, however, is an artifact of the pathological behavior of the static observers' reference frames at the horizons. To verify that the stress-energy tensor is, in fact, regular at both horizons, we can transform to the proper reference frame of a freely falling observer whose four-velocity is

$$\mathbf{u} = \frac{\sqrt{f_0}}{f}\frac{\partial}{\partial t} \pm \sqrt{f_0 - f}\frac{\partial}{\partial r}. \qquad (3.60)$$

Here f_0 is f at the starting point of the free fall, the $+$ and $-$ signs pertain to the observer falling towards the cosmological or black hole horizons respectively. We can either repeat the argument presented following Eq. (3.29) or use the late time expressions Eqs. (3.54), as well as Eq. (3.56) (at the black hole horizon) or Eq. (3.58) (at the cosmological horizon), to verify that in a freely falling observer's reference frame, the stress-energy tensor remains finite as the observer crosses any of the horizons, regardless of where the crossing point is located.

7 Conclusion

In this paper we have seen that quantum field theory does not induce an instability of the black hole horizon formed by gravitational collapse in de Sitter spacetime. Rather, when a massless scalar field is in the natural generalization of the de Sitter vacuum (also a natural generalization of the Unruh vacuum), it remains everywhere well behaved — and, indeed, behaves in just the manner one would expect from the study of quantum field theory in other horizon-endowed spacetimes.

After the original version of this paper was submitted for publication, we received a preprint by Shin-ichi Tadaki and Shin Takagi which reaches the same principal conclusions as we derive in Secs. 4 and 6 — but describes them in somewhat different language [18].

Acknowledgments

D.M. wishes to thank Kip S. Thorne for advice about this research. He is also grateful to Paul Coppi and Aharon Melman for introducing him to computer typesetting. D.M. was supported in part by the National Science Foundation, Grant

AST – 8817792. W.G.U. was supported in part by NSERC Grant 580441, by the Canadian Institute for Advanced Research and by the LAC Minerals Corporation.

Bibliography

[1] S.W. Hawking, Commun. Math. Phys., **43**, 199 (1975); see also R.M. Wald, *General Relativity* (Chicago University Press, Chicago, 1984), chap. 14, for a lucid introduction.

[2] W.G. Unruh, Phys. Rev. D **14**, 870 (1976).

[3] G.W. Gibbons and S.W. Hawking, Phys. Rev. D **14**, 2738 (1977).

[4] N.D. Birrell and P.C.W. Davies, *Quantum Fields in Curved Space* (Cambridge University Press, Cambridge, UK, 1982), sect. 8.1.

[5] K.S. Thorne, R.H. Price and D.A. Macdonald, *Black Holes: The Membrane Paradigm* (Yale University Press, Yale, 1986), chap. VIII.

[6] V.P. Frolov and K.S. Thorne, Phys. Rev. D **39**, 2125 (1989).

[7] See sects. VIIIB6 and VIIIB7 of Ref. 5.

[8] W.A. Hiscock, Phys. Rev. D **39**, 1067 (1989).

[9] B. S. Kay and R.M. Wald, "Theorems on the Uniqueness and Thermal Properties of Stationary, Nonsingular, Quasi-free States on Spacetimes with a Bifurcate Killing Horizon" (preprint, 1989).

[10] For the relation between the two-dimensional and four-dimensional cases, see L.H. Ford and L. Parker, Phys. Rev. D **17**, 1485 (1978), sect. II.

[11] P.C.W. Davies, S.A. Fulling and W.G. Unruh, Phys. Rev. D **13**, 2720 (1976).

[12] J. Morrow-Jones, Ph.D. thesis, University of California, Santa Barbara, 1988.

[13] G. Denardo and E. Spallucci, Nuovo Cimento B **53**, 334 (1979).

[14] See Ref. 4, sect. 8.1.

[15] See Ref. 4, sect. 5.4.

[16] W. Israel, Phys. Lett. **57A**, 107 (1976).

[17] See Ref. 4, sects 3.3 and 8.3.

[18] S. Tadaki and S. Takagi, Prog. Theor. Phys. **83**, 941 (1990); **83**, 1126 (1990).

Chapter 4

Convection in a spherically symmetric accretion flow

Abstract

We develop a simple model of convection in a fluid spherically accreting onto a black hole. The model is based on a generalization of the standard mixing length theory of convection and is applicable if the convective velocities are either larger or smaller than the accretion velocity. The change in the accretion velocity with radius leads to a radial stretching of the inflowing fluid which impedes convection. Thus, in order for convection to occur, the specific entropy has to grow inward at the rate higher than some threshold value ($dS/dr < (dS/dr)_{\mathrm{threshold}} < 0$), which modifies the familiar Schwarzscild criterion for convection. However, this minimum rate is of such a small magnitude that even, for instance, optically thick, gas-pressure dominated accretion flows, discussed by Flammang, would necessarily involve convection, though the convective luminosity would be small compared to the total luminosity. We illustrate our model through its application to an accretion onto a small primordial black hole at the centre of a Sun-like star.

1 Introduction and summary

1.1 Motivation

Despite its seeming simplicity the problem of the luminosity produced by an optically thick, spherically symmetric accretion onto a black hole resisted various attempts at solution for a relatively long period of time [1]. Finally a series of papers by Flammang and collaborators [1, 2, 7] provided a first self-consistent, relativistic treatment of accretion under a broad range of conditions in either radiation or gas-pressure dominated environments. Flammang succeeded in isolating a well-behaved solution, $\hat{L}_o(r)$, for the luminosity, which is unique for a given mass of the black hole and environmental density and temperature. If we neglect the mass of the accreting fluid enclosed within radius r, this solution approaches, at large radii, a constant value which we will call the Flammang luminosity, and whose value in the gas-pressure dominated case is [7]

$$L_{\mathrm{Fl}} = 4\frac{\Gamma - 1}{\Gamma}\frac{P_{\mathrm{rad}}}{P_{\mathrm{gas}}}\frac{4\pi GMc}{\kappa}, \tag{4.1}$$

where P_{rad} and P_{gas} are the radiation and gas pressures in the fluid surrounding the black hole and $\Gamma \approx 5/3$ is the adiabatic exponent of the gas.

If, in order to examine certain arguably realistic astrophysical situations, we drop some of the assumptions underlying Flammang's result, we immediately face considerable uncertainties. For instance, one case, where Flammang's treatment may be of relevance, would be the accretion onto a black hole residing at the centre of a star. It is then quite realistic [8] to consider a possibility, not included in Flammang's treatment, that the rotation of the star might impart enough specific angular momentum to the accreting fluid to significantly change the mode of accretion: While far from the black hole the inflow would still be almost spherically symmetric, at smaller radii there could form, due to the possible presence of a centrifugal barrier, a torus like structure of dense and hot fluid concentrated in the equatorial plane. It is very difficult to estimate the luminosity emitted by such a relatively complex configuration, as well as the accretion rate itself which may now differ from the familiar Bondi rate

$$\dot{M}_{\mathrm{B}} = 4\pi\lambda_s\frac{G^2M^2}{c_s^3}\rho_s. \tag{4.2}$$

Here M is the mass of the black hole, ρ_s is the density of the fluid surrounding the black hole, c_s is the speed of sound, and λ_s is a constant of order unity ($\lambda_s = 1/4$ for $\Gamma = 5/3$).

The possibility that cannot be excluded is that the impeding effect of the centrifugal barrier would reduce the accretion rate relative to $\dot{M}_{\mathrm{B}}$, and, at the same time, through friction within the torus, increase the luminosity over the value (4.1). As it spreads outward through fluid of lower temperature, this luminosity may be too high to be transported by radiation only, thus causing convection.

Convection may be relevant to the spherical accretion from another, more theoretical point of view. As Flammang himself noted [1], his solution, $\hat{L}_o(r)$, entailed a slightly negative specific entropy gradient, $dS/dr < 0$ at large distances from the black hole. According to the Schwarzschild criterion for convection in a *static* fluid, this would imply an instability to convection. Though Flammang was able to conclude that the convection, even if it actually occurs, should not significantly modify his solution, a fuller understanding of convection in this context remains desirable.

A situation, somewhat analogous to convective spherical accretion onto a black hole, has been encountered in the study of the so-called Thorne-Żytkov objects [5, 6], in which the material from a red giant's interior accretes onto its neutron-star core. The relatively small accretion rate in such objects means that the typical convective velocities are much larger than the velocity of radial inflow [6], thus allowing a direct application of the standard mixing length theory (MLT) of convection, which is frequently used in the theory of stellar structure [9].

Despite its simple-mindedness and inevitable crudeness due to the poor state of theoretical understanding of convection, the standard MLT has been remarkably successful: Models of the structure and evolution of the Sun and other stars, which rely heavily on MLT, agree well with the observations and are not sensitive to uncertainties of MLT, such as the value chosen for the mean distance traveled by a convective fluid element before it disintegrates, the so-called mixing length, l_{m}.

In the standard formulation of MLT [9], one assumes that any averaged motion of the stellar material (e.g. due to an evolutionary contraction of the star) is far slower than the convective cells' speeds; and correspondingly there is no coupling between the averaged motion and the convection. As we noted above, this presents no difficulty in the application of the standard MLT to Thorne-Żytkov objects. There are situations, however, when the averaged motion is fast enough that the coupling cannot be ignored. One such situation — the coupling of convection to large amplitude stellar pulsations — has been studied in some detail in the past [8]. In this paper we examine another such situation: the coupling of convection to a steady, radial inflow of stellar matter, i.e. steady spherical accretion.

1.2 Overview

We will develop a simple model of stationary convection in a spherically accreting fluid based on a straightforward extension of the standard MLT. In other words, instead of attempting to found our treatment in the basic hydrodynamic equations we proceed directly from a semi-phenomenological level occupied by convective elements as "elementary particles" of our model — exactly as is done in the standard MLT.

Although we will allow the accretion velocity to be comparable to or even exceed the convective velocity in the mean rest frame of the fluid, we will restrict ourselves to subsonic accretion. This is because a supersonic theory would be far more difficult — and probably is not needed since at supersonic convective velocities the convective elements would presumably be quickly decomposed (through shocks). Thus they cannot travel upstream against a supersonic flow, and they cannot carry energy outward. The energy is presumably trapped in the inflow and the accretion can be approximated as adiabatic [1].

As in the more familiar setting of stellar structure theory, so also in a (subsonic) accreting flow, an excess temperature gradient, or, equivalently, a negative specific entropy gradient, naturally tends to impart buoyancy to convective elements. The elements of smaller entropy and, therefore, higher density will thus tend to fall through the accreting fluid of higher specific entropy and progress more rapidly toward the black hole. Similarly, the hyper-entropic elements will experience a buoyancy force directed upwards. The accretion may, however, sweep both classes of elements toward the black hole.

Of great importance here is the fact that the luminosity may be radius-dependent ($\partial L/\partial r < 0$) in a steady-state accretion flow, even if heat sources such as nuclear burning, are neglected. As we explain in Sec. 2, within the region where convection is present, the luminosity is growing as we approach the black hole ($\partial L/\partial r$ ¡ 0). This causes every fluid element to gain heat as it progresses towards the black hole: simply more heat is received from the fluid below than is released to the fluid above the element. The heavy ("hypoentropic") elements will, due to their faster inward motion, accumulate less heat in this way, after traveling a given distance, than the fluid moving with the mean velocity of accretion. In the opposite case the light ("hyperentropic") elements will accumulate more heat than the surrounding fluid. This enables both classes of elements to sustain their respective density differences with the environment and thus to move relative to it under the influence of buoyancy forces. As we show in Sec. 2 [Eq. (4.35)], the elements from the two classes move symmetrically in the mean reference frame of the accreting fluid, i.e. with velocities of the same magnitude but opposite directions.

There is, however an impediment to convection which we will explore in Sec. 2: The fluid flowing toward the black hole is being stretched in the radial direction ($\partial v/\partial r > 0$, where $v = dr/dt < 0$ is the radial accretion velocity). This effect makes it more difficult for the convective elements to move relative to the mean flow. In the course of their motion, they exchange more heat with the environment due to larger temperature differences needed to produce the requisite buoyancy forces. If the magnitude of the luminosity gradient, $|\partial L/\partial r|$, is not large enough to sustain those temperature differences in the presence of the adverse effect of stretching, the convection will be inhibited. Since $\partial S/\partial r \propto \partial L/\partial r$, this modifies the familiar Schwarzschild criterion for convection, $\partial S/\partial r < 0$, by requiring that $\partial S/\partial r$ be smaller than some (typically small in magnitude) negative quantity proportional to the amount of stretching. Naturally, even when this modified Schwarzschild criterion is satisfied, and convection occurs, the stretching drives the temperature gradients up, as we discuss in Sec. 2.

Having developed in Sec. 2 the basics of our MLT model of convection on the background of an accretion flow, we turn in Sec. 3 to a discussion of some consequences of the model for optically thick accretion onto a black hole. In all cases to be considered, the black hole is sufficiently small that its environment can be assumed homogeneous. In the case of a small black hole located at the centre of a star, this means that we consider only radii that are much smaller than the radius of the star's central region. In addition, since we treat convection only at radii large compared to the so-called accretion radius [6],

$$r_{\mathrm{a}} = \frac{GM}{c_{\mathrm{s}}^2} \tag{4.3}$$

(where c_s is the speed of sound), the pressure scale height, $H_P = -P/(\partial P/\partial r)$, at a given r, will be much larger than r, typically by several orders of magnitude. For that reason we will assume that the mixing length at a given point is always of the order of the distance from the black hole to that point. Thus emerges a picture of concentric convective regions of growing thickness as we move away from the black hole.

Among other issues, we will examine the conclusion of Flammang that the temperature gradient, at least in a gas-pressure dominated environment, is slightly superadiabatic, i.e., that the specific entropy of the accreting fluid increases inward. We will find that even this amount of superadiabaticity actually exceeds our threshold for convection. This inevitably implies that Flammang's solution is convective, though the convective heat flux is still small in comparison to the radiative heat flux. It turns out that Flammang's solution to the combined equations of inflow and convection may be regarded as just the lowest-luminosity member of a class of solutions all of which involve convection. However, the particularly appealing property of Flammang's solution, whose luminosity is virtually constant throughout the convective region, is that the increase in the threshold of convection at smaller radii seems to provide a natural mechanism for extinguishing the convection in the vicinity of the accretion radius. By contrast, in the case of solutions of higher luminosity, most of the heat is transported by convection. Due to a rapid growth in luminosity, as the fluid flows toward the black hole, these solutions' temperature gradients remain safely distant from the convection threshold even at small radii. As we have remarked in the last subsection, this kind of behavior would occur if the conditions at small radii (e.g., high specific angular momentum) lead to higher temperatures and/or higher densities within and around the accretion radius r_{a}. This would preclude a supersonic transition at r_{a}. Instead, the fluid would settle (probably at a rate lower than the Bondi rate) onto the dense and hot inner region, whose description remains outside the scope of this paper.

In Sec. 3 we apply our model to accretion onto a small, primordial black hole of mass $M = 10^{-8} M_{\odot}$ or $M = 10^{-4} M_{\odot}$ residing at the centre of a Sun-like star [3], which, for simplicity, is assumed to consist of pure hydrogen. At the relevant conditions ($T = 1.5 \times 10^{7}\mathrm{K}$, $\rho = 150\ \mathrm{g/cm^3}$), $P_{\mathrm{rad}} = 1.3 \times 10^{14}\mathrm{dyn/cm^2}$ and $P_{\mathrm{gas}} = 3.7 \times 10^{17}\mathrm{dyn/cm^2}$, which implies

$$L_{\mathrm{Fl}} \simeq 2.5 \times 10^{26} \frac{\mathrm{erg}}{\mathrm{sec}} \frac{M}{10^{-8} M_{\odot}} \tag{4.4}$$

[see Eq. (4.1)].

We integrate the equations of structure of the accretion flow inward from the upper boundary of the convective region to $r = 10 r_{\mathrm{a}}$, where [see Eq. (4.3)]

$$r_{\mathrm{a}} = 3.2 \times 10^{2} \mathrm{cm} \frac{M}{10^{-8} M_{\odot}}. \tag{4.5}$$

Thus, as we remarked above, in addition to avoiding the near-sonic region of accretion where any MLT is bound to break down, we leave open the question of inner boundary conditions, which may depend strongly on the parameters of the innermost portion of the flow.

The conditions at smaller radii might also influence the accretion rate, as we noted above. Thus we will study accretion for three different accretion rates: $\dot{M} = 0.01\dot{M}_{\rm B}$, $\dot{M} = 0.1\dot{M}_{\rm B}$ and $\dot{M} = \dot{M}_{\rm B}$, where

$$\dot{M}_{\rm B} = \frac{M_\odot}{50{\rm sec}}\left(\frac{M}{M_\odot}\right)^2 = 4\times10^{15}\frac{\rm g}{\rm s}\left(\frac{M}{10^{-8}M_\odot}\right)^2 \tag{4.6}$$

is the Bondi accretion rate [see Eq. (5.1)]. The given range of accretion rates will allow us to observe a continuous transition from a convection very close to that described by the standard MLT, where accretion is too slow to have any effect on convection, over to a convection very strongly influenced by the presence of accretion.

In Chapter 5 of this thesis we will use our modified MLT formalism for convection, and these convective accretion models to analyze the evolution of a small black hole at the centre of a Sun-like star, and the structure of the accretion flow onto it.

2 Heat transfer and convection in an accreting fluid

2.1 Heat transfer and pressure balance

The basic equation of heat transfer [11] in the local rest frame of the fluid, with entropy sources (e.g., viscosity or nuclear reactions) neglected, is

$$\rho T\frac{dS}{dt} = -\nabla\cdot\mathbf{q}, \tag{4.7}$$

where S is the entropy per unit mass. This equation involves the heat flux $\mathbf{q}$ regardless of the mechanism of heat transfer — whether it is photon diffusion, electron conduction, or convection. In our convective situation we have in mind a somewhat artificial picture of large-scale fluid elements exchanging heat by, among other means, trading packets of fluid with extra high or low (depending on the direction of motion) entropy content. Of course, in order for convection to occur, the Schwarzschild criterion involving entropy and pressure gradients has to be satisfied. As we shall see the Schwarzschild criterion, though with some modifications, retains its importance in a spherically accreting fluid.

In the spherically symmetric ($\mathbf{q} = F\mathbf{e}_r$) and stationary (zero time derivatives) flow, Eq. (4.7) can be rewritten as

$$\rho T v \frac{\partial S}{\partial r} = -\frac{1}{4\pi r^2}\frac{\partial L}{\partial r}, \tag{4.8}$$

or as

$$\dot{M} T \frac{\partial S}{\partial r} = \frac{\partial L}{\partial r}, \tag{4.9}$$

where $L = 4\pi r^2 F$ is, again, the total (radiative and convective) luminosity *measured in the rest frame of the fluid* and v ($v < 0$) is the radial velocity of accretion.

Using the total differential of specific entropy

$$\begin{aligned} dS &= \left[\left(\frac{\partial S}{\partial T}\right)_P \frac{dT}{dP} + \left(\frac{\partial S}{\partial P}\right)_T\right] dP \\ &= c_P(\nabla - \nabla_{\mathrm{ad}})\frac{dP}{P}, \end{aligned} \tag{4.10}$$

where c_P is the isobaric heat capacity per unit mass, and denoting by $\nabla_{\mathrm{ad}} \equiv (\partial \ln T/\partial \ln P)_{\mathrm{ad}}$ the adiabatic temperature gradient and by $\nabla \equiv \partial \ln T/\partial \ln P$ the actual temperature gradient in the fluid, Eq. (4.9) leads to

$$\nabla - \nabla_{\mathrm{ad}} = -\frac{H_P}{\dot{M} c_P T}\frac{\partial}{\partial r} L. \tag{4.11}$$

Here $H_P \equiv -P/(\partial P/\partial r)$ is the pressure scale height.

In the convective regime fluid elements of density differing from the average density of their surroundings move relative to the mean rest frame of the fluid under the influence of the buoyancy force. However, since we assume the accretion flow stationary, we will find it occasionally convenient to consider the motion of the convective elements in the rest frame of the black hole — the frame in which all quantities associated with the bulk flow change only with radius r.

The total force per unit mass acting on a fluid element of density ρ_e and moving with velocity v_e is then

$$\begin{aligned} \frac{dv_e}{dt} = f &= -\frac{G\mathcal{M}}{r^2} - \frac{1}{\rho_e}\frac{\partial P}{\partial r} \\ &= -\frac{G\mathcal{M}}{r^2} - \frac{1}{\rho_e}\left(-\frac{G\mathcal{M}}{r^2}\rho - v\frac{\partial v}{\partial r}\rho\right) \\ &\simeq -\frac{\Delta\rho}{\rho}\bar{g} + \frac{dv}{dt}, \end{aligned} \tag{4.12}$$

where $\Delta\rho = \rho_e - \rho$, and $\mathcal{M}$ is the total mass enclosed within radius r – including the mass of the black hole. We have denoted by d/dt the time derivatives comoving with the convective element on the left-hand side, and with the mean flow on the right-hand side of Eq. (4.12):

$$\frac{d}{dt}v_e \equiv \left(\frac{\partial}{\partial t} + v_e\frac{\partial}{\partial r}\right) v_e, \qquad \frac{d}{dt}v \equiv \left(\frac{\partial}{\partial t} + v\frac{\partial}{\partial r}\right) v. \tag{4.13}$$

In Eq. (4.12) we have also introduced the "effective" gravity $\bar{g} \equiv G\mathcal{M}/r^2 + dv/dt$ which in the case of stationary accretion (stationary mean flow) is simply $\bar{g} = G\mathcal{M}/r^2 + v(\partial v/\partial r)$. Thus the motion relative to the general accelerated (term $v\partial v/\partial r$) flow of the surrounding fluid is due to to the density difference $\Delta\rho$. We can therefore identify the first term on the right-hand side of the last of Eqs. (4.12) as the buoyancy force. We see that if the density $\Delta\rho$ difference can be sustained, convection will inevitably follow. The density difference itself critically depends on the details of the dynamics of convective elements and the heat exchange between them and the surrounding fluid.

2.2 Motion of convective elements through the surrounding fluid

The heat exchange between a convective element and its environment can be approximately treated as consisting of two components. The first component, or, as we will call it, the "horizontal heat exchange," is due to the temperature difference ΔT between the element and the horizontally surrounding fluid. The second component is the "vertical heat exchange" with the fluid just above and below the convective element; it results if the luminosity L changes with radius — as can be expected in an accreting fluid even without any energy sources or sinks [see Eq. (4.11)]. This vertical exchange occurs even for fluid elements whose temperature is equal to the temperature of the horizontal layer in which they reside. It is simply due to the fact that the amount of heat being received by the element from below need not equal the amount of heat released to the upper levels. For simplicity we assume that this exchange does not depend on the element's motion through the surrounding fluid. The vertical contribution can then be written as

$$\left(\frac{dS}{dt}\right)_{\mathrm{v}} = -\frac{1}{\rho T}\nabla \cdot \mathrm{q} = -\frac{1}{4\pi r^2 \rho T}\frac{\partial}{\partial r}L. \tag{4.14}$$

The total rate of change of the entropy per unit mass in the convective element is, then,

$$\left(\frac{dS}{dt}\right)_{\mathrm{e}} = \left(\frac{dS}{dt}\right)_{\mathrm{v}} + \left(\frac{dS}{dt}\right)_{\mathrm{h}}$$

$$= -\frac{1}{4\pi r^2 \rho T}\frac{\partial}{\partial r}L - \frac{\Lambda}{\rho V T}. \tag{4.15}$$

In the above expression we have introduced the convective element's volume V and the "horizontal" heat flux Λ through its surface, which for a roughly spherical element of diameter d and surface area Σ can be written approximately as

$$\Lambda = \frac{8acT^3}{3\kappa\rho}\Delta T\frac{\Sigma}{d}. \tag{4.16}$$

Using Eq. (4.10), $d/dt \equiv v_e d/dr$ along the trajectory of the element, and the definition of pressure scale height, we can derive

$$\nabla_e - \nabla_{\rm ad} = -\frac{v}{v_e}\frac{H_P}{\dot{M}c_P T}\frac{\partial}{\partial r}L + \frac{H_P}{\rho V c_P v_e T}\Lambda, \tag{4.17}$$

where we have introduced the "convective element" temperature gradient $\nabla_e \equiv (\partial \ln T/\partial \ln P)_e$ which describes the change of temperature in the element as it moves through the layers of different pressure, and relative to the accreting fluid. In Eq. (4.17) we have actually averaged over all upgoing (or all downgoing) convective elements passing through a stationary (fixed r) referent surface instead of treating them individually — in the same way it is done in the standard MLT [9]. Similarly, in omitting the partial time derivative from the expression for the acceleration of the convective elements (4.13), we have in fact assumed that the pattern of convection, emerging as a result of the averaging in a *stationary* accretion flow, is itself stationary.

Following approximations familiar from the mixing-length theory, we assume that convective fluid elements traverse on average the mixing length $l_{\rm m}$ *in the mean rest frame of the fluid.* From now on we will denote by a subscript $+$ $(-)$ quantities corresponding to convective elements moving "upward" ("downward") in this reference frame. Thus the "upward" moving elements may either move away from the black hole ($v_+ > 0$) or actually approach it due to advection by the accretion flow ($v_+ < 0$, yet $v_+ - v > 0$).

We now return to an individual (i.e., *not averaged*) fluid element and examine its motion. We denote by x the radial distance that this fluid element has traveled relative to the mean fluid motion, under the destabilizing action of its buoyancy, since the moment it was created in near equilibrium with its surroundings. Similarly, we will denote by $r_\pm$ the distance of the element from the black hole. Because the element's velocity relative to the fluid's mean local rest frame is $v_\pm - v = dx/dt$, while its velocity relative to the black hole is $v_\pm = dr_\pm/dt$,

$$dr_\pm = \frac{v_\pm}{v_\pm - v}dx. \tag{4.18}$$

Using this relation, we can rewrite the fluid element's equation of motion (4.12) as

$$\begin{aligned}
-\frac{\Delta\rho_\pm}{\rho}\bar{g} &= v_\pm\frac{d}{dr_\pm}v_\pm - v\frac{d}{dr_\pm}v \\
&= v_\pm\frac{d}{dr_\pm}(v_\pm - v) + (v_\pm - v)\frac{dv}{dr_\pm} \\
&= \frac{1}{2}\frac{d}{dx}(v_\pm - v)^2 + (v_\pm - v)\frac{\partial v}{\partial r}. \qquad (4.19)
\end{aligned}$$

In Eq. (4.19) we have taken advantage of the fact that the mean flow is stationary to write

$$\frac{d}{dr_\pm}v \equiv \frac{1}{v_\pm}\left(\frac{\partial}{\partial t} + v_\pm\frac{\partial}{\partial r}\right)v = \frac{\partial}{\partial r}v. \qquad (4.20)$$

The second term in the last line of Eq. (4.19) has the form of a "frictional braking" whose origin is not difficult to explain: The radial separation Δr between any pair of points comoving with the mean flow of the fluid ($|v| \propto 1/r^2$ typically, so $dv/dr > 0$) is increased as they approach the black hole ($\Delta r \propto 1/r^3$). This radial stretching effectively decelerates the convective elements relative to the surrounding fluid, thus counteracting the buoyancy force. This is analogous to an ant crawling on the surface of an expanding balloon, or to the cosmological "redshifting" of the velocity of a cosmic-ray proton, as it moves through the expanding universe.

We now seek to integrate Eq. (4.19) in an averaged sense (averaged over all upgoing or downgoing elements). In doing so, we estimate that the average buoyancy force, that has acted on the upgoing (or downgoing) fluid elements now passing through some referent surface, is one half the buoyancy force they are now experiencing at that surface. Since they have traveled, on average a distance $l_{\mathrm{m}}/2$ (in the fluid's frame), the portion of the specific "work" of the buoyancy force available for the elements' acceleration is, again on average,

$$\frac{1}{2}\int_0^{\pm l_{\mathrm{m}}/2}\left(-\frac{\Delta\rho_\pm}{\rho}\bar{g}\right)dx \approx \frac{1}{2}\left(-\frac{1}{2}\frac{\Delta\rho_\pm}{\rho}\bar{g}\right)\left(\pm\frac{l_{\mathrm{m}}}{2}\right), \qquad (4.21)$$

where we assumed that half the buoyancy "work" was spent on "pushing" the surrounding fluid aside. The numerical factors appearing in Eq. (4.23) are somewhat arbitrary — they were introduced in order to conform to the standard mixing-length theory [9].

Similarly, we approximate the effect of the radial stretching of the accreting fluid by

$$\int_0^{\pm l_{\mathrm{m}}/2}(v_\pm - v)\frac{dv}{dr}dx \approx \left(\frac{v_\pm - v}{2}\right)\frac{dv}{dr}\left(\pm\frac{l_{\mathrm{m}}}{2}\right). \qquad (4.22)$$

Equation (4.19) then gives the following relation between the approximate speed of convective elements relative to the surrounding fluid, and the average density difference $\Delta\rho_\pm$:

$$\frac{1}{2}(v_\pm - v)^2 \approx \mp\frac{1}{8}\frac{\Delta\rho_\pm}{\rho}\bar{g}l_{\mathrm{m}} \mp \frac{1}{4}l_{\mathrm{m}}\frac{dv}{dr}(v_\pm - v). \tag{4.23}$$

The convective elements' average displacement $\Delta r_\pm$ in the frame of the black hole, as they traverse the mixing length l_{m} in the fluid's frame, is [see Eq. (4.18)]

$$\Delta r_\pm = v_\pm \frac{l_{\mathrm{m}}}{|v_\pm - v|} = \pm l_{\mathrm{m}}\frac{v_\pm}{v_\pm - v}. \tag{4.24}$$

Thus, the temperature difference between the elements, which started their convective motion from an average distance $\Delta r_\pm/2$ below (above) the referent surface, and their environment is

$$\begin{aligned} \Delta T_\pm \equiv T_\pm - T &= \frac{\Delta r_\pm}{2}\frac{1}{H_P}(\nabla - \nabla_\pm)T \\ &= \pm\frac{l_{\mathrm{m}}}{2H_P}\left(\frac{v_\pm}{v_\pm - v}\right)(\nabla - \nabla_\pm)T, \end{aligned} \tag{4.25}$$

where $\nabla_\pm \equiv (\partial \ln T/\partial \ln P)_\pm$ are averaged temperature gradients carried by convective elements as they move across layers of different pressure. The temperature difference, Eq. (4.25), leads to a density difference

$$\begin{aligned} \Delta\rho_\pm \equiv \rho_\pm - \rho &= -\delta\rho\frac{\Delta T_\pm}{T} \\ &= \mp\frac{\delta l_{\mathrm{m}}}{2H_P}\left(\frac{v_\pm}{v_\pm - v}\right)(\nabla - \nabla_\pm)\rho. \end{aligned} \tag{4.26}$$

In the above equation we have used $\delta \equiv -(\partial \ln \rho/\partial \ln T)_P$ and assumed the equality of pressure in the elements and the environment due to all relevant speeds being subsonic.

Finally, using Eq. (4.26) we obtain from Eq. (4.23) an equation for the velocities of convective elements

$$(v_\pm - v)^3 \pm \frac{1}{2}l_{\mathrm{m}}\frac{dv}{dr}(v_\pm - v)^2 = v_\pm w^2(\nabla - \nabla_\pm), \tag{4.27}$$

where we have introduced a new quantity of the dimension of velocity

$$w \equiv \left(\frac{\delta\bar{g}l_{\mathrm{m}}^2}{8H_P}\right)^{1/2} \approx \frac{v_{\mathrm{ff}}^2}{c_{\mathrm{s}}}. \tag{4.28}$$

In the last equation we denoted by $v_{\rm ff} \equiv (2\bar{g} l_{\rm m})^{1/2}$ the velocity that would be acquired by a particle freely falling through a height $l_{\rm m}$ in a gravitational field of strength $\bar{g}$. Note that if $H_P < r$, we can assume, as is usually done in the theory of stellar structure [9], that $l_{\rm m} \approx H_P$. In this case $w \approx c_{\rm s}$.

Defining

$$Z \equiv \frac{|v|}{w}, \quad t_\pm \equiv \frac{v_\pm}{w}, \quad \Psi \equiv \frac{1}{2}\frac{l_{\rm m}}{w}\frac{dv}{dr}, \tag{4.29}$$

we can conveniently rewrite Eq. (4.27) as

$$(t_\pm + Z)^3 \pm \Psi (t_\pm + Z)^2 = t_\pm (\nabla - \nabla_\pm). \tag{4.30}$$

Adopting the convention $l_{\rm m}\Sigma/Vd = (9/2)/l_{\rm m}$ from the standard mixing length theory [9], using Eqs. (4.16), (4.25) and (4.28), and defining

$$U \equiv \frac{3acT^3}{\kappa \rho^2 c_P l_{\rm m}^2 \bar{g}} \left(\frac{8P}{\delta\rho}\right)^{1/2}, \tag{4.31}$$

it is straightforward to rewrite Eq. (4.17) as

$$\nabla_\pm - \nabla + X = \frac{v}{v_\pm} X \pm 2Uw \frac{\nabla - \nabla_\pm}{v_\pm - v}, \tag{4.32}$$

where we have used a new dimensionless quantity

$$X \equiv \nabla - \nabla_{\rm ad}. \tag{4.33}$$

We recall that the second term on the right-hand side of Eq. (4.32) stands for the averaged "horizontal" heat exchange due to the temperature difference between the upgoing (downgoing) convective elements and their surroundings. This heat exchange is proportional to the dimensionless parameter U, which is roughly equal [9] to the ratio $(H_P/\bar{g})^{1/2}/\tau_{\rm adj}$ of the free fall time through the height H_P, and the "adjustment" time $\tau_{\rm adj} = |\rho l_{\rm m}^3 c_P \Delta T_\pm / \Lambda|$ [see Eq. (4.16)] over which an element's temperature would approach that of the environment. For instance, in the case of "efficient" convection ($U \ll 1$), the elements tend to exchange very little heat horizontally with the environment until they are disrupted after traveling an average distance $l_{\rm m} < H_P$.

With the help of Eqs. (4.27)–(4.30), we can rewrite Eq. (4.32) as

$$(t_\pm + Z)^3 \pm (2U + \Psi)(t_\pm + Z)^2 - (X - 2U\Psi)(t_\pm + Z) = 0. \tag{4.34}$$

Equation (4.34), being a cubic in the unknown $t_\pm$, has three solutions. The following two solutions are physically acceptable,

$$t_\pm = -Z \mp \left(U + \frac{\Psi}{2}\right) \pm \left[\left(U + \frac{1}{2}\Psi\right)^2 + X - 2U\Psi\right]^{1/2}, \tag{4.35}$$

$$t_{\pm} = -Z; \tag{4.36}$$

The third solution (the same as (4.35) but with the last $\pm$ substituted by a $\mp$) is physically unacceptable because it says that the "+" solution is downgoing and the "−" solution is upgoing, contrary to their definitions. The acceptable solution (4.36) corresponds to elements moving together with the average flow (an unstable situation according to the Schwarzschild criterion), while the solution (4.35) represents convective elements moving symmetrically in opposite directions in the mean rest frame of the fluid.

Since for the elements moving upward (downward) with respect to the fluid we must have $t_+ + Z > 0$ ($t_- + Z < 0$), the convective solution (4.35) is physically unacceptable when $X < 2U\Psi$, thus leaving the equilibrium $t_{\pm} + Z = 0$ as the only acceptable solution. This tells us that, in the presence of our accelerating flow, the Schwarzschild criterion for convective instability, which normally takes the form $X \equiv \nabla - \nabla_{\mathrm{ad}} > 0$ gets modified to $X > 2U\Psi$. This happens because, as we pointed out earlier, the radial "stretching" of the inflowing fluid effectively reduces the action of the buoyancy forces. Equivalently, the larger element-environment temperature difference necessary to produce a given magnitude of convective speeds, $v_{\pm} - v$, will lead to a more rapid cooling of the upward moving elements or heating of the downward moving ones.

Let us discuss this in greater detail: Consider, for concreteness, the downward moving elements. Due to their higher velocity of radial inflow they are heated less rapidly by the changing luminosity than the surrounding fluid. Since this heating deficit is proportional to X [see, e.g., Eq. (4.32)], we obtain that, in order to keep these elements cooler than the environment, X needs to exceed $2U\Psi$. Thus for $0 < X < 2U\Psi$, although the Schwarzschild criterion is satisfied, the too rapid temperature equalization between the elements and the environment inhibits convection.

Of course, since the numerical factors we adopted in Eqs. (4.21) and (4.22) are somewhat arbitrary, the factor 2 in our condition $X > 2U\Psi$ for convection is only approximate. We will see in the next section that the presence of Ψ in the criterion for convection is unlikely to be of importance in the case of efficient convection ($U \ll 1$), or/and for a very subsonic flow [$r \gg r_{\mathrm{a}}$, see Eq. (4.3)]. The latter case constitutes the proper domain of the applicability of our model.

2.3 Equations of flow in the convective regime

In order to determine the basic quantities describing convection, X and $t_\pm$, we need to supplement Eq. (4.34) with an equation expressing the convective transport of energy. The convective heat flux in the mean rest frame of the fluid (moving with velocity v) is

$$F_{\rm c} = \rho_-(v_- - v)c_P\Delta T_- + \rho_+(v_+ - v)c_P\Delta T_+, \tag{4.37}$$

where $\rho_\pm/\rho$ are the fractions of the fluid participating in "upward" or "downward" convective motions. Assuming that all of the fluid is included in convection ($\rho_+ + \rho_- = \rho$), and bearing in mind that, due to the symmetry of solutions (4.35), $\rho_+ = \rho_-$ in order to conserve the total mass flux $\dot{M} = -4\pi\rho r^2 v$, we conclude $\rho_+ = \rho_- = \rho/2$.

Using Eqs. (4.25), (4.29) and (4.30), the convective flux (4.37) can be rewritten as

$$F_{\rm c} = \frac{\rho}{2}c_P w T\frac{l_{\rm m}}{2H_P}\frac{1}{2}\Big[(t_+ + Z)^3 + \Psi(t_+ + Z)^2 - (t_- + Z)^3 + \Psi(t_- + Z)^2\Big]. \tag{4.38}$$

Since the total heat flux is the sum of the radiative and convective fluxes

$$F = F_{\rm r} + F_{\rm c}, \tag{4.39}$$

where F is proportional to the so-called radiative temperature gradient $\nabla_{\rm r}$

$$F = \frac{L}{4\pi r^2} \equiv \frac{4}{3}\frac{ca}{\kappa\rho}\frac{T^4}{H_P}\nabla_{\rm r}, \tag{4.40}$$

and

$$F_{\rm r} = \frac{4}{3}\frac{ca}{\kappa\rho}\frac{T^4}{H_P}\nabla, \tag{4.41}$$

Eq. (4.38) can be rewritten as

$$\begin{aligned} \frac{8}{9}U(W - X) \;=\; & \left[\left[\left(U + \frac{1}{2}\Psi\right)^2 + X - 2U\Psi\right]^{1/2} - U - \frac{1}{2}\Psi\right]^3 \\ & +\Psi\left[\left[\left(U + \frac{1}{2}\Psi\right)^2 + X - 2U\Psi\right]^{1/2} - U - \frac{1}{2}\Psi\right]^2, \end{aligned} \tag{4.42}$$

where we have introduced $W \equiv \nabla_{\rm r} - \nabla$ and used Eqs. (4.28), (4.31) and (4.35).

If $\Psi = 0$, Eq. (4.42) is identical to that for X in the standard MLT [9]. Indeed, together with Eq. (4.35), it shows that, within the framework of our model, convection can be thought of as nothing but a "Galilean boost" of the standard MLT picture into the local *accelerated* rest frame of the inflowing fluid. The inclusion of $\Psi \neq 0$ then only accounts for the fact that the local velocity of the inflowing fluid is not homogeneous ($\partial v/\partial r \neq 0$).

For sufficiently small U ($U \ll X^{1/2}$ *and* $U \ll \Psi$), the right-hand side of Eq. (4.42) can be considerably simplified

$$\frac{8}{9}U(W-X) = \left[\left(\frac{1}{4}\Psi^2 + X\right)^{1/2} - \frac{1}{2}\Psi\right] X. \tag{4.43}$$

The effect of the "stretching" of the inflowing fluid is now quite transparent: The presence of Ψ reduces the amount of luminosity that can be transported by convection [proportional to the right-hand side of Eq. (4.43)] at given X — just as we would expect on the basis of our discussion in the last subsection of the effect of radial stretching on convection.

In order to determine the structure of the convective region, we need, in addition to Eq. (4.42), equations describing the variation of the total mass $\mathcal{M}$, pressure, temperature, accretion speed and luminosity with r. While giving the necessary derivations in the Appendix, here we only present those equations:

$$\begin{aligned}
\frac{\partial \mathcal{M}}{\partial r} &= 4\pi \rho r^2, \\
\frac{\partial P}{\partial r} &= -\frac{G\mathcal{M}\rho}{r^2}\frac{1-2rv^2/G\mathcal{M}}{1-(\alpha-\delta\nabla)\rho v^2/P}, \\
\frac{\partial T}{\partial r} &= -\nabla\frac{T}{P}\frac{dP}{dr}, \\
\frac{\partial L}{\partial r} &= \dot{M} c_P T X \frac{1}{P}\frac{\partial P}{\partial r},
\end{aligned} \tag{4.44}$$

where we have introduced $\alpha \equiv (\partial \ln \rho/\partial \ln P)_T$. Note that the second and third of Eqs. (4.44) as well as Eq. (4.42), are coupled in a seemingly complicated way due to the presence of $\nabla \equiv \nabla_{\rm ad} + X$, the definition of W, and the related Eq. (4.40). Moreover, in order to find Ψ, which is also used in Eq. (4.42), we need to compute

$$\frac{\partial v}{\partial r} = v\left(-\alpha\frac{1}{P}\frac{\partial P}{\partial r} + \delta\frac{1}{T}\frac{\partial T}{\partial r} - \frac{2}{r}\right) \tag{4.45}$$

(see Appendix for derivation). However, since we are limited to subsonic flow ($v^2 \ll P/\rho$), this coupling is very weak. In a numerical solution of Eqs. (4.44), for instance, only one or two iterations, starting from an essentially arbitrary initial X in the second equation of the set, yield a highly accurate solution for X.

3 The structure of the convective region

As we have noted in connection with Eq. (4.35), within the framework of our model X must be larger than $2U\Psi$ in order to drive convection. Because the radiative gradient ∇_{r} is always greater than the actual gradient ∇ ($W > X$), the condition $X > 2U\Psi$ implies $W > 2U\Psi$. Since in our treatment of convection we are naturally limited to (very) subsonic accretion velocities, Ψ is likely to be a small number at the upper boundary of the convection region. Indeed, at very subsonic accretion velocities ($v/c_{\mathrm{s}} \ll 1$, or, equivalently, $r/r_{\mathrm{a}} \gg 1$), where $H_P \gg r$ and thus the density gradient $\partial\rho/\partial r$ can be ignored, $r(dv/dr) \simeq -2v$, and thus $\Psi \simeq Z(l_{\mathrm{m}}/r) \lesssim Z$. As we mentioned in the Introduction, in this region we can reasonably estimate the mixing length l_{m} to be of the order of r. Defining $\eta = l_{\mathrm{m}}/r \lesssim 1$ and using Eqs. (4.3) and (4.28) we obtain

$$w \approx \frac{G\mathcal{M}}{r}\eta\left(\frac{\rho}{8P}\right)^{1/2} \sim \eta c_{\mathrm{s}}\frac{r_{\mathrm{a}}}{r}. \tag{4.46}$$

Since the accretion velocity is

$$|v| = \frac{\dot{M}}{4\pi\rho r^2}, \tag{4.47}$$

Eqs. (4.29) and (4.46) imply

$$\Psi = \frac{\dot{M}}{4\pi G\rho\mathcal{M}}\left(\frac{8P}{\delta\rho}\right)^{1/2}\frac{1}{r}. \tag{4.48}$$

Under the same assumptions, U can be computed from Eq. (4.31)

$$\begin{aligned} U &= \frac{3acT^3}{Gc_P\eta^2\kappa\rho^2\mathcal{M}}\left(\frac{8P}{\delta\rho}\right)^{1/2} \\ &= 4.8\times10^{-5}\left(\frac{0.7}{\eta}\right)^2\left(\frac{1.1}{\kappa}\right)\frac{\bar{T}^{7/2}}{\bar{\rho}^2}\frac{1}{M_{-8}}\frac{M}{\mathcal{M}}, \end{aligned} \tag{4.49}$$

where we have expressed the temperature and density in units of their values at the centre of the Sun: $\bar{T} = T/T_\odot = T/1.5\times10^7\mathrm{K}$, $\bar{\rho} = \rho/\rho_\odot = \rho/150\mathrm{g/cm}^3$. The mass of the black hole, M_{-8}, is given in units $10^{-8}M_\odot$. We have also approximated the opacity κ with a sum of electron scattering and Rosseland mean bremsstrahlung (free-free) opacities

$$\kappa \simeq \kappa_{\mathrm{es}} + \kappa_{\mathrm{bs}}, \tag{4.50}$$

where

$$\kappa_{\mathrm{bs}} = 6.4\times10^{22}\rho T^{-7/2}\ \mathrm{cm/g}. \tag{4.51}$$

The value of this opacity is $\kappa \simeq 1.1 \mathrm{cm}^2/g$ for the conditions at the centre of the Sun. The opacity in Eq. (4.49) is assumed to be in units cm^2/g.

From Eq. (4.48) we can, then, obtain the threshold of convection

$$\begin{aligned} X_{\mathrm{c}} = 2U\Psi &= \frac{12ac}{\pi G^2 \delta \eta^2 c_P} \frac{\dot{M} P T^3}{\kappa \rho^4 \mathcal{M}^2} \frac{1}{r} = \\ &= 6.6 \times 10^{-5} \left(\frac{0.7}{\eta}\right)^2 \left(\frac{1.1}{\kappa}\right) \frac{\bar{T}_o^{7/2}}{\bar{\rho}_o^2} \frac{1}{M_{-8}} \left(\frac{M}{\mathcal{M}}\right)^2 \frac{r_{\mathrm{a}}}{r}, \end{aligned} \tag{4.52}$$

where we have used the Bondi accretion rate (4.6) as well as its dependence on the density and temperature of the environment in the case of a gas-pressure-dominated fluid, $\dot{M}_{\mathrm{B}} \propto M\rho/T^{3/2}$. As should be obvious from Eq. (4.52), the typically small value of X_{c} in the upper part of the convection zone, where $r \gg r_{\mathrm{a}}$, implies only a tiny modification of the Schwarzschild criterion for the onset of convection.

The value of X_{c} is, however, important in another context. Assuming purely radiative heat transfer, Flammang [1] found that the equations for the structure of a spherically symmetric accretion flow implied the existence of only one solution for luminosity, $\hat{L}_o(r)$, for a given mass of the black hole and environmental density and temperature. This result can be understood for subsonic velocities ($r \gg r_{\mathrm{a}}$) with the aid of our Eqs. (4.44):

Since we are, for the moment, ignoring the possibility of convection, $X = W$ and $F = F_{\mathrm{r}}$ [see Eqs. (4.40) and (4.41)], the last of Eqs. (4.44) can be written as

$$\frac{d}{dr} L = k_{\mathrm{r}}(L - L_{\mathrm{s}}), \tag{4.53}$$

where L_{s} is the luminosity that would be obtained in the case of an adiabatic temperature gradient, or, equivalently, at constant specific entropy S, and where

$$L_s = \frac{16\pi G c a \mathcal{M}}{3\kappa} \frac{T^4}{P} \nabla_{\mathrm{ad}}, \tag{4.54}$$

and

$$\begin{aligned} k_{\mathrm{r}} &= -\frac{3}{16\pi} \frac{\dot{M} c_P \kappa \rho}{c a T^3} \frac{1}{r^2} \\ &= -6.5 \times 10^4 \left(\frac{\kappa}{1.1}\right) \frac{\bar{\rho}^2}{\bar{T}^{7/2}} \frac{r_a}{r^2}. \end{aligned} \tag{4.55}$$

The typically large negative value of k_r implies a very "stiff" [12] quasi-exponential behavior of the luminosity. Namely, a small deviation from a certain stable solution, $\hat{L}_o(r)$ of Eq. (4.53), will lead to an exponential divergence (as we integrate inward) from $\hat{L}_o(r)$ with the e-folding distance k_r^{-1}. To prevent this divergence, $\hat{L}_o(r)$ has to closely follow L_s. This is most simply expressed in terms of the excess temperature gradient $X \equiv \nabla - \nabla_\mathrm{ad} = \nabla_\mathrm{r} - \nabla_\mathrm{ad}$. Since $L = L_s(\nabla_\mathrm{ad} + X)/\nabla_\mathrm{ad}$, we can rewrite Eq. (4.53) for $r \gg r_\mathrm{a}$ as

$$\frac{r}{\nabla_\mathrm{ad}}\frac{\partial X}{\partial r} + \left(1 + \frac{X}{\nabla_\mathrm{ad}}\right)\frac{r}{L_S}\frac{\partial L_S}{\partial r} = -\frac{3c_P\kappa\dot{M}\rho}{16\pi caT^3}\frac{X}{r}, \tag{4.56}$$

or as

$$\begin{aligned}\frac{r}{\nabla_\mathrm{ad}}\frac{\partial X}{\partial r} &= -\frac{3c_P\kappa\dot{M}\rho}{16\pi caT^3}\frac{1}{r}X + \left(1 + \frac{X}{\nabla_\mathrm{ad}}\right)\frac{G\mathcal{M}\rho}{Pr} \times \\ &\quad \times \left[4\nabla - 1 + \frac{\kappa - \kappa_\mathrm{es}}{\kappa}\left(\frac{9}{2}\nabla - 1\right) - 4\pi\frac{Pr^4}{G\mathcal{M}^2}\right].\end{aligned} \tag{4.57}$$

We see from Eq. (4.57) that, except for a narrow interval near

$$\begin{aligned} r_o &= \left(\frac{G\mathcal{M}^2}{4\pi P}\right)^{1/4}\left[4\nabla_\mathrm{ad} - 1 + \frac{\kappa - \kappa_\mathrm{es}}{\kappa}\left(\frac{9}{2}\nabla - 1\right)\right]^{1/4} \\ &\simeq 4.8 \times 10^3 r_\mathrm{a}\frac{1}{M_{-8}^{1/2}}\frac{\bar{T}^{3/4}}{\bar{\rho}^{1/4}}\left(\frac{3}{5} + \frac{\kappa - \kappa_\mathrm{es}}{\kappa}\frac{4}{5}\right)^{1/4}, \end{aligned} \tag{4.58}$$

($\nabla_\mathrm{ad} = 2/5$ for a gas-pressure-dominated fluid) at which the second term on the right-hand side of Eq. (4.57) changes sign, we can neglect the derivative term in (4.57) to obtain an approximate solution

$$\begin{aligned}\hat{X}_o(r) &= \frac{16\pi Gca}{3c_P}\frac{T^3\mathcal{M}}{\kappa P\dot{M}}\nabla_\mathrm{ad}\left[4\nabla - 1 + \frac{\kappa - \kappa_\mathrm{es}}{\kappa}\left(\frac{9}{2}\nabla - 1\right) - 4\pi\frac{Pr^4}{G\mathcal{M}^2}\right] \\ &\simeq 1.0 \times 10^{-5}\left(\frac{1.1}{\kappa}\right)\frac{\bar{T}_o^{7/2}}{\bar{\rho}_o^2}\frac{1}{M_{-8}}\frac{\mathcal{M}}{M}\left[\frac{3}{5} + \frac{\kappa - \kappa_\mathrm{es}}{\kappa}\frac{4}{5}\right. \\ &\qquad \left. -1.9 \times 10^{-15}M_{-8}^2\left(\frac{M}{\mathcal{M}}\right)^2\left(\frac{r}{r_\mathrm{a}}\right)^4\right],\end{aligned} \tag{4.59}$$

and the corresponding luminosity $\hat{L}(r) = (1 + \hat{X}_o/\nabla_\mathrm{ad})L_s(r)$. The small positive value of $\hat{X}_o$ at $r < r_o$ stems from the growth of temperature as the fluid approaches the black hole. In conjunction with the resulting fall in opacity, this will increase the luminosity L_S that can be transported by radiation at $\nabla = \nabla_{\mathrm{ad}}$. Since the actual luminosity has to follow this growth of L_S, this implies that even if, as we have assumed, convection doesn't occur, the temperature gradient is (slightly) super-adiabatic: The fluid receives some heat as it flows toward the black hole.

Comparing, now, Eqs. (4.52) and (4.59), we observe that $\hat{X}_o(r)$ and $X_c(r)$ are comparable in the vicinity of r_a regardless of the values of T, ρ and M_{-8}. However, the r_a/r dependence of $X_c(r)$ makes it smaller than $\hat{X}(r)$ for $10r_a < r < r_o$, thus necessarily implying convection in this region.

Let us now examine the effects of convection. The increase in L_S, as we go inward, will, as in the case of non-convective accretion discussed by Flammang, lead to the existence of a solution $L_o(r) \simeq \hat{L}_o(r) \simeq L_S(r)$ for which $X_o \simeq \hat{X}_o$ is just sufficient to enable the luminosity to follow L_S. However, the rate of deviation of nearby solutions from L_o will be much smaller than for non-convective accretion. Specifically, since $X_o \gg X_c$ for $10r_a < r < r_o$, we can, for the case of "efficient" convection, $U \ll X^{1/2}$, solve Eq. (4.42) to obtain

$$X = \left(\frac{8}{9}UW\right)^{2/3}. \tag{4.60}$$

Then, using the last of Eqs. (4.44), we can derive

$$\begin{aligned}\frac{\partial}{\partial r}(L - L_o) &= \dot{M}c_P T\frac{1}{P}\frac{\partial P}{\partial r}(X - X_o) \\ &\simeq \dot{M}c_P T\frac{1}{P}\frac{\partial P}{\partial r}X_o\frac{2}{3}\frac{W - W_o}{W_o} \\ &= \frac{16}{27}\frac{U}{X_o^{1/2}}k_r(L - L_o),\end{aligned} \tag{4.61}$$

where $W_o = 9X_o^{3/2}/8U$. From Eqs. (4.49), (4.55) and (4.59) we can compute the rate of deviation of L from L_o in the convective region $r < r_o$

$$\begin{aligned}\frac{r}{L - L_o}\frac{\partial}{\partial r}(L - L_o) = rk_c &= r\frac{16}{27}\frac{U}{X_o^{1/2}}k_r \\ &= -5.8 \times 10^2\left(\frac{0.7}{\eta}\right)^2\left(\frac{\kappa}{1.1}\right)^{1/2}\frac{\bar{\rho}_o^2}{\bar{T}^{7/2}}M_{-8}^{1/2}\frac{r_a}{r} \\ &\qquad \times\left(\frac{3}{5} + \frac{\kappa - \kappa_{\mathrm{es}}}{\kappa}\frac{4}{5}\right)^{-1/2}.\end{aligned} \tag{4.62}$$

We see that, despite the reduction in the deviation rate brought about by convection, the rate is still relatively high at sufficiently small radii unless $M_{-8} < 0.1$. For this reason the solution $X_o(r)$ retains some of the significance it had in the non-convective model of accretion: Should X fall below X_o, as we approach the black hole, it will proceed, with the e-folding distance $k_{\rm c}^{-1}$ towards $X_{\rm c}$. Upon crossing $X_{\rm c}(r)$ the convection will end, and the fall of X will accelerate and then continue with the much smaller e-folding distance $k_{\rm r}^{-1}$. This fall will rapidly annihilate the luminosity L. Quite obviously, these solutions must be considered un-physical. In the opposite case, $X > X_o$, the solutions will rapidly move towards higher luminosities and higher X. However, in contrast with the unphysical solutions for $X < X_o$, this growth will be inhibited to some extent by the presence of convection for all radii $10r_{\rm a} < r < r_o$.

We illustrate the above analysis by the accretion onto a small black hole of mass $M_{-8} = 1$ which resides at the centre of a Sun-like star ($\rho = 150 \mathrm{g/cm^3}$, $T = 1.5 \times 10^7$K). In Fig. 4.1 we show the behavior of the luminosity L, convective velocities $v_\pm$, and gradient differences, W and X, for various solutions of Eqs. (4.44).

As we explained above, between $X_o \simeq \hat{X}_o$ (dotted line in Fig. 4.1) and $X_{\rm c}$ (dashed line) for $r < r_o$ lies the region of unphysical convective solutions. Noteworthy is also the sustained fall of relative convective velocities, $|v_\pm - v|$ with respect to the accretion velocity $|v|$, for the "lowest luminosity" physical solution $X_o(r)$. This was to be expected, since, due to the (approximate) constancy of X_o, $W_o = 9X_o^{3/2}/8U$ and L_o for $r < r_o$, Eq. (4.38) implies $|t_\pm + Z| \propto r^{-1/3}$ for $X \gg X_{\rm c}$, and thus $|v_\pm - v| = w|t_\pm + Z| \propto r^{-4/3}$ [see Eq. (4.46)], while $|v| \propto r^{-2}$.

The upward shift of the upper boundary of the convective region, $r_{\rm c}$, relative to r_o (solid X curve relative to dotted), requires, however, some explanation. In the convective regime, relatively small changes in the excess gradient $X \equiv \nabla - \nabla_{\rm ad}$ may result in much larger changes in $W = 9X^{3/2}/8U$ ($X \gg X_{\rm c}$), as can be seen in connection with Eqs. (4.61) and (4.62). Analogously to Eq. (4.56) we can derive, using $L = L_S(1 + W/\nabla_{\rm ad})$, an equation for X in the convective case

$$\left(\frac{27}{16}\frac{X^{1/2}}{U}\right)\frac{r}{\nabla_{\rm ad}}\frac{\partial X}{\partial r} + \frac{r}{L_S}\frac{\partial L_S}{\partial r} + \frac{1}{\nabla_{\rm ad}}\frac{9}{8U}X^{3/2}\left(\frac{r}{L_S}\frac{\partial L_S}{\partial r} - \frac{r}{U}\frac{\partial U}{\partial r}\right) = -\frac{3c_P\kappa\dot{M}\rho}{16\pi caT^3}\frac{X}{r}. \tag{4.63}$$

The third term on the left-hand side of Eq. (4.63) is proportional to a small quantity $W = 9X^{3/2}/8U$ and can be neglected in comparison with the second term on the same side. As we move outward across r_o, the second term changes its

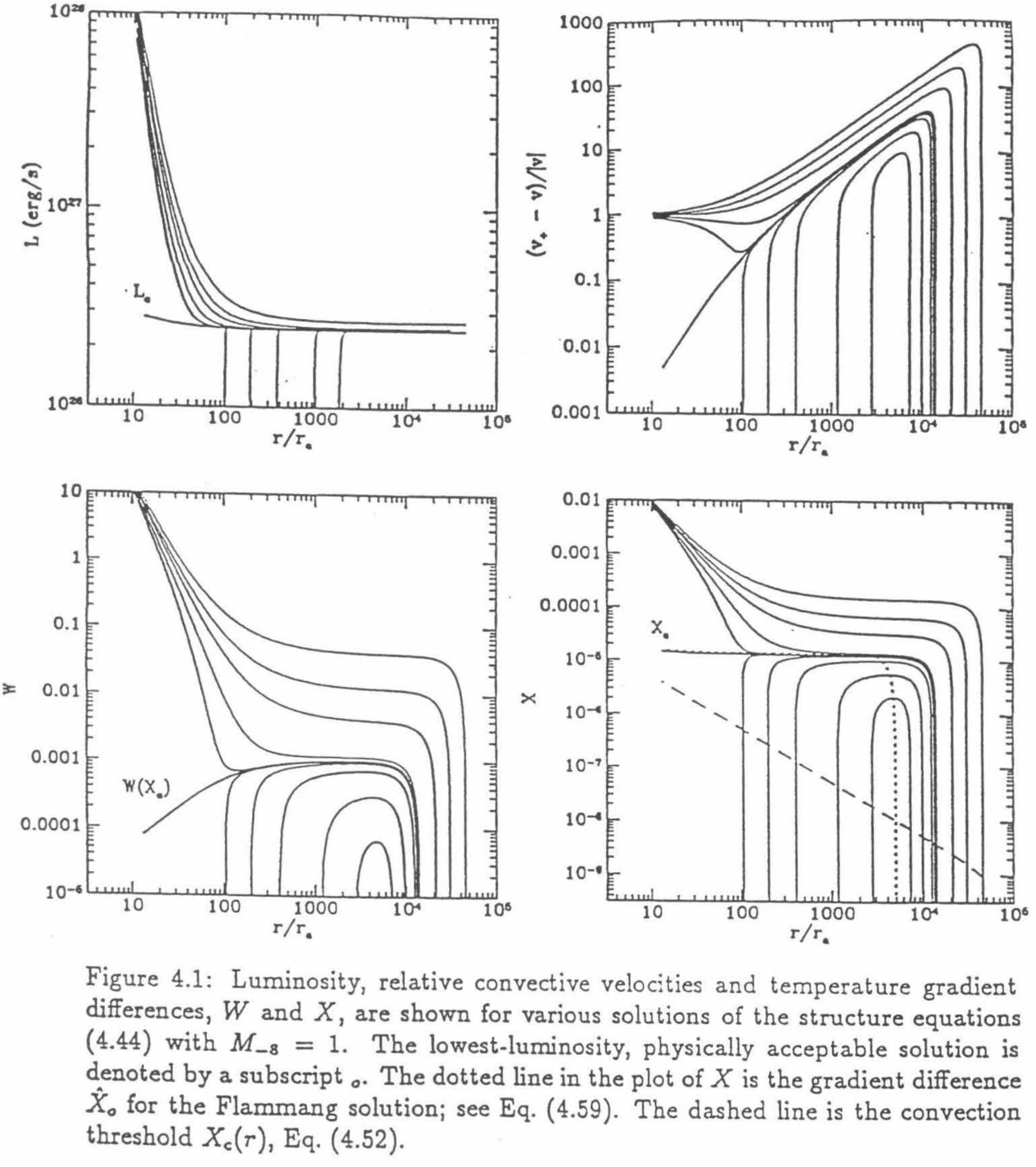

Figure 4.1: Luminosity, relative convective velocities and temperature gradient differences, W and X, are shown for various solutions of the structure equations (4.44) with $M_{-8} = 1$. The lowest-luminosity, physically acceptable solution is denoted by a subscript $_o$. The dotted line in the plot of X is the gradient difference $\hat{X}_o$ for the Flammang solution; see Eq. (4.59). The dashed line is the convection threshold $X_c(r)$, Eq. (4.52).

sign from negative to positive. However, in order for X to change appreciably $[-(r/X)\partial X/\partial r \sim 1]$, the first term on the left-hand side needs to reach some (negative) value whose magnitude increases with growing $\bar{X}$, the value of X at $r < r_o$. This is achieved roughly at r_c which can be estimated from

$$\begin{aligned}\frac{27}{16}\frac{\bar{X}^{3/2}}{\nabla_{\rm ad}U} &\approx \frac{r_c}{L_S}\frac{\partial L_S}{\partial r} + \frac{3c_P\kappa\dot{M}\rho}{16\pi caT^3}\frac{X}{r_c} \\ &\approx \frac{4\pi\rho}{\mathcal{M}}\frac{r_c^4 - r_o^4}{r_c} + \frac{3c_P\kappa\dot{M}\rho}{16\pi caT^3}\frac{X}{r_c},\end{aligned} \tag{4.64}$$

where we have used the expression for $\partial L_S/\partial r$ appearing in Eq. (4.57). Solving Eq. (4.64) for the case shown in Fig. 4.1, with $\bar{X} \approx X_o \approx 10^{-5}$, one obtains $r_c \approx 2r_o \approx 10^5 r_a$, in reasonable agreement with the exact numerical solution displayed in Fig. 4.1. Thus, the convection effectively "smears" the effect of a sudden drop in $\hat{X}_o$ at r_o. This effect may, actually, be inferred directly by comparing Eqs. (4.56) (non-convective model) and (4.63) (convective model): In the case of efficient convection, $U^2 \ll X$, the derivative term in the convective case is "weighted" by a relatively large factor $X^{1/2}/U$ which is absent from the non-convective model. This circumstance, together with the relatively small rates of deviation of the un-physical solutions ($X < X_o$) from X_o at $r \lesssim r_o$ (see Eq. (4.62)), gives a certain limited "lease on life" to these solutions on both sides of r_o, with the range of radii, over which such a solution can exist, increasing with growing $\bar{X}$ (see Fig. 4.1). Ultimately, when $\bar{X}$ reaches X_o, this range extends up to r_c and all the way down to the vicinity of r_a.

Once we have gone beyond r_c, the upper boundary of the convection zone, toward larger radii, the relatively rapid fall of X_o stops, approximately at $\hat{X}_o(r_c) < 0$, and then the solution proceeds along the Flammang-type non-convective curve $\hat{X}_o(r)$. A similar conclusion holds for solutions with $X(r) > X_o(r)$, or, equivalently, $L(r) > L_o(r)$, for which the radius at which they merge into the Flammang-type solution is naturally shifted upwards as we can see in Fig. 4.1.

If the luminosity L is sufficiently larger than L_o, we can compute straightforwardly the radius of the upper boundary of the convection zone. Specifically, if the luminosity at $r \gg r_a$ is $L = (1+\zeta)L_{\rm Fl}$, the radiative gradient will be

$$\nabla_{\rm r} = \frac{3}{16\pi acG}\frac{\kappa LP}{\mathcal{M}T^4} = \nabla_{\rm ad}\frac{1+\zeta}{1+\mu(r/r_a)^3}, \tag{4.65}$$

where we have taken into account that the accreting fluid may contribute significantly to the mass enclosed within the given radius, $\mathcal{M} \simeq M + 4\pi\rho_o r^3/3$, and have introduced the dimensionless parameter μ

$$\mu = \frac{4\pi \rho_o r_{\rm a}^3}{3M} = 1.1 \times 10^{-15} M_{-8}^2. \tag{4.66}$$

The upper boundary of the convection zone will then lie at $r_{\rm c}$, where

$$\frac{r_{\rm c}}{r_{\rm a}} = \left(\frac{\zeta_{\rm c}}{\mu}\right)^{1/3} = 0.97 \times 10^5 \frac{\zeta_{\rm c}^{1/3}}{M_{-8}^{2/3}}, \tag{4.67}$$

and $\zeta_{\rm c}$ is the value of ζ at $r_{\rm c}$.

In Fig. 4.2 we further illustrate the influence of accretion on the structure of the vicinity of the black hole. We choose a relatively high value $\zeta_{\rm c} = 1$ (so the luminosity is twice Flammang at the outer edge of the convection zone), and show the solutions for $M_{-8} = 10^4$ and for three values of the accretion rate: $\dot{M} = 0.01\dot{M}_{\rm B}$, $0.1\dot{M}_{\rm B}$, and $1.0\dot{M}_{\rm B}$ as indicated on the figure. As we have noted in the Introduction, such departures of the accretion rate from the Bondi value (5.1) are not implausible: The conditions at and inside $r_{\rm a}$, such as the presence of a relatively high specific angular momentum in the fluid, and the resulting formation of an accretion torus that pushes back against the flow, may hinder the inward flow and thus reduce the accretion rate below $\dot{M}_{\rm B}$. The flow at larger radii could well remain virtually spherically symmetric and thus amenable to the foregoing analysis. Naturally, in the limit $\dot{M} = 0$ one obtains constant $(dL/dr = 0)$ luminosity and a W which changes very slowly for intermediate radii because $\nabla_{\rm r} \propto L/\mathcal{M}$, and $\mathcal{M}$ varies little inside $r_M(M) = (3M/4\pi\rho_o)^{1/3} = 210\, r_{\rm a}(M/10^{-4}M_\odot)^2$. Note also that, not surprisingly, at larger accretion rates ($\dot{M} \approx \dot{M}_{\rm B}$) both the "downgoing" and "upgoing" elements are swept by the accretion towards the black hole ($v_+ - v < -v$) throughout the convective region. This behavior should be contrasted with the case of a smaller black hole ($M_{-8} = 1$), discussed above, where only the solutions with very low luminosities had the accretion velocity exceeding the convective velocities at small radii — an obvious consequence of the fact that the characteristic accretion rate $\dot{M}_{\rm B} \propto M^2$ grows faster with mass than the characteristic luminosity $L_{\rm Fl} \propto M$.

Finally, for completeness, we show in Fig. 4.3 the profiles of $\mathcal{M}$, ρ and P, again for $M_{-8} = 10^4$. These quantities are virtually independent on the accretion rate. Thus, pressure balance is only slightly affected by the accretion since $\bar{g} - G\mathcal{M}/r^2 \approx (v/v_{\rm ff})^2 G\mathcal{M}/r^2 \propto (r_{\rm a}/r)^3 G\mathcal{M}/r^2$, where $v_{\rm ff} \equiv (G\mathcal{M}/r)^{1/2}$ is the "free fall" speed. Similarly, since $X \ll 1$ in all cases considered, ∇ is almost the same as $\nabla_{\rm ad}$ thus determining the temperature profile independently of the accretion rate.

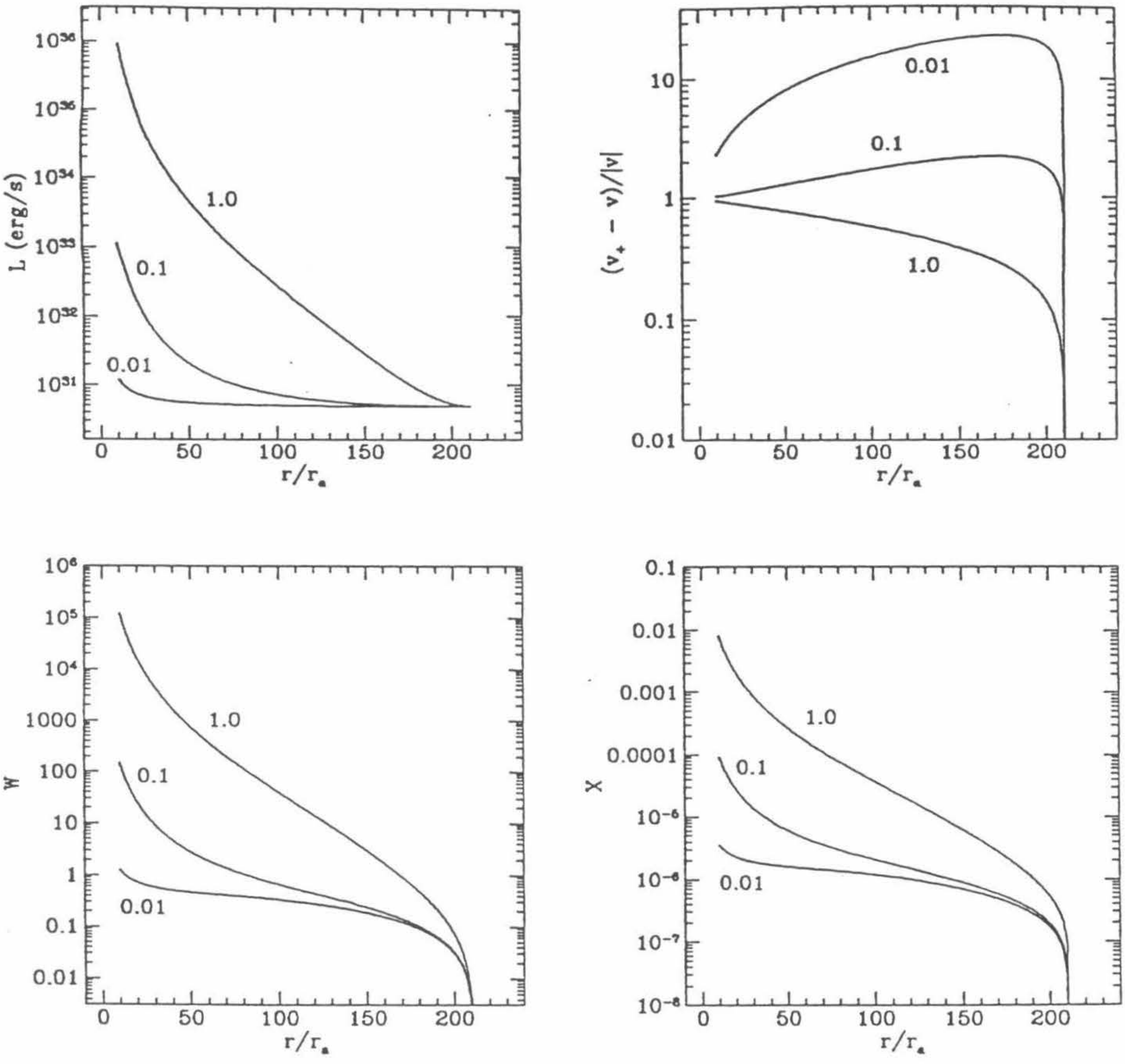

Figure 4.2: Quantities strongly dependent on the accretion rate — the luminosity L, W, $(v_+ - v)/|v| = -(v_- - v)/|v|$ and X — are shown for three different accretion rates. The numbers next to the curves indicate these accretion rates in units of the Bondi rate $\dot{M}_{\rm B}$. In all three cases we assume $L = 2L_{\rm Fl}$ at the upper boundary of the convection region.

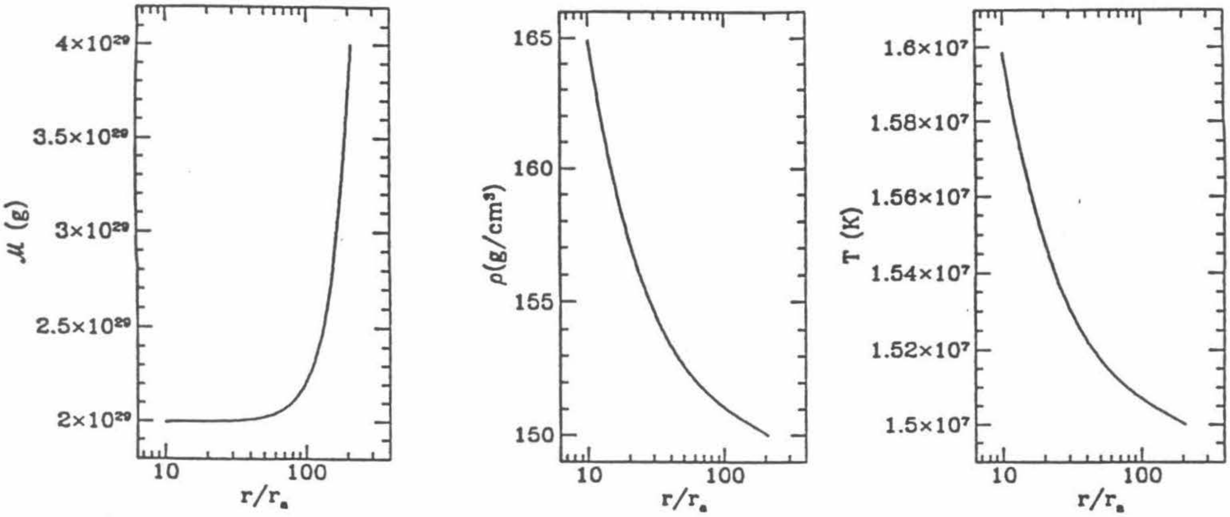

Figure 4.3: Quantities weakly dependent on the accretion rate — Mass $\mathcal{M}$, density ρ and temperature T — are shown as functions of r for $L = 2L_{\rm Fl}$. Although three different accretion rates were used as in Fig. 4.2, the differences in $\mathcal{M}$, ρ and T are invisibly small.

4 Conclusion

The modified MLT approach to convection in spherically symmetric accretion flows, that we have developed in Sec. 2, and the insights we have gained from specific examples in Sec. 3, are used in Chapter 5 of this thesis as an important tool for deducing the evolution of a small black hole inside a Solar-type star.

Acknowledgments

The author wishes to thank Garrett Biehle and Peter Goldreich for very useful discussions regarding this research and related topics. In particular, the author thanks Kip Thorne for patient support and invaluable insights provided during the course of this research. This paper was supported in part by NSF grant AST-9114925.

Appendix: Derivation of the equations of structure

The first and third of Eqs. (4.44) need no special explanation. The second equation can be obtained easily if we note that

$$\begin{aligned} \frac{\partial|v|}{\partial r} &= \frac{\partial}{\partial r}\left(\frac{\dot{M}}{4\pi\rho r^2}\right) \\ &= -\frac{\dot{M}}{2\pi\rho^3} - \frac{\dot{M}}{4\pi\rho r^2}\frac{\partial}{\partial r}\ln\rho \\ &= -|v|\left(\frac{2}{r} + \alpha\frac{1}{P}\frac{\partial P}{\partial r} - \delta\frac{1}{T}\frac{\partial T}{\partial r}\right), \end{aligned} \tag{4.68}$$

where we have used

$$\begin{aligned} \frac{\partial\ln\rho}{\partial\ln r} &= \left(\frac{\partial\ln\rho}{\partial\ln P}\right)_T\frac{\partial\ln P}{\partial\ln r} + \left(\frac{\partial\ln\rho}{\partial\ln T}\right)_P\left(\frac{\partial\ln T}{\partial\ln P}\right)\frac{\partial\ln P}{\partial\ln r} \\ &\equiv (\alpha - \delta\nabla)\frac{\partial\ln P}{\partial\ln r}. \end{aligned} \tag{4.69}$$

With the aid of Eq. (4.68) we can easily solve

$$\frac{\partial P}{\partial r} = -\rho v\frac{\partial v}{\partial r} - \frac{G\mathcal{M}\rho}{r^2}, \tag{4.70}$$

for $\partial P/\partial r$ and thus arrive at the second of Eqs. (4.44). The fourth of Eqs. (4.44) is nothing but a rewrite of expression (4.11).

Bibliography

[1] See R.A. Flammang, Mon. Not. R. astron. Soc. **199**, 833 (1982) and references therein.

[2] K.S. Thorne, R.A. Flammang and A.N. Żytkow MNRAS **194**, 475 (1981).

[3] R.A. Flammang, MNRAS **206**, 589 (1984).

[4] See Chapter 5 of this thesis.

[5] K.S. Thorne and A.N. Żytkov, Ap. J., **212**, 832 (1977).

[6] G. Biehle, Ap. J., **380**, 167 (1991).

[7] R. Kippenhahn and A. Weigert, *Stellar Structure and Evolution* (Springer-Verlag, Berlin, 1990); J.P. Cox, R.T. Giuli, Principles of Stellar Structure, Vol.I (Gordon and Breach, New York, 1968), B. Paczyński, Acta Astr. **19, 1** (1969).

[8] For a recent review of the role of convection in stellar pulsations, see the articles in D. Gough and J. Toomre, *Challenges to Theories of the Structure of moderate-Mass Stars* (Springer-Verlag, Berlin, 1991).

[9] S. Hawking, Mon. Not. R. Astron. Soc., **152**, 75 (1971).

[10] J. Frank, A. King and D. Raine, *Accretion Power in Astrophysics* (Cambridge University Press, Cambridge, U.K., 1992).

[11] L.D. Landau and E.M. Lifshitz, *Fluid Mechanics* (Pergamon Press, Oxford, U.K., 1987).

[12] For more treatment of the concept of "stiff" differential equations, see C.W. Gear, *Numerical Initial Value Problems in Ordinary Differential Equations* (Prentice Hall, Englewood Cliffs, N.J., 1971); R.C. Aiken, *Stiff Computation* (Oxford University Press, Oxford, U.K., 1985); E. Hairer, S.P.

Norsett, G. Wanner, *Solving Ordinary Differential Equations, Vol. II: Stiff and Differential-Algebraic Problems* (Springer-Verlag, Berlin, 1987).

Chapter 5

Evolution of a primordial black hole inside a rotating solar-type star

Abstract

We investigate the accretion-driven evolution of a primordial black hole at the center of the Sun or any other solar-type star. We show that if the star's rotation is small enough for the accretion to be radial, then the black hole grows at the rather fast "Bondi" rate [so the remaining life of the star is $50(M_\odot/M)$s when the hole's mass is M], and the flow produces luminosity at the rather low "Flammang" level [$L_{\rm Fl} = 2.5 \times 10^{34}(M/M_\odot)$ erg/s]. As a result, the growing hole has no influence on the star's external appearance until tens of minutes before it completely destroys the star. We then examine the effects of a solar-like rotation. If each fluid element were to retain its angular momentum during the inflow, the accretion would centrifugally hang up and form an "accretion torus" near the growing hole, until the hole's mass M reaches $M_+ = 10^{-3}M_\odot$; thereafter the inflow would be radial. We show that, when $M < M_{\rm v} \equiv 10^{-11}M_\odot$, then molecular viscosity removes angular momentum from the flow fast enough to prevent such an accretion torus from forming; and when $M < M_B \equiv 6 \times 10^{-8} {B_o}^{3/4} M_\odot$, where B_o is the magnetic field strength at the star's center, then magnetic torques prevent the torus from forming; and in these regimes the flow remains radial at the high Bondi rate, and the luminosity remains at the low Flammang level. For M above these regimes but below $M_+ = 10^{-3}M_\odot$, an accretion torus probably does form and may increase the luminosity L above Flammang and slow the flow $\dot{M}$ below Bondi. However, until at most three days before the star is destroyed, the increase of L cannot be by more than about an order of magnitude because the higher L would produce strong convection outside the accretion torus and the resulting turbulent viscosity would remove so much angular momentum from the flow as to prevent the torus from forming in the first place. Furthermore, if the accretion rate is reduced to less than about 20% of the Bondi rate, the rotation does not change the final conclusion: The black hole has no significant influence on the external appearance of the star until tens of minutes before the star is destroyed. If, on the other hand, the accretion rate somehow remains approximately Bondi, the luminosity and the total energy output of the accretion could, in principle, grow large enough to cause observable changes in the star, but not earlier than the last two or three days before the end of the accretion. As a corollary, the "solar neutrino problem" cannot be solved by postulating a small black hole at the Sun's center.

1 Introduction and summary

Over the past two decades the discrepancy between the observed and theoretically predicted solar neutrino rates [1, 2] has given a healthy stimulus to a great variety of speculative attempts to solve the so-called "Solar Neutrino Problem." Proposed explanations at one extreme are based on modifications of the standard solar model through precarious alterations in the temperature and/or chemical content of the Sun's core. Explanations at the other extreme are based on the fundamental particle physics of neutrinos; these, especially the Mikheev-Smirnov-Wolfenstein theory of neutrino flavor mixing, have gained popularity recently due to improvements in empirical understanding [2].

Exotic as they might seem, these models' boldness is exceeded by Hawking's early proposal [3] that accretion onto a black hole residing inside the Sun could substitute to some extent the energy produced by conventional nuclear reactions. Since the energy flux due to accretion would be accompanied by few neutrinos, it might seem straightforward to produce both the photon and neutrino fluxes as they are currently observed [4].

However, the expected progressive increase in the mass of the black hole and in the hole's accretion rate immediately posed the problem of the time-scale over which the accretion could provide the necessary luminosity. In their model of Solar evolution involving a central black hole, Clayton *et al.* [5] assumed (without justification on the basis of any models) that the accretion rate $\dot{M}$ was directly proportional to the luminosity L, for whose value they simply adopted the Eddington luminosity. These assumptions lead to an exponential growth of the mass of the black hole. The authors concluded that if the accretion provided a significant fraction of the observed luminosity at some moment, the star would ultimately be eaten up by the black hole in a time $\Delta t = 0.1 t_{\rm age}(f/0.1)$, where $t_{\rm age}$ is the present age of the Sun and $f \equiv L/\dot{M}c^2$ is the efficiency of accretion, which was assumed (without proof) to be constant. Thus although we would indeed live in an untypical era, a relatively short time before the end of the Sun, there would still be enough time to, say, develop sufficient technology and move to another hospitable, this time hopefully black-hole free, solar system.

This conclusion is, alas, brought into question by a more careful examination of the assumptions regarding the accretion luminosity. Specifically, for a black hole mass M larger than about 10^{21} grams, the accretion radius [6] $r_a \simeq GM/c_s^2$ will be larger than the mean free path $l_p = 1/\kappa\rho_s$ of a photon. (Here $c_s = 6 \times 10^7$cm/s is the speed of sound in pure, completely ionized hydrogen at 1.5×10^7K, $\kappa \simeq 1.1\mathrm{cm}^2/\mathrm{gram}$ is the opacity, and $\rho_s = 150\mathrm{g/cm}^3$ is the central density of the Sun.)

In this mass range, *if the Sun's rotation is negligible*, we should be able to treat the accretion in the first approximation as everywhere adiabatic and radial with the familiar Bondi accretion rate [6]

$$\dot{M} = 4\pi\lambda_s \frac{G^2M^2}{a_s^3}\rho_s = C_0M^2 = \frac{M_\odot}{50\mathrm{s}}\left(\frac{M}{M_\odot}\right)^2 \tag{5.1}$$

(where λ_s is a numerical constant of order unity, equal to 1/4 for the adiabatic exponent $\Gamma = 5/3$), which leads to a remaining lifetime for the Sun

$$t_{\mathrm{life}} = 50\mathrm{s}(M_\odot/M), \tag{5.2}$$

when the black hole's mass has reached the value M. Moreover, as Flammang has shown [7], the radial flow and large optical thickness at the accretion radius lead to a unique luminosity emitted by the accreting fluid,

$$L_{\mathrm{Fl}} = 4\nabla_{\mathrm{ad}}\frac{P_{\mathrm{rad}}}{P_{\mathrm{gas}}}\frac{4\pi GMc}{\kappa} \approx 2.5 \times 10^{34}\frac{\mathrm{erg}}{\mathrm{s}}\frac{M}{M_\odot}, \tag{5.3}$$

where $P_{\mathrm{rad}} = 1.5 \times 10^{14}\mathrm{dyn/cm}^2$ and $P_{\mathrm{gas}} = 3.7 \times 10^{17}\mathrm{dyn/cm}^2$ are the radiation and gas pressure corresponding to the above mentioned values of the temperature and density; $\nabla_{\mathrm{ad}} \equiv (\partial \ln T/\partial \ln P)_S = (\Gamma - 1)/\Gamma$ is the adiabatic "temperature gradient" [8, 9]. It is easy to see that L_{Fl} is the luminosity that "leaks out" from the accreting fluid whose temperature gradient is almost exactly at its adiabatic value.

A straightforward conclusion can now be drawn from Eqs. (5.1)-(5.3): If the present day accretion luminosity is a detectable portion (say 1 percent) of the total solar luminosity (and if the Sun's rotation is negligible), there remain only about 10 hours until the final throes of the dying Sun. Moreover, the accretion luminosity has been this high only during the past day—far too short for the accretion-induced photons to diffuse out to the solar surface. Correspondingly, we cannot know that the Sun has a black hole at its center until hydrodynamic effects from the final, catastrophic accretion reach the Sun's surface—presumably tens of minutes before the Sun's death. The apparent conflict of this result with naked eye observations hardly seems to be compensated by the remote possibility of a briefly reduced neutrino flux.

One would, thus, be lead to reject the black hole inside the Sun as a cure for the solar neutrino problem.

This simple picture might, however, be changed significantly due to the rotation of the Sun (or any other solar-type star)—as Martin Rees has pointed out to us. Although the Sun may be considered a relatively slowly rotating star with the period of about 25 days at its surface and about 15 days in its core, the fluid flowing from large radii toward the black hole could have enough specific angular momentum to get hung up at the corresponding Kepler radius before reaching the black hole. Thus, at least until the growth of the black hole makes the last stable orbit radius exceed the Kepler radius of the inflowing fluid (which happens when $M = M_{+} \simeq 10^{-3} M_{\odot}$), there is a possibility that a torus-like structure, supported by the angular momentum, could form near the black hole and produce a luminosity larger than the Flammang luminosity. Therefore, the above-described analysis and conclusions, regarding the evolution of a black hole inside the Sun, would be valid, strictly speaking, only for very slowly rotating solar-type stars.

In order to get centrifugally hung-up, the inflowing fluid needs to retain a substantial portion of its original angular momentum. For that reason, this paper is, in large part, devoted to an analysis of various mechanisms of transferring angular momentum from the fluid at small radii to a more distant environment (i.e., of "braking the rotation"), and to the limits these mechanisms could impose on the formation of an accretion torus and on the luminosity produced by any such torus. In our treatment we will focus attention on the region around the equatorial plane where the influence of the rotation is strongest, and will assume that the angular momentum is transferred only within this region. In other words, we will ignore the exchange of angular momentum between the near-equatorial region and the fluid closer to the axis of rotation. Such exchange, occurring, for instance, through meridional circulation [10], presumably would only weaken the effects of rotation on the accretion. For that reason our treatment will underestimate to some extent the rotation-braking effect of all of the mechanisms examined.

Since the accretion rate increases with the growing mass of the black hole, the time over which the braking of the differential rotation can act is ever shorter as the hole grows larger and the fluid is increasingly able to retain its angular momentum. This will put an upper limit on the mass of the black hole, above which a given braking mechanism loses its effectiveness. Thus we will conclude in Sec. 3 that (for the parameters characteristic of the center of the Sun) braking by molecular viscosity is capable of removing the centrifugal obstacle to radial inflow only for $M < M_{\rm v} = 10^{-11} M_{\odot}$. On the other hand, as we shall see in Sec. 4, the mass limit M_B for effective braking by magnetic torques depends on the strength of the initial "seed" field B_0 in the Sun's core, which is amplified by the differential rotation. Though one might presume that the braking effect would be limited by reconnection of the field lines and subsequent ohmic dissipation, an analysis in Sec. 4 shows that for $B_0 > 5$ Gauss the mass limit $M_B = 6 \times 10^{-8} M_\odot (B_0/\mathrm{Gauss})^{3/4}$ is determined not by reconnection but by the limited amplification of the magnetic field due to an insufficient amount of winding of the field lines at the given accretion rate $\dot{M} = \dot{M}_B$. If $B_0 < 10^5$Gauss, there will be a range of black hole masses $M_B < M < M_+$ over which magnetic braking is incapable of preventing an accretion torus from forming.

In this mass range we see no way to prevent a torus from forming. If the torus is to be of any interest for the external appearance of the Sun, it must increase the accretion's luminosity well above the Flammang level and/or reduce the inflow rate well below the Bondi level. A detailed analysis of the torus's actual structure and luminosity is beyond the scope of this paper—and turns out to be almost unnecessary. Instead, in Sec. 5, we investigate the question of whether, in the region of radial flow outside the torus, a substantially increased luminosity and/or reduced inflow rate is compatible with a flow which carries enough angular momentum to form the torus in the first place. The answer is "No," because of luminosity-induced convection: Based on a mixing-length theory of convection in a spherically accreting fluid developed in Chapter 4 of this thesis, we estimate that luminosities exceeding the Flammang level $L_{\mathrm{Fl}}(M)$ by a factor of a few would produce strong convection, and the resulting turbulent viscosity would remove angular momentum from the inflowing fluid so efficiently as to prevent the torus from forming. There is a possible exception: When $M \sim 0.1 M_+$ the luminosity required to prevent the torus formation could exceed the L_{Fl} by two or or more orders of magnitude if $\dot{M} \simeq \dot{M}_B$. If $\dot{M}$ is significantly reduced from the Bondi value ($\dot{M} \lesssim 0.2 \dot{M}_{\mathrm{B}}$), this increase in luminosity is not large enough to cause observable energy release during the short time (at most three days) before the black hole reaches the limit M_+ and reverts to spherically symmetric accretion with the accompanying Flammang luminosity. Therefore, in the probable case of sub-Bondi accretion rates, the Sun or any other solar-type star will show no surface signs of the cancerous black hole at its center until (presumably) tens of minutes before the hole destroys the star. Only then, with hydrodynamic effects from the final catastrophic accretion reaching the star's surface, will external observers learn of the hole.

If the accretion rate persists at about the Bondi level, the luminosity as the hole passes through the range $M \sim (0.1 \text{ to } 1) M_+$ might be large enough to lead to observable effects — but only during the last two or three days before the final collapse of the star.

In our analysis we have ignored the fact that the flow down the polar axis of the Sun would not be hindered by a centrifugal barrier. However, due to the formation of a torus, one would expect the radiative flux to be preferentially emitted along the axis, and thus to push (to some extent) the fluid back. This is closely related to a possible caveat in our discussion: Since we are not analyzing the detailed structure of the innermost region where the torus should form, we are not able to exclude the (however unlikely) possibility that a very large luminosity could be directed almost entirely along the axis of rotation. Although this pattern of heat transfer could, in principle, produce visible effects on the star's surface, it might still not cause a significant convection in the equatorial plane, and thus our heat generator would be left without an effective negative feedback. However, due to the high density and opacity of the fluid near the centre of the Sun, it seems implausible that the high anisotropy of the flux could extend to distances large enough ($r \gg r_{\mathrm{a}}$) to affect our basic conclusions.

Apart from this remote possibility, our analyses, leading to the conclusions outlined in this Introduction, are rather crude, since the detailed effects of rotation, magnetic fields, and convection on the flow are probably quite complex. However, our arguments appear to be quite robust, and thus our conclusions fairly secure.

Our analysis can be easily extended to any star similar to the Sun, but with possibly somewhat different parameters. However, for simplicity, in this paper we will restrict ourselves to the solar parameters—including, for example, the rotation rate of the Sun's core (period 15 days).

2 The role of the Sun's rotation

At first sight, the rotation of the Sun might seem too slow (we assume angular velocity of $\Omega_0 = 2\pi/15\text{days} = 5 \times 10^{-6}\text{sec}^{-1}$ at the center of the Sun), to be of any consequence for the accretion onto a small black hole. However, consider a fluid element, close to the equatorial plane, which at the beginning of accretion happens to be at distance r_o from the black hole. If the inflowing gas conserves its angular momentum, the rotation will still provide this element with enough specific angular momentum $l = \Omega_0 r_0^2$ to stall its inflow near the corresponding

Kepler radius $r_k = r_0^4\Omega_0^2/MG$ which can be re-expressed as

$$\frac{r_k}{r_a} = 2.7 \times 10^{-7}\left(\frac{M_\odot}{M}\right)^{2/3}, \tag{5.4}$$

for the conditions at the center of the Sun. In Eq. (5.4) we have taken into account that by the time the initially distant fluid element approaches the center, the black hole mass will have grown approximately to

$$M = 4\pi r_0^3 \rho_0/3. \tag{5.5}$$

In epochs when the inflow has been approximately radial near the hole during the last several doublings of the hole's mass (e.g., because of viscous or magnetic torquing), the black hole will be rotating slowly and thus will be approximately Schwarzschild. In epochs when the inflow has maintained an accretion torus near the hole during the last several mass doublings, the gas descending from the torus to the hole will have carried so much angular momentum that it will have spun the hole up to nearly extreme Kerr [11]. We shall parameterize the hole's actual spin at any epoch by the specific angular momentum of the gas at the last stable circular orbit $l_{\rm lso}$, in units of that for a Schwarzschild hole; i.e., by the parameter ψ in the following equation:

$$l_{\rm lso} = 2\sqrt{3}\psi\frac{GM}{c}. \tag{5.6}$$

For a Schwarzschild hole, $\psi = 1$; for an extreme Kerr hole, $\psi = 1/3$. In order for a torus to exist at some epoch, the specific angular momentum of the fluid as it nears the hole must then exceed $l_{\rm lso}$. This condition sets the maximum mass

$$M_+ = \frac{1}{12^{3/2}}\left(\frac{c\Omega_0}{G}\right)^3 \frac{1}{\psi^3}\left(\frac{3}{4\pi\rho_0}\right)^2 \simeq 4 \times 10^{-4} M_\odot \frac{1}{\psi^3}, \tag{5.7}$$

above which the rotation of the infalling matter will not be able to supply enough specific angular momentum to stall the accretion at the centrifugal barrier.

From Eq. (5.7) we conclude that for $M > M_+ \approx (0.001 \text{ to } 0.01)M_\odot$ one can neglect the influence of rotation on accretion and assume that the accretion is roughly spherically symmetric. [Actually, as the black hole grows beyond $\sim 0.1M_\odot$ it will accrete the material from radii where specific angular momentum is significantly higher than it would be for a body of unform density. Nevertheless, one can see by looking at the standard solar model tables (e.g., [1]) that this cannot stall the accretion at the Kepler radius except for the last $\sim 10\%$ of the mass of the Sun.]

Various mechanisms of the outward transport of angular momentum within the accreting fluid could, however, remove the centrifugal barrier and preserve essentially spherical accretion at the Bondi rate even for $M < M_+$. Of those mechanisms we first examine braking by molecular viscosity (Sec. 3), then magnetic braking (Sec. 4), and finally braking by convection-induced turbulent viscosity (Sec. 5).

3 Viscous transport of angular momentum

In order to estimate the conditions under which viscosity can keep the accretion practically spherical, we will examine the viscous transport of angular momentum on the background of radial inflow at the Bondi rate $\dot{M} = C_0 M^2$ [where C_0 is defined in Eq. (5.1)]. The radial velocity is then given by

$$v_r = -\frac{C_0 M^2}{4\pi \rho r^2}. \tag{5.8}$$

Since the effects of Sun's rotation should be most pronounced near the equatorial plane, we will consider only the motion in a thin slice $-\alpha/2 < \theta < \alpha/2$ (where θ is the angular latitude with $\theta = 0$ at the equator), and neglect its coupling to the fluid outside the slice.

The total angular momentum enclosed in the ring-shaped part of the slice from r to $r + \Delta r$ is

$$\mathcal{L} = \alpha 2\pi (\Delta r) \rho r^2 l, \tag{5.9}$$

where l is the specific angular momentum. The change in $\mathcal{L}$ is given by the following equation

$$\begin{aligned} \frac{d}{dt}\mathcal{L} &\equiv \left(\frac{\partial}{\partial t} + v_r \frac{\partial}{\partial r}\right) \mathcal{L} = \mathcal{T}(r) - \mathcal{T}(r + \Delta r) \\ &\simeq -\Delta r \frac{\partial}{\partial r} \mathcal{T}(r), \end{aligned} \tag{5.10}$$

where

$$\mathcal{T}(r) = -\alpha 2\pi \rho \nu r^4 \frac{\partial}{\partial r}\Omega \tag{5.11}$$

is the viscous torque exerted on the side of the "ring" at radius r, ν is the kinematic viscosity, $\Omega = l/r^2$ is the angular velocity and $\rho \nu r \partial\Omega/\partial r$ is the viscous stress.

Using Eqs. (5.8)-(5.11), as well as the conservation of mass $d(\rho r^2 \Delta r)/dt = 0$, we arrive at the angular momentum transport equation

$$\frac{\partial}{\partial t} l - \frac{C_0 M^2}{4\pi \rho r^2} \frac{\partial}{\partial r} l = \frac{1}{\rho r^2} \frac{\partial}{\partial r} \left[\rho \nu r^4 \frac{\partial}{\partial r} \left(\frac{1}{r^2} l\right)\right]. \tag{5.12}$$

We now take advantage of the fact that after approaching the black hole to within, say, one half of its original distance r_0, the subsequent flow of a fluid element can be considered stationary since M does not change significantly over the rest of the course of the inflow. Thus, neglecting the time derivative for $r < r_0/2$, we can write the first integral of Eq. (5.12)

$$l + \frac{4\pi\rho\nu}{C_0 M^2} r^4 \frac{\partial}{\partial r}\left(\frac{1}{r^2} l\right) = K, \tag{5.13}$$

where K is a constant of integration.

The kinematic viscosity at the center of the Sun can be estimated as

$$\nu \simeq \lambda_{\rm d} c_{\rm s} \simeq 20 \frac{\rm cm^2}{\rm s} \left(\frac{T}{1.5 \times 10^7 K}\right)^{5/2} \left(\frac{150 {\rm g/cm^3}}{\rho}\right), \tag{5.14}$$

where $\lambda_{\rm d} \simeq 1.2 \times 10^{-18} {\rm cm}\, T^2/\rho \ln \Lambda$ (CGS units) is the mean deflection time of a proton due to Coulomb collisions and $\ln \Lambda \simeq 4$ is the Coulomb logarithm.

We can estimate conditions for effective viscous braking of rotation even without actually solving Eq. (5.13). (However, see Appendix A.) If

$$r > D_{\rm v} = \frac{C_0 M^2}{4\pi\rho\nu} \simeq 1 \times 10^7 {\rm cm} \left(\frac{M}{10^{-10} M_\odot}\right)^2, \tag{5.15}$$

the second term on the left-hand side of Eq. (5.13) will prevent a significant increase in angular velocity. The same condition can be translated into the requirement that the viscous torque per unit area, $\rho\nu\, r^2 \partial\Omega/\partial r$, be greater than the angular momentum current density, $\rho|v_{\rm r}|l$. This can be achieved at $r = r_0$ for $M < 10^{-10} M_\odot$. In this range of masses, the viscous braking is effective for $D_{\rm v} < r < r_0$. Assuming that rotation is roughly rigid ($\Omega \approx \Omega_0$) for $r > D_{\rm v}$, and totally unaffected by viscosity [$\Omega \approx \Omega_0 (D_{\rm v}/r)^2$] for $r < D_{\rm v}$, we estimate the specific angular momentum that the fluid will retain at $r < D_{\rm v}$

$$l = \Omega_o D_{\rm v}^2 = 5 \times 10^8 \frac{\rm cm^2}{\rm s} \left(\frac{M}{10^{-10} M_\odot}\right)^4. \tag{5.16}$$

Equating l with $l_{\rm lso}$ gives, then, the maximum mass $M_{\rm v} \approx 10^{-11} M_\odot$ beyond which an effective removal of angular momentum by conventional viscosity is impossible.

4 The transport of angular momentum by magnetic torques

A potentially more efficient mechanism of braking the accretion-driven differential rotation for black-hole masses above $M_{\rm v}$ can be provided by the well known tendency of magnetic fields, "frozen" in a highly conductive plasma, to resist any flow that would deform the field lines.

The evolution of the magnetic field is governed by the well known equation of magneto-hydrodynamics (MHD) [12]

$$\frac{\partial}{\partial t}\mathbf{B} - \nabla \times (\mathbf{v} \times \mathbf{B}) = \eta \nabla^2 \mathbf{B}, \tag{5.17}$$

where $\eta = c^2/4\pi\sigma$ and σ is the conductivity of the plasma given by

$$\sigma = \frac{1.16}{\pi^{3/2}} \frac{(2kT)^{3/2}}{m_e^{1/2} e^2 \ln \Lambda} \simeq 2.0 \times 10^{18} \mathrm{s}^{-1} \left(\frac{T_0}{1.5 \times 10^7 \mathrm{K}} \right)^{3/2}, \tag{5.18}$$

thus giving $\eta \simeq 36 \mathrm{cm}^2/\mathrm{s}$ for the center of the Sun.

4.1 Ideal magneto-hydrodynamics in the accreting plasma

At first we consider the ideal MHD case ($\eta = 0$) leaving the effects of finite conductivity to the next subsection. Assuming for simplicity axial symmetry, $\partial\omega/\partial\phi = \partial v_r/\partial\phi = 0$, where ϕ is the azimuthal angle, we obtain equations describing the amplification of any preexisting "seed" magnetic field through compression,

$$B_r = \left(\frac{r_0}{r} \right)^2 B_0, \tag{5.19}$$

and winding up,

$$\frac{d}{dt} \left(\frac{B_\phi}{r} \right) = B_0 \left(\frac{r_0}{r} \right)^2 \frac{\partial \Omega}{\partial r} \tag{5.20}$$

of magnetic field lines pinned to a fluid element at the equatorial plane. B_0 is the radial component of the initial field in the fluid element which is at r_0 at the beginning of accretion.

As in the previous section [see comments after Eq. (5.15)], the condition for effective braking of differential rotation is that the magnetic torque per unit area should exceed the angular momentum current density:

$$r \left| \frac{B_r B_\phi}{4\pi} \right| \gtrsim \rho |v_r| l = \frac{C_0 M_c^2}{4\pi r^2} l, \tag{5.21}$$

where $T_{r\phi} = -B_r B_\phi / 4\pi$ is the physical "$r\phi$" component [$\mathbf{e}_\phi \equiv (1/r)\partial/\partial\phi$] of the magnetic stress tensor and M_c is the current mass of the black hole. Using Eq.

(5.19) and defining $x = r/r_0$, $m_c = M_c/M_v = M_c/10^{-11} M_\odot$, we can re-express this condition for effective braking as

$$\left|\frac{B_\phi}{B_r}\right| \gtrsim \left|\frac{B_\phi}{B_r}\right|_{\rm e.b.} = \frac{C_0 M_c^2 l}{B_r^2 r^3} \simeq 6.3 \times 10^{-3} \frac{m_c^{5/3}}{B_0^2} \frac{\Omega}{\Omega_0} x^3. \tag{5.22}$$

Whenever the azimuthal (toroidal) magnetic field of a strength sufficient to satisfy condition (5.22) is generated, the angular velocity will be kept roughly constant, thus preserving an essentially rigid rotation of the accreting fluid.

Similarly to the approximation used in the previous section, we can divide the inflow in two "phases:" in the first (say $1/2 \lesssim x \lesssim 1$), r does not change significantly, while M_c grows, starting from $\sim M_v$, by, possibly, several orders of magnitude

$$\frac{1}{M_v} - \frac{1}{M_c} = C_0 t \tag{5.23}$$

(for $M_c < M_v \simeq 10^{-11} M_\odot$ rotation is rigid due to viscosity – see previous section).

In order to determine whether the winding of the magnetic field lines can lead to the fulfillment of the condition (5.22), we will compute the maximum amplification of the field which is obtained if we neglect the back-reaction on the rotation ($\Omega \approx \Omega_0 (r_0/r)^2 = \Omega_0/x^2$)

$$\frac{\partial \Omega}{\partial r} = \Omega_0 \frac{\partial}{\partial r}\left(\frac{r_0}{r}\right)^2 = -\frac{2\Omega_0}{r_0}\left[\left(\frac{r_0}{r}\right)^3 - 1\right], \tag{5.24}$$

where we have used $dr_0/dr = r^2/r_0^2$. Given Eq. (5.24) and the growth in M_c with decreasing x,

$$x^3 = 1 - \frac{M_c - M_v}{M}, \tag{5.25}$$

where $M = 4\pi\rho r_0^3/3$, the growth of B_ϕ, Eq. (5.20), can be expressed for $M_v \ll M_c < M$ ($1 \ll m_c < m$, where $m = M/M_v = M/10^{-11} M_\odot$) as

$$\begin{aligned} B_\phi &= r r_0^2 B_0 \int_0^t \frac{1}{r^2} \frac{\partial \Omega}{\partial r} dt \\ &\approx -r_0 B_0 \int_{M_v}^{M_c} \frac{dM_c}{C_0 M_c^2} \frac{2\Omega_0}{r_0} \frac{M_c - M_v}{M} \\ &\approx -\frac{2\Omega_0 B_0}{C_0 M} \ln\left(\frac{M_c}{M_v}\right) \\ &\approx -5 \times 10^7 B_0 \frac{\ln m}{m}, \end{aligned} \tag{5.26}$$

where $\ln m_c \approx \ln m$.

The field thus amplified can effectively brake the differential rotation for $1/2 < x < 1$ only if roughly (see Eq. (5.22))

$$m^{8/3}/\ln m < 3 \times 10^9 B_0^2, \tag{5.27}$$

or if

$$M < m_A(B_0)M_v \approx 6 \times 10^{-8} M_\odot B_0^{3/4}, \tag{5.28}$$

assuming $1 < m < M_+/M_v$.

The seed magnetic field B_0 satisfying condition (5.28) will successfully brake differential rotation even for $x < 1/2$, where r (or x) changes by several orders of magnitude while M remains roughly constant ($m_c \approx m$). More specifically, in this region Eq. (5.20) leads to

$$B_\phi \approx -r\frac{4\pi\rho r_0^2}{C_0 M^2} B_0 \int_{r_0/2}^{r} \frac{\partial\Omega}{\partial r} dr \approx -\frac{4\pi\rho r_0^2}{C_0 M^2} B_0 r(\Omega - \Omega_0), \tag{5.29}$$

and thus

$$\frac{B_\phi}{B_r} = -\frac{3}{C_0 M_v}\frac{x^3}{m}(\Omega - \Omega_0). \tag{5.30}$$

The requirement that the magnetic field so amplified keep Ω roughly constant ($\Omega - \Omega_0 = \mathcal{O}(\Omega_0)$) implies, again through Eq. (5.22), relation (5.28) — independently of x.

4.2 Effects of finite resistivity

The winding of the magnetic field lines will inevitably force regions of oppositely directed fields into mutual proximity, and thus, possibly, bring about the onset of fast reconnection and accelerate Ohmic dissipation [effects of the finite conductivity of the plasma, Eq. (5.18)].

From the simple geometry of the frozen magnetic field, we see that the distance Δr between two initially remote points that are brought close to each other by the winding of the field line to which both are pinned is

$$\Delta r \approx \left|\frac{B_r}{B_\phi}\right| \pi r. \tag{5.31}$$

Then, the time scale τ_R at which the field line will reconnect is inversely proportional to the reconnection speed which is a fraction of the Alfvén speed $v_R = \beta v_A$ ($\beta \lesssim 0.1$)

$$\tau_R = \frac{1}{\beta}\frac{\Delta r}{v_A} \simeq \frac{1}{\beta}\Delta r \frac{\sqrt{4\pi\rho}}{|B_\phi|}. \tag{5.32}$$

As a result of the reconnection, the field which was originally ordered on a large scale ($\gtrsim r_0$) is being fragmented into isolated "islands" or "cells," thus reducing its ability to transport angular momentum. However, as long as $\tau_{\rm R}$ is larger than the characteristic time scale of field amplification $\tau_B \equiv B_\phi/(dB_\phi/dt) \simeq (B_\phi/B_r)/|r\partial\Omega/\partial r|$ [see Eq. (5.20)], B_ϕ will continue to grow. In other words if

$$\frac{\tau_R}{\tau_B} \simeq 2\times 10^3 \frac{1}{\beta}\frac{m^{1/3}}{B_0}\left|\frac{B_r}{B_\phi}\right|^3 x^3 \frac{r}{\Omega_o}\left|\frac{\partial\Omega}{\partial r}\right| \gtrsim 1 \tag{5.33}$$

[where we have again used Eq. (5.19) and $r = r_0 x = 3.2\times 10^6 {\rm cm}\ m^{1/3}x$], the magnetic cells will, on average, gain in length along the ϕ direction despite being occasionally broken up by the reconnection.

The reconnection by itself does not cause a significant loss of the magnetic flux. Nevertheless, the reduction of the relevant length scale due to the winding of the field lines will accelerate the familiar Ohmic dissipation which will proceed on the timescale $\tau_{\rm D} = (\Delta r)^2/\eta$. Then, from Eqs. (5.19) and (5.31), we obtain the condition for a continuing amplification of the magnetic field, despite Ohmic dissipation

$$\frac{\tau_{\rm D}}{\tau_B} \simeq 1.4\times 10^7 m^{2/3}\left|\frac{B_r}{B_\phi}\right|^3 x^2 \frac{r}{\Omega_o}\left|\frac{\partial\Omega}{\partial r}\right| \gtrsim 1. \tag{5.34}$$

The effect of reconnection in the early phase of accretion ($1/2 < x < 1$) might be to stop the amplification of the magnetic field before condition (5.22) is satisfied. Otherwise, as shown in the previous subsection, the field will keep the rotation essentially rigid, therefore removing the danger of an all-out reconnection.

The borderline case occurs when $\tau_{\rm R}/\tau_B \approx 1$ at the moment the ratio B_ϕ/B_r reaches the value (5.22). This implies [see Eq. (5.33)] that an effective braking, for $1/2 < x < 1$, can be achieved despite reconnection if

$$\left(\frac{\tau_{\rm R}}{\tau_B}\right)_{\rm e.b} \simeq 3\times 10^{10}\frac{1}{\beta}\frac{B_0^5}{m^{14/3}} > 1, \tag{5.35}$$

where we have used $|\partial\Omega/\partial r| \lesssim 2\Omega_0/r$, $\Omega/\Omega_0 \lesssim 4$. Therefore, if

$$m < m_{\rm R} \simeq 200\frac{1}{\beta^{3/14}}B_0^{15/14}, \tag{5.36}$$

the differential rotation will be braked before the field is fragmented by reconnection. Of course, this assumes that the amplification of the field is efficient enough [condition (5.28)] to give rise to substantial magnetic torques, capable of braking the rotation.

Similarly, at the point of effective braking [Eq. (5.22)], Eq. (5.34) yields

$$\left(\frac{\tau_D}{\tau_B}\right)_{\mathrm{eb}} \simeq 5 \times 10^{14} \frac{B_0^6}{m^{13/3}}, \tag{5.37}$$

leading, therefore, to the upper mass limit for negligible dissipation at effective braking

$$m < m_{\mathrm{D}} = 2 \times 10^3 B_0^{18/13}. \tag{5.38}$$

If condition (5.38) is satisfied, most of the magnetic flux will be preserved despite reconnection. This raises an interesting possibility that the magnetic field fragmented at $x \approx 1$ might still achieve ratio B_ϕ/B_r sufficient for effective braking later in the course of accretion. More specifically, for $x < 1/2$

$$\left(\frac{\tau_{\mathrm{R}}}{\tau_B}\right)_{\mathrm{e.b.}} = 9 \times 10^9 \frac{1}{\beta} \frac{B_0^5}{m^{14/3}} \frac{1}{x^6} \left(\frac{\Omega_0}{\Omega}\right)^3 \frac{r}{\Omega_o} \left|\frac{\partial \Omega}{\partial r}\right|, \tag{5.39}$$

where we have, again, substituted B_ϕ/B_r from the relation (5.22) and assumed a rough conservation of the flux ($B \approx B_0/x^2$) which is necessary for Eqs. (5.22) and (5.33) to be valid. If we also assume that, after the reconnection at $x \approx 1$, the rotation is virtually uninhibited by any angular momentum transport, $\Omega \approx \Omega_0/x^2$ (though the magnetic "cells" produced by reconnection do indeed provide some "friction" [13]), thus minimizing (5.39), we obtain

$$\left(\frac{\tau_{\mathrm{R}}}{\tau_B}\right)_{\mathrm{e.b.}} = 2 \times 10^{10} \frac{1}{\beta} \frac{B_0^5}{m^{14/3}} \frac{1}{x^2}. \tag{5.40}$$

Thus if the accretion is capable of generating strong enough magnetic fields [see Eqs. (5.28) and (5.30)], the reconnection will lose its ability to disrupt the achievement of $|B_\phi/B_r|_{\mathrm{e.b.}}$ at the distance (in units r_0)

$$x_{\mathrm{res}} \approx 1 \times 10^5 \frac{1}{\sqrt{\beta}} \frac{B_0^{5/2}}{m^{7/3}}, \tag{5.41}$$

from the black hole for $m < m_{\mathrm{A}}$, $m < m_{\mathrm{D}}$ but $m > m_{\mathrm{R}}$.

The angular velocity that has increased during the inflow from 1 to x_{res}, $\Omega_{\mathrm{res}} \approx \Omega_0/x_{\mathrm{res}}^2$, will remain roughly constant inward from x_{res} to, say, the accretion radius $x_{\mathrm{a}} \equiv r_{\mathrm{a}}/r_0 \simeq 1 \times 10^{-7} m^{2/3}$, where the effective transport of angular momentum should presumably cease due to the increased radial velocity of the inflow. The requirement that the corresponding specific angular momentum l should be smaller than the last stable orbit angular momentum l_{lso}

$$\frac{l}{l_{\mathrm{lso}}} = \frac{\Omega_{\mathrm{res}} r_{\mathrm{a}}^2}{2\sqrt{3}\psi G M/c} \approx 1 \times 10^{-21} \frac{\beta}{\psi} \frac{m^{17/3}}{B_0^5} < 1, \tag{5.42}$$

translates into a new reconnection limit

$$M < m'_{\mathrm{R}} M_{\mathrm{v}} = 5 \times 10^{-8} M_{\odot} B_0^{15/17} \left(\frac{\psi}{\beta}\right)^{3/17} , \tag{5.43}$$

thus depending only weakly on the details of the mechanism of reconnection (factor β), or the angular momentum of the black hole (factor ψ).

We note in passing that for $x < 1/2$ the danger of Ohmic dissipation is diminished with decreasing x [see Eq. (5.34)]. Indeed, the ratio $(\tau_{\mathrm{D}}/\tau_B)_{\mathrm{e.b.}}$ actually increases inward from $x \approx 1$,

$$\begin{aligned} \left(\frac{\tau_{\mathrm{D}}}{\tau_B}\right)_{\mathrm{e.b.}} &\approx 2 \times 10^7 m^{2/3} \left|\frac{B_r}{B_\phi}\right|^3_{\mathrm{e.b.}} x^2 \frac{r}{\Omega_o} \left|\frac{\partial \Omega}{\partial r}\right| \\ &\sim 10^{14} \frac{B_0^6}{m^{13/3}} \frac{1}{x^3} \end{aligned} \tag{5.44}$$

[compare with Eq. (5.37)]. Therefore, the condition (5.38) which ensures that the flux is not dissipated near $x = 1$ guarantees its approximate conservation during the subsequent inflow.

Finally, we conclude that if all three conditions (5.28), (5.38) and (5.43) are satisfied, the magnetic field will be able to preserve a roughly spherical accretion despite the reconnection and Ohmic dissipation.

For B_0 greater than about 5 Gauss, we see that the only relevant upper mass limit is (5.28), which is imposed only by the limited ability of the flow to amplify the seed magnetic field through an ideal MHD dynamo action. Therefore, if we want the magnetic braking of the differential rotation to be successful throughout the relevant range of mass ($M_{\mathrm{v}} < M < M_+$), we would need to have $B_0 \gtrsim 5 \times 10^5$ Gauss.

5 Convective transport of angular momentum

Since we have shown that viscosity and magnetic braking (for seed fields $B_0 < 5 \times 10^5\,\mathrm{G}$) are not able to ensure an essentially spherical accretion we are faced with a possibility that the rotation of the fluid can radically change the mode of accretion. Following the current understanding of accretion in various astrophysical contexts [6, 14], one might then suspect that the resulting disk or torus-like configuration around the black hole could generate a significantly higher luminosity than the spherical accretion.

Although the details of the accretion at small radii may be very complex and the luminosity emitted by the torus difficult to determine, we will rely on the following simple physical picture to extract enough information for our analysis: The torus, supported in its innermost part by a high specific angular momentum, will push out against the accreting fluid, possibly as far as the accretion radius r_{a} and beyond, and thus reduce the rate of accretion. On the other hand, the increased luminosity produced by the torus cannot be transported by radiation alone. Some, possibly a large part, of the luminosity will have to be transported by convection. However, convection cannot transport the heat efficiently against a supersonic flow since the convective elements would presumably be dissipated by shocks at supersonic convective velocities.

For these reasons, if the luminosity is to be increased above that of Flammang and/or the accretion rate reduced below that of Bondi, the accretion very likely must be subsonic within and everywhere above the torus: Instead of the supersonic transition near r_{a}, which determines the Bondi rate, the fluid will settle subsonically onto the torus.

Besides transferring heat, the convection will also transport angular momentum in the fluid which rotates differentially due to accretion. Since the angular momentum is essential for the maintenance of the altered mode of accretion, we will, in this section, try to estimate the maximum luminosity $\hat{L}(M)$ at which the magnitude of the convective turbulent viscosity would still allow the inflowing fluid to keep a large part of its angular momentum while passing through the convective region surrounding the black hole.

In estimating the effects of convection, we will rely on a mixing-length theory (MLT) of convection in a spherically accreting fluid that we have developed elsewhere [8]. Though the luminosity, as well as the accretion rate, can be affected by the presence of a torus at small radii, we will assume that the accretion at $r > 10r_{\mathrm{a}}$ will deviate very little from spherical symmetry for, say, $M > 10^{-9}M_{\odot}$ [see Eq. (5.4)]. Similarly, while the luminosity may be preferentially emitted along the axis of rotation, we will also assume that the heat flux is roughly isotropic at $r \gg r_{\mathrm{a}} \gg r_{\mathrm{k}}$. [However, see our remarks in the Introduction.] This (almost) spherically symmetric portion above the torus and above r_a is the proper playground for our MLT model of convection in accretion flows.

We will consider only the stage in the evolution of the black hole when its mass is around $M = 10^{-4}M_{\odot}$ since it is at this stage that, due to a high accretion rate, the convection will have the most difficulty reducing the amount of angular momentum in the inflowing fluid — just before the rotation of the Sun looses its relevance at $M = M_+$. Therefore, we can expect the highest $\hat{L}(M)$ right around $M = 10^{-4} M_\odot$ ($m = 10^7$).

As elsewhere in this paper, our estimates will be crude. First of all, we will associate with the convection an effective viscosity $\nu_\mathrm{c} = |v_\mathrm{c} - v| l_\mathrm{m}$, where $v_\mathrm{c} - v$ is the average velocity of the convective elements in the mean rest frame of the fluid and l_m is the mixing length, which is going to be of the order of the distance of the point, at which l_m is estimated, from the black hole [8]. Then, by analogy with the discussion in Sec. 3 in connection with Eqs. (5.12) and (5.13) (see also the Appendix), we can consider the convection capable of holding the angular velocity of the accreting fluid roughly constant at given radius r only if the "braking length"

$$D_\mathrm{c} \equiv \frac{\dot{M}}{4\pi \rho \nu_\mathrm{c}} \tag{5.45}$$

is smaller than r. The length D_c is analogous to the quantity D_v introduced in Eq. (5.15).

Following this basic fact we will simply assume that the angular velocity is constant in the region where $D_\mathrm{c} < r$ and, on the other hand, free to change as $1/r^2$ wherever $D_\mathrm{c} > r$. The region where $D_\mathrm{c} < r$ will be called the "braking zone," and its bottom and top radii will be denoted r_b and r_t.

The discussion so far has not taken into account the overall conservation of angular momentum. Specifically, as a fluid element enters the convection zone from above, the "viscosity" rises abruptly and the element actually gains some angular velocity. Physically, the entering element is at the "receiving" end of the angular momentum "transmission line." Thus we can expect that the (roughly constant) angular velocity within the convection zone should be somewhat higher than the angular velocity of the fluid just above it. This effect is augmented somewhat by the fact that the fluid departing the braking zone leaves behind most of its angular momentum. Because the (molecular or magnetic) viscosity at $r > r_t$ is far smaller than the (turbulent) viscosity at $r < r_t$, the braking zone is isolated in terms of angular momentum transport from the rest of the star, especially during the late phase of accretion that we are particularly interested in. This braking zone actually serves as an angular momentum "depository" throughout the later stages of accretion.

For this reason we will compute the total balance of angular momentum in the braking zone. The contribution that has been brought into the braking zone by the fluid that is currently there is

$$\mathcal{L}_{\rm in} = \int_{r_{\rm b}}^{r_{\rm t}} 2\pi\alpha\rho l_{\rm in}(r) r^2 dr \tag{5.46}$$

where α is the opening angle of the wedge around the equatorial plane (see Sec. 2) and $l_{\rm in} = \Omega_0 r_{\rm in}^2$ is the specific angular momentum brought by the fluid starting from radius $r_{\rm in}$. Bearing in mind that

$$\frac{4\pi}{3}\rho_o r^3 + M = \frac{4\pi}{3}\rho_o r_{\rm in}^3, \tag{5.47}$$

we derive

$$\begin{aligned} \mathcal{L}_{\rm in} &= \frac{\alpha}{2} 4\pi \int_{r_{\rm b}}^{r_{\rm t}} \rho\Omega_0 \left(r^3 + \frac{3}{4\pi\rho} M\right)^{2/3} r^2 dr \\ &= \frac{\alpha}{2} 6.0 \times 10^{29}\,\mathrm{erg\,s}\, m^{5/3} \left[\left((r_{\rm t}/r_{\rm O})^3 + 1\right)^{5/3} - \left((r_{\rm b}/r_{\rm O})^3 + 1\right)^{5/3}\right]. \end{aligned} \tag{5.48}$$

The contribution from the history of departing fluid leaving most of its angular momentum in the braking zone is

$$\begin{aligned} \mathcal{L}_{\rm h} &= \frac{2\pi\alpha}{4\pi} \int_{M_{\rm v}}^{M} (l_{\rm in}(M) - l_{\rm lso}(M)) dM \\ &= \frac{\alpha}{2} 6.0 \times 10^{29}\,\mathrm{erg\,s}\, \left[m^{5/3} - 1 - 0.87 \times 10^{-3}\left(m^2 - 1\right)\right], \end{aligned} \tag{5.49}$$

where we have assumed that the luminosity in the whole previous history since the the end of the "viscous" era at $M_{\rm v}$ was just enough to reduce, via convection, the specific angular momentum from $l_{\rm in}(M) = \Omega_0(3M/4\pi\rho)^{2/3}$ to $l_{\rm lso}$ [Eq. (5.6) with $\psi = 1/3$, see Sec. 2]. In Eq. (5.49) we have integrated from $M_{\rm v}$ because for $M < M_{\rm v}$ the accretion is slow enough for the angular momentum to be distributed throughout a large portion of the star [see Sec. 3].

The sum of the "input" angular momenta $\mathcal{L}_{\rm in}$ and $\mathcal{L}_{\rm h}$ must be equal to the total angular momentum $\mathcal{L}_{\rm st}$ stored in the braking zone. This $\mathcal{L}_{\rm st}$ will depend on the bottom and top radii r_b and r_t of the braking zone, and on the (roughly constant) angular velocity Ω_c in the braking zone:

$$\mathcal{L}_{\rm st} = 2\pi\alpha\Omega_{\rm c} \int_{r_{\rm b}}^{r_{\rm t}} \rho r^4 dr. \tag{5.50}$$

Given a value of the luminosity at the upper boundary of the convective region (which virtually coincides with $r_{\rm t}$), we can integrate the equations of structure of the (convective) spherically symmetric accretion flow [see [8], Eqs. (42) and (44)] and then obtain $\Omega_{\rm c}$ from equation

$$\mathcal{L}_{\rm in} + \mathcal{L}_{\rm h} = \mathcal{L}_{\rm st}. \tag{5.51}$$

The larger is the total luminosity L emerging from the accretion flow, the stronger must be the convection and thus the stronger the turbulent viscosity. The resulting increase in braking efficiency implies that the fluid leaving the braking zone at r_{b}, and proceeding toward the vicinity of the black hole, will have a lower specific angular momentum. There is an upper limit, $\hat{L}(M)$ on the allowed luminosity; above this limit, the inflowing specific angular momentum will be too small to allow an accretion torus to form and thus too small to increase the luminosity above that of Flammang. Thus, this $\hat{L}(M)$ is the accretion flow's luminosity when the specific angular momentum emerging from the braking zone is equal to l_{lso}, which means when $\Omega_{\mathrm{c}} = l_{\mathrm{lso}}/r_{\mathrm{b}}^2$. For this Ω_{c},

$$\begin{aligned} \mathcal{L}_{\mathrm{st}} = \hat{\mathcal{L}}_{\mathrm{st}} &= 2\pi\alpha \frac{l_{\mathrm{lso}}}{r_{\mathrm{b}}^2} \int_{r_{\mathrm{b}}}^{r_{\mathrm{t}}} \rho r^4 \, dr \\ &= \frac{\alpha}{2} 1.9 \times 10^{27} \,\mathrm{erg}\, sm^2 \left((r_{\mathrm{t}}/r_0)^5 - (r_{\mathrm{b}}/r_0)^5 \right) (r_0/r_{\mathrm{b}})^2. \qquad (5.52) \end{aligned}$$

In Fig. 5.1 we plot the luminosity L, the fraction L_{r}/L of the total luminosity transported by radiation, the relative convective velocities and the ratio D_{c}/r, determining the braking of rotation, for $M = 10^{-4} M_{\odot}$ and for three values of the accretion rate: $\dot{M}/\dot{M}_{\mathrm{B}} = 0.1$ (full lines), 0.5 (dotted lines) and 1 (dashed lines). In each of the cases shown, the luminosity as measured at the upper boundary of the convective zone has been fixed as $\hat{L}$, i.e., chosen to yield equality (5.51) for $\Omega_{\mathrm{c}} = l_{\mathrm{lso}}/r_{\mathrm{b}}^2$.

We observe that the luminosity $\hat{L}(M)$, thus obtained, is primarily determined by the need to achieve sufficient braking, i.e., sufficiently small D_{c} at small radii. Especially at higher accretion rates ($\dot{M} \approx \dot{M}_{\mathrm{B}}$), the ratio D_{c}/r can be very small (efficient braking) in the upper portion of the convective region. However, this does not guarantee that the rotation will be braked at small radii, where the increased accretion velocity could make the fluid escape toward the black hole before a significant part of its angular momentum is removed. For this reason, at least at higher accretion rates, we need relatively high luminosities to achieve efficient braking. Naturally, these high luminosities lead to large portions of the total luminosity being transported by convection and to more extended convective regions (see Fig. 5.1) [15].

We notice that at $\dot{M} = \dot{M}_{\mathrm{B}}$ (and for $M = 10^{-4} M_{\odot}$), $\hat{L} \approx 170 L_{\mathrm{Fl}}$. This corresponds to about 10% of the solar luminosity. However, at this accretion rate there remain only $50\mathrm{s} M_{\odot}/M \simeq 6$ days until the mass of the black hole exceeds M_{+} and the rotation ceases to affect the accretion. The amount of heat deposited in the

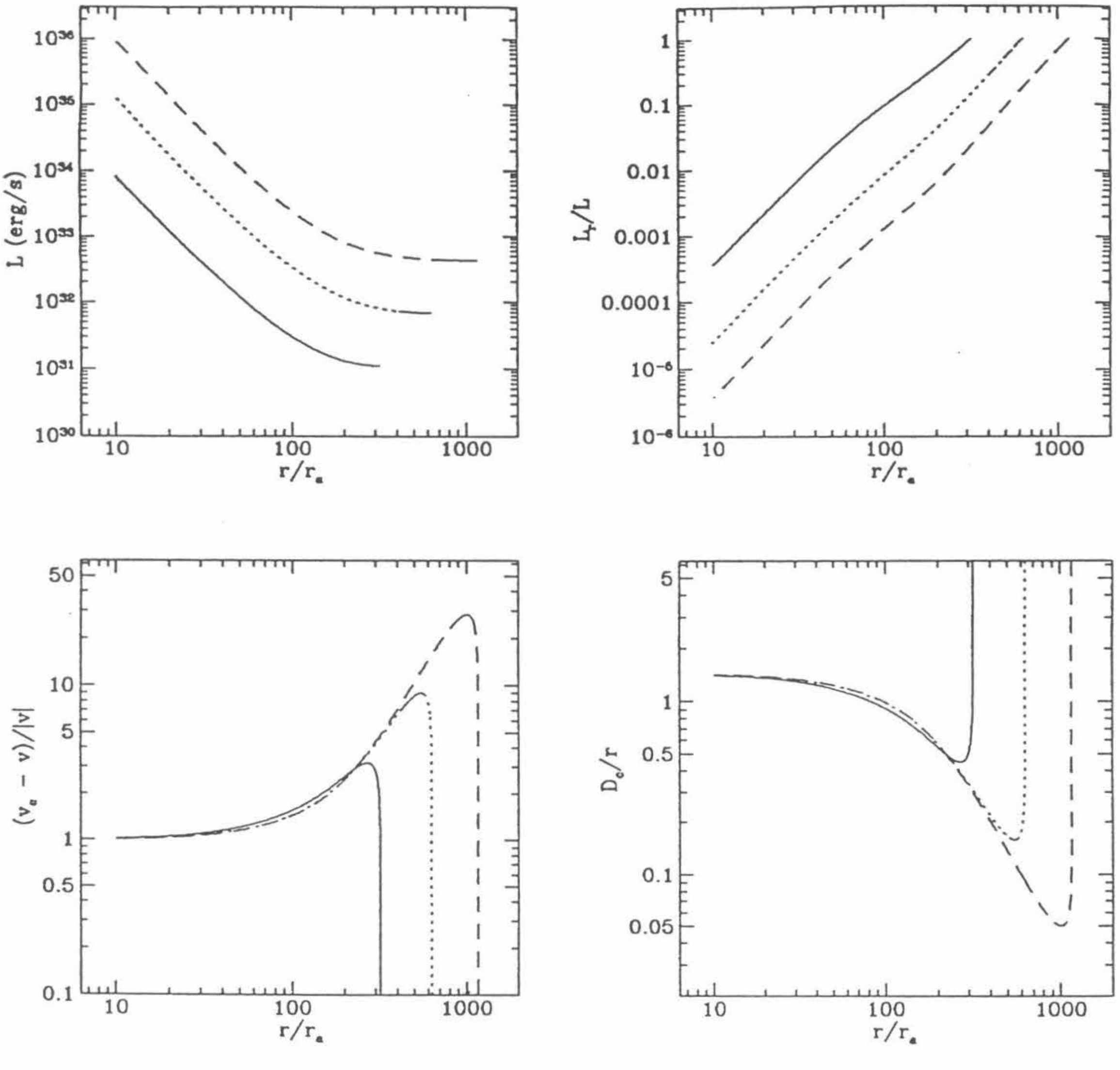

Figure 5.1: Luminosity L, ratio of the radiative and total luminosity L_{r}/L, convective velocity in the mean rest frame of the fluid in units of the accretion velocity and the ratio D_{c}/r for $M = 10^{-4} M_{\odot}$ and three values of the accretion rate as explained in the text.

central region of the Sun by the accreting black hole at this stage ($\sim 10^{38}$erg) will be exceedingly small — certainly too small to have any effect that might be observable from outside our star (e.g., the thermal energy stored in the deepest 1% of the mass of the Sun is $\sim 10^{47}$erg). A similar conclusion holds for smaller accretion rates, at which the time the black hole spends in the vicinity of $M = 10^{-4} M_\odot$ will be longer while the luminosity $\hat{L}$ will be considerably smaller: $\hat{L} \simeq 30 L_{\rm Fl}$ for $\dot{M} = \dot{M}_{\rm B}/2$ and $\hat{L} \simeq 4 L_{\rm Fl}$ for $\dot{M} = \dot{M}_{\rm B}/5$. Since the accretion rate ($\dot{M}_{\rm B} \propto M^2$) will be much smaller in the earlier stages of the evolution of the black hole, the luminosity will never exceed a few Flammang luminosities for $M < 10^{-4} M_\odot$.

As the black hole grows beyond $10^{-4} M_\odot$, the convection will find it more difficult to cope with the higher accretion rate as can be seen from Fig. 5.2. We have followed the growth of $\hat{L}(M)$, as determined by the prescription outlined above, up to the point where $\hat{L}$ roughly equals the solar luminosity $L_\odot$ and the central convective region encompasses about 10% of the mass of the Sun. Clearly, the correct integration of the solar structure, at such relatively large radii, would have to include the energy produced by nuclear burning. However, by not including it, we obtain a reasonable approximation to the requisite $\hat{L}$ [16].

In Fig. 5.2 we express $\hat{L}(M)$ in terms of both the Flammang [$L_{\rm Fl}(M)$] and solar ($L_\odot$) luminosities. We also show the portion $M_{\rm conv}/M_\odot$ of the total mass of the Sun that is included in the central convective region, as well as the time $t_{\rm life}(M)$ that remains until the end of accretion at the given mass of the black hole. Again, the full lines correspond to $\dot{M} = 0.2\dot{M}_{\rm B}$, dotted to $\dot{M} = 0.5\dot{M}_{\rm B}$, and dashed to $\dot{M} = 1\dot{M}_{\rm B}$.

We observe that in all three cases the luminosity $\hat{L}(M)$ will reach $L_\odot$ about three days before the final collapse of the Sun. However, at smaller accretion rates ($\dot{M} = 0.2\dot{M}_{\rm B}$ — see dashed lines) this luminosity is achieved when the mass of the black hole is near M_+. Given the proximity of M_+ and the relatively small total energy released at this stage ($\sim 10^{39}$ergs), it is almost certain that the accretion will sail through this period without producing any change in the appearance of the Sun. Obviously, due to the still lower $\hat{L}(M)$, this conclusion would hold for even smaller accretion rates ($\dot{M} < 0.2\dot{M}_{\rm B}$). Thus, the probable lowering of the accretion rates below the Bondi value, due to to the formation of the torus at small radii, would lead to an accretion invisible for outside observers until the last tens of minutes before the demise of the Sun.

If the accretion could somehow proceed at higher rates ($\dot{M} \sim \dot{M}_{\rm B}$), a much higher energy output would be possible in the last two or three days. The physics

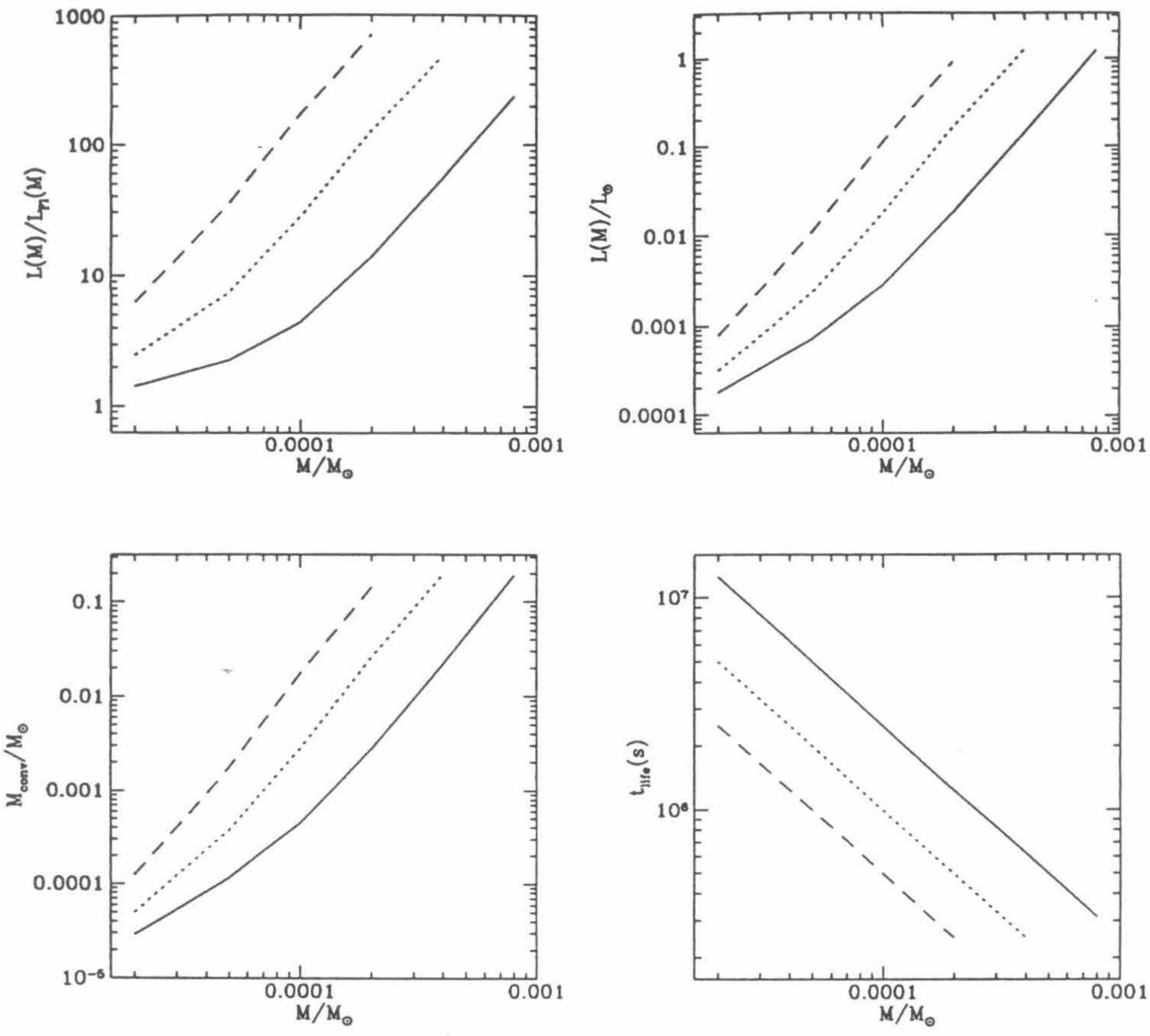

Figure 5.2: Evolution of the luminosity $\hat{L}(M)$ and the mass of the convective region $M_{\rm conv}$ in the short interval before M reaches $M_+ = 10^{-3}M_\odot$ for the same accretion rates as in Fig. 5.1. $t_{\rm life}$ is the time that remains until the end of accretion at the given nass and accretion rate. See text for more detail.

of accretion would become rather more complex, resulting in a possible change in the Sun's appearance. This last stage would then lie outside the scope of this paper. We rest content with the conclusion that for all but (at most) the last two or three days of the accretion, an outside observer would see no reason not to consider the Sun just another, ordinary star.

Acknowledgments

The author wishes to express gratitude to Garrett Biehle, Lars Bildsten, and especially Kip Thorne for enlightening conversations in connection with this research. This paper was supported in part by NSF grant AST-9114925.

Appendix: A stationary solution of the viscous angular momentum transport equation

We rewrite the time independent Eq. (5.13) in a more convenient form

$$\frac{d}{dr}\Omega = -\frac{D}{r^2}\Omega + \frac{KD}{r^4}, \tag{5.53}$$

where $\Omega = l/r^2$ and

$$D \equiv \frac{\dot{M}}{4\pi\rho\nu} = \frac{C_0 M^2}{4\pi\rho\nu}. \tag{5.54}$$

Assuming that D is constant everywhere, we can (substitution $y = 1/r$ is useful) arrive at the solution

$$\Omega = \Omega_0 \left[1 + \frac{D}{r} + \frac{1}{2}\left(\frac{D}{r}\right)^2\right], \tag{5.55}$$

where we have substituted $\Omega_0 \equiv C/D^2$. This solution describes a peculiar stationary vortex in which the angular velocity Ω is constant at $r \gg D$ but increases as $1/r^2$ for $r \ll D$. The "exit" specific angular momentum for the fluid that finally escapes ($r \ll D$) the braking action of the viscosity ν is $l_{\rm ex} = \Omega_0 D^2/2$.

Strictly speaking, this solution is not directly applicable to the problems discussed in this article because it assumes a constant accretion rate and stationarity everywhere — as well as a constant viscosity . However, it strongly indicates that viscosity, or any other angular momentum transport mechanism which can be reasonably quantified by a "diffusivity" ν, can effectively keep the angular velocity constant if $r > D$.

Bibliography

[1] J.N. Bahcall, *Neutrino Astrophysics* (Cambridge University Press, Cambridge, 1990).

[2] T.J. Bowles and V.N. Gavrin, Annu. Rev. Nucl. Part. Sci., **43**, 117 (1993).

[3] S. Hawking, Mon. Not. R. Astron. Soc., **152**, 75 (1971).

[4] Independently of the black hole's ability to produce the required luminosity, there remains the unanswered question of just how a primordial black hole could find itself captured inside the Sun (or any solar-type star). A preliminary study by the author of various mechanisms of capture (e.g., adiabatic evolution of trapped orbits during the condensation of a protostellar cloud, inverse slingshot effect off Jupiter, etc.) suggest that the probability for finding a primordial black hole inside the Sun must be exceedingly low. Due to the extreme crudeness of these estimates, the author will refrain from quoting any numerical values. A more reliable analysis might be undertaken in the future.

[5] D.D. Clayton, M.J.Newman and R.J. Talbot Jr., Ap. J., **201**, 489 (1975).

[6] J. Frank, A. King and D. Raine, *Accretion Power in Astrophysics* (Cambridge University Press, Cambridge, 1992).

[7] R.A. Flammang, MNRAS **199**, 833 (1982), **206**, 589 (1984).

[8] See Chapter 4 of this thesis.

[9] R. Kippenhahn and A. Weigert, *Stellar Structure and Evolution* (Springer-Verlag, Berlin, 1990).

[10] J.-L. Tassoul, *Theory of Rotating Stars* (princeton University Press, Princeton, 1978).

[11] J. Bardeen, Ap. J. **162**, 71 (1970).

[12] E.N. Parker, *Cosmical Magnetic Fields* (Clarendon Press, Oxford, 1979).

[13] F.V. Coroniti, Ap. J., **244**, 587 (1981).

[14] R. Blandford, in *Active Galactic Nuclei* (Springer Verlag, Berlin, 1991).

[15] Strictly speaking, the equations of structure of the accretion flow [8], that we have integrated in Fig. 5.1, are valid only for the region where the flow can be considered stationary. This would be the case for, say, $r \lesssim (3M/4\pi\rho)^{1/3}/2$, since in this region the characteristic time over which the accretion rate changes is longer than the time a given fluid element takes to reach the black hole. At high luminosities the upper boundary of the convective region is certainly outside the stationary domain. At these larger radii, however, the structure of the star is little affected by accretion as can be seen, for instance, from the very slow growth of the luminosity. We can thus consider the structure shown in Fig. 5.1 a reasonable description of the regions at $r \gtrsim 2(3M/4\pi\rho)^{1/3}$ (essentially static configuration), and at $r \lesssim (3M/4\pi\rho)^{1/3}/2$ (stationary flow), as well as the transition between them.

[16] Thus, the standard solar model [1] predicts that the nuclear burning in the innermost 10% of the solar mass generates about one half of the solar luminosity. Furthermore, the contribution of the nuclear burning to the luminosity falls rapidly as we approach the black hole ($dL_{\rm nucl}/dr \propto r^2$). Thus, at small radii, where the need for convective braking of rotation is most critical, the nuclear burning can be safely neglected (see Fig. 5.1).